

**Predicted Safety & Excavation Progress Algorithms for
Autonomous Excavation**

by

Abdullah Rasul

A thesis submitted to the
School of Graduate and Postdoctoral Studies in partial
fulfillment of the requirements for the degree of

Master of Applied Science in Mechanical Engineering

Faculty of Engineering and Applied Sciences

University of Ontario Institute of Technology (Ontario Tech University)

Oshawa, Ontario, Canada

August 2020

© Abdullah Rasul, 2020

THESIS EXAMINATION INFORMATION

Submitted by: **Abdullah Rasul**

Master of Applied Science in Mechanical Engineering

Thesis title: Predicted Safety & Excavation Progress Algorithms for Autonomous Excavation

An oral defense of this thesis took place on August 14 in front of the following examining committee:

Examining Committee:

Chair of Examining Committee	Dr. Sayyed Ali Hosseini
Research Supervisor	Dr. Jaho Seo
Research Co-supervisor	Dr. Amir Khejepour
Examining Committee Member	Dr. Haoxiang Lang
Thesis Examiner	Dr. Xianke Lin

The above committee determined that the thesis is acceptable in form and content and that a satisfactory knowledge of the field covered by the thesis was demonstrated by the candidate during an oral examination. A signed copy of the Certificate of Approval is available from the School of Graduate and Postdoctoral Studies.

ABSTRACT

Excavation is the process of moving earth and is considered to be one of the primary projects in the construction industry. The adoption of various cutting-edge technologies for full automation can be a solution to the various ongoing issues in construction equipment used for excavation such as safety, monitoring, and productivity.

To address this, this project developed advanced safety algorithms and methodologies in ground mapping and estimation of excavation progress, which can accelerate autonomous excavation.

For autonomous excavation, safety is a significant concern to reduce accidents and machinery damage. Considering this point, this thesis deals with tracking, motion prediction, and track management of the detected objects that can improve the safety function of autonomous excavators. The proposed safety algorithms can evaluate the degree of a potential collision risk by using the information of predicted motion of detected objects, working areas of the excavator, and safety indices calculation.

The second component of this project covers the volume estimation for excavation progress estimation, occlusion problem for ground mapping, and 5D mapping. The volume estimation comprises of ground excavation volume and bucket volume estimation. To overcome the problem of an occlusion area that may result in incorrect mapping and estimation of excavation progress, sensing data of proprioceptive and exteroceptive sensors were integrated. Finally, we proposed the idea of 5D mapping to provide a broad spectrum of the excavated ground info that includes the coordinates and material type and properties using a 3D ground map, LiDAR's beam reflectivity, and force index.

Keywords: autonomous excavator; predicted safety algorithm; excavation progress; occlusion area; 5D mapping

AUTHOR'S DECLARATION

I hereby declare that this thesis consists of original work of which I have authored. This is a true copy of the thesis, including any required final revisions, as accepted by my examiners.

I authorize the University of Ontario Institute of Technology (Ontario Tech University) to lend this thesis to other institutions or individuals for the purpose of scholarly research. I further authorize University of Ontario Institute of Technology (Ontario Tech University) to reproduce this thesis by photocopying or by other means, in total or in part, at the request of other institutions or individuals for the purpose of scholarly research. I understand that my thesis will be made electronically available to the public.

Abdullah Rasul

STATEMENT OF CONTRIBUTIONS

Part of the work described in Chapter 4 has been accepted for publication as:

A. Rasul, J. Seo, K. Oh, A. Khajepour, N. Reginald, “Predicted Safety Algorithms for Autonomous Excavators using a 3D LiDAR Sensor”, in 2020 14th Annual IEEE International systems conference.

Part of the work described in Chapter 5 has been accepted for publication as:

N. Reginald, J. Seo, A. Rasul, “Tracking Control of Force/Position and Contour for an Excavator with Co-simulation”, in 2020 IEEE Conference on Electrical and computer engineering (CCECE).

Part of the work described in Chapter 5 has been accepted for publication as:

Reginald, N. and Seo., J., Rasul, A, “Development of an integrated tracking control algorithm for digging operations of an excavator”, 2020 20th International Conference on Control, Automation and Systems (ICCAS 2020), 2020 (Jun), submitted.

ACKNOWLEDGEMENTS

Firstly, I would like to express my sincere gratitude to my supervisor Dr. Jaho Seo, for the continuous support of my study and research, for his motivation, patience, and enormous knowledge. His guidance helped me in all the time of research and thesis writing. It is my honor to be his student and get his guidance during my master study period.

My sincere thanks to my co-supervisor, Professor Amir Khajepour, for giving me all the guidance and knowledge throughout my research period. He shared his knowledge and expertise during every stage, which helped me overcome the obstacles during the research work. Without his supervision and constant help, the dissertation would be challenging to accomplish.

Finally, I would like to thank my family. Words cannot express how grateful I am to my parents and sisters for all the support they have given. Without their continued help and support, I would not be in a position where I am right now.

TABLE OF CONTENTS

Thesis Examination Information	ii
Abstract	iii
Authors Declaration	iv
Acknowledgments.....	v
Table of Contents	vii
List of Tables	xi
List of Figures.....	xvi
List of Abbreviations and Symbols	xxvi
Chapter 1. Introduction.....	1
1.1 Objectives and Scopes	2
1.2 Outlines of Thesis	3
1.3 Working Foundation	5
1.3.1 Veloview	5
1.3.2 Stereo Vision Sensing	6
1.3.3 Point Cloud Registration.....	6
1.3.4 Geometric Transformations of Point Clouds	8
Chapter 2. Literature Review.....	10
2.1 Introduction	10
2.2 Challenges in Sensing for Autonomous Excavation.....	10
2.3 Safety Algorithms for Autonomous Excavators	11
2.3.1 Sensor-Based Safety Management	11
2.3.2 Algorithms-Based Safety Management	12
2.4 Autonomous Excavation Progress	14
2.5 Conclusion	15
Chapter 3. Experimental Test Platform	17
3.1 Introduction	17
3.2 Test Platform	17
3.3 The Excavator.....	17
3.3.1 Mechanical System.....	17
3.3.2 Electronic System	19
3.3.3 Hydraulic System	20

3.3.4	Hardware Controller.....	21
3.4	Sensors.....	23
3.4.1	LiDAR Sensor – Velodyne VLP 16.....	23
3.4.2	Stereo Camera – ZED Camera	25
3.4.3	LVDT Sensor.....	26
3.4.4	Pressure Sensor.....	27
3.4.5	Rotatory Encoder.....	28
3.5	Conclusion.....	29
Chapter 4.	Safety Modules for Autonomous Excavators	30
4.1	Introduction	30
4.2	Object Detection.....	31
4.2.1	Plane Fitting and Ground Points.....	31
4.2.2	Neighboring and Clustering.....	32
4.2.3	Bounding Box	33
4.3	Object Tracking and Track Management	34
4.3.1	Extended Kalman Filter	34
4.3.2	Joint Probabilistic Data Association	36
4.4	Safety Indices	38
4.4.1	Kinematic Analysis and Working Area of Excavator.....	39
4.4.2	Time to Collision (<i>TTC</i>).....	41
4.4.3	Warning Index (<i>x</i>).....	42
4.5	Safety Level Decision.....	43
4.6	Conclusion.....	43
Chapter 5.	Autonomous Excavation Progress	45
5.1	Volume Estimation Algorithm	45
5.1.1	Point Cloud registration using NDT.....	45
5.1.2	Ground excavation volume estimation.....	47
5.1.3	Bucket CAD Model.....	48
5.1.4	Bucket Volume Estimation.....	49
5.1.5	Volume Estimation Algorithm Summary	51
5.2	Occlusion Detection.....	51
5.2.1	Sensor Vision occlusion.....	52

5.2.2	Initial Exteroceptive Map.....	52
5.2.2	Identification of Bucket Trajectory using Kinematic Analysis	53
5.2.2.1	Conversion of Stroke to Bucket Position	54
5.2.2.2	Conversion of 2D Bucket Trajectory to 3D	56
5.2.2.3	Meshing and Triangulation of Bucket Trajectory.....	57
5.2.3	Reconstruction of a Map for Occlusion Areas	58
5.3	5D mapping	59
5.3.1	Building 3D Geometrical Map	60
5.3.2	Materials Classification using LiDAR's Intensity	61
5.3.3	Soil Type Classification Using Neural Network	62
5.3.4	Construction of 5D Map	64
Chapter 6.	Results and Analysis.....	65
6.1	Introduction	65
6.2	Sensors Selection	65
6.3	Predicted Safety Algorithm Results.....	66
6.3.1	Sensor Location	66
6.3.2	Experimental Test Scenario	67
6.3.3	Obstacle Detection and Tracking	67
6.3.4	Safety Evaluation Results	69
6.4	Volume Estimation Results and Analysis	73
6.4.1	Bucket Contained Volume Estimation.....	73
6.4.2	Ground Excavation Volume estimation	76
6.4.3	Relationship between ground and bucket volume.....	78
6.5	Occlusion Area Problem Results and Analysis.....	82
6.5.1	Bucket Trajectory formation.....	82
6.5.2	Reconstructed map for occluded area	84
6.5.3	Verification of reconstructed map for Occluded Area.....	85
6.6	Material Properties – 5D Map.....	87
6.6.1	3D ground map and LiDAR's intensity	87
6.6.2	Force Index	89
6.6.3	Relationship between Intensities and Forces	93
6.6.4	Soil type image classification results	95

6.6.5	5D map Construction	96
Chapter 7.	Conclusion and Future Work.....	98
7.1	Conclusion	98
7.2	Future Improvements	100
REFERENCES	101
APPENDICES	109
	Appendix A. Point cloud Transformation.....	109

LIST OF TABLES

CHAPTER 1

Table 1.1: Transformation Methods Comparison	8
Table 1.2: Registration Methods Comparison	8

CHAPTER 3

Table 3.1: Platform Specifications	18
Table 3.2: VLP-16 Specifications	23
Table 3.3: ZED Camera Specifications.....	25
Table 3.4: LVDT Specifications.....	27
Table 3.5: Pressure Sensor Specifications	28

CHAPTER 5

Table 5.1: Physical Measurements of Excavator	54
---	----

CHAPTER 6

Table 6.1: Estimated Volume Comparison.....	81
Table 6.2: Excavation Progress Rate	81
Table 6.3: Intensity and Forces Relationship	93
Table 6.4: Natural Ground Classification Relationship	94

Appendix A

Appendix A.1: 3D Geometric Transformation Matrices	109
--	-----

LIST OF FIGURES

CHAPTER 1

Figure 1.1: Veloview.....	5
Figure 1.2: Stereo Vision Process [52]	6
Figure 1.3: Point Cloud Registration Workflow	7
Figure 1.4: Point Cloud Registration	7

CHAPTER 3

Figure 3.1: Test Platform [1]	18
Figure 3.2: Electronics System of Test Platform [1].....	19
Figure 3.3: Relay Box	20
Figure 3.4: Links and Actuators of Excavator	21
Figure 3.5: dSPACE MicroAutoBox II [28].....	22
Figure 3.6: dSPACE Simulink Interface Blockset	23
Figure 3.7: VLP-16 LiDAR	24
Figure 3. 8: ZED Stereo Camera	25
Figure 3.9: LVDT Sensor on Excavator [1]	27
Figure 3.10: Pressure Sensor on Excavator [1]	28
Figure 3.11: Rotatory Encoder [1]	29

CHAPTER 4

Figure 4.1: Safety Module Process Overview	30
Figure 4.2: Object Detection and Tracking Workflow	31
Figure 4.3: Raw Point Cloud (a), and Clustered Point Cloud (b)	33
Figure 4.4: Detected Objects with Bounding Boxes	34
Figure 4.5: EKF Procedure	36
Figure 4.6: JPDA Events.....	38
Figure 4.7: LVDT - Stroke Data.....	39
Figure 4.8: Working Area of the Excavator [19]	40
Figure 4.9: Variables Illustration for TTC (left), Variables Illustration for Warning Index [19]	42
Figure 4.10: Safety Level Indices.....	43

CHAPTER 5

Figure 5.1: Pre-Excavation Ground Image and Point Cloud	47
Figure 5.2: Ground Image and Point Cloud After Digging	48
Figure 5.3: Bucket CAD model (a), and Bucket CAD Model Point Cloud (b)	49

Figure 5.4: Stereo Camera Position.....	50
Figure 5.5: Bucket Containing Soil Point Cloud (left) and Actual Image (right)	50
Figure 5.6: Bucket CAD Model and Registered Point Cloud	51
Figure 5.7: Initial Occluded Area Ground Map	53
Figure 5.8: Occlusion Area in Front of Excavator	53
Figure 5.9: Boom, Arm, and Bucket Links and Their Corresponding Angles.....	54
Figure 5.10: Bucket Actuator and Corresponding Four-Bar Mechanism.....	55
Figure 5.11: 2D Bucket Trajectory	56
Figure 5.12: Conversion of The Bucket Trajectory in 3D Space	57
Figure 5.13: Conversion of Bucket Trajectory to Mesh	58
Figure 5.14: Map Update After Proprioceptive Merging	59
Figure 5.15: Reconstructed Map: Occlusion Area Problem	59
Figure 5.16: Excavation Ground Image.....	60
Figure 5.17: Excavation Ground Point Cloud	61
Figure 5.18: Intensity Index for Soil	62
Figure 5.19: Network Architecture and Network Layers Information	63
Figure 5.20: Image Classification Using CNN.....	64

CHAPTER 6

Figure 6.1: LiDAR Position.....	66
Figure 6.2: Multiple Object Detection	67
Figure 6.3: Operator's View.....	68
Figure 6.4: Tracking Details for Multiple Objects	69
Figure 6.5: Excavator Working Area - Multiple Objects	70
Figure 6.6: Safety Evaluation for Multiple Objects	71
Figure 6.7: Working Area- Single Object.....	72
Figure 6.8: Safety Evaluation - Single Object.....	72
Figure 6.9: Filled Bucket Image.....	73
Figure 6.10: Filled Bucket Point Cloud	74
Figure 6.11: Filled Bucket Point Cloud and Bucket CAD Model Merged	74
Figure 6.12: Scenario 1 - Accumulated Bucket Volume	75
Figure 6.13: Scenario 2 - Accumulated Bucket Volume	75
Figure 6.14: Ground Surface Point Cloud Before Excavation	76
Figure 6.15: Ground Surface Point Cloud After Digging.....	76
Figure 6.16: Scenario 1 - Ground Volume	77
Figure 6.17: Scenario 2 - Ground Volume	77
Figure 6.18: Scenario 1 - Bucket and Ground Volume Comparison	78
Figure 6.19: Scenario 2 - Bucket and Ground Volume Comparison	78
Figure 6.20: Scenario 1, and 2 Merged - Bucket and Ground Volume Comparison	79
Figure 6.21: Scenario 1,2, and 3 Merged - Volume Estimation Comparison	79
Figure 6.22: Ground and Bucket Volume Relationship.....	80
Figure 6.23: Occlusion Area Problem.....	82

Figure 6.24: Occluded Area Point Cloud.....	83
Figure 6.25: Bucket Trajectory.....	83
Figure 6.26: Bucket Trajectory Meshing.....	84
Figure 6.27: Merging of Occluded Area Point Cloud and Bucket Trajectory	84
Figure 6.28: Reconstructed Map for Occluded Area	85
Figure 6.29: Occluded Area - Front Side.....	85
Figure 6.30: Occluded Area - Opposite Side.....	86
Figure 6.31: Occlusion Area Verification (Left: Front and Right: Opposite)	86
Figure 6.32: 3D Geometrical Info for Soil	87
Figure 6.33: Soil Intensity Value for 5D Map.....	88
Figure 6.34: Position and Intensity Values for Sand and Soil.....	88
Figure 6.35: Sand Bucket Trajectory w.r.t to Time	89
Figure 6.36: Soil Bucket Trajectory w.r.t to Time	90
Figure 6.37: Head Force - Sand.....	90
Figure 6.38: Rod Force - Sand.....	91
Figure 6.39: Net Force - Sand	91
Figure 6.40: Head Force - Soil	92
Figure 6.41: Rod Force - Soil	92
Figure 6.42: Net Force - Soil	93
Figure 6.43: Image Classification – Segment 1.....	95
Figure 6.44: Image Classification - Segment 2	95
Figure 6.45: Image Classification - Segment 3	96
Figure 6.46: 5D Map Construction	97

LIST OF ABBREVIATIONS AND SYMBOLS

3D	Three Dimensional
5D	five Dimensional
BIM	Building Information Modelling
CAD	Computer-Aided Design
CAN	Controller Area Network
CNN	Convolutional Neural Network
CPD	Coherent Point Drift
CSV	Comma-Separated Values
ECU	Electronic Control Unit
EHD	Electro-Hydraulic Driver
EHPV	Electro-Hydraulic Proportional Valve
EKF	Extended Kalman Filter
I/O	Input/Output
ICP	Iterative Closest Point
JPDA	Joint Probabilistic Data Association
LiDAR	Light Detection and Ranging
LVDT	Linear Variable Differential Transformer
NDT	Normal Distribution Transformation
RANSAC	Random Sample Consensus
RMS	Root Mean Square
RFID	Radio-Frequency Identification

RTLS	Real-Time Location System
TTC	Time to Collision
UAV	Unmanned Aerial Vehicle
UWB	Ultra-Wideband
WLAN	Wireless Local Area Network

Chapter 1. Introduction

Excavation is the process of moving earth and is considered to be one of the primary projects in the construction industry. However, construction sites for excavation are always under harsh ground and hazardous environmental conditions that can be a critical obstacle to maximize productivity and enhance safety. The adoption of various cutting-edge technologies for full automation (i.e., autonomous operation) can be a solution to this ongoing issue in construction equipment used for excavation such as safety, monitoring, and productivity.

With the increasing number of accidents on the excavation sites, involving the workers, and the excavators, the advanced safety control algorithms become the crucial aspect of the autonomous excavators. The poor visibility due to the blind spots and operator's carelessness can increase the chances of potential risks. So, our first focus is to develop an advanced safety algorithm for autonomous excavators that can predict the motion of the objects on the site, predict the working area of the excavator, and generate safety indices to avoid a collision.

Automating the excavation process also involves monitoring its progress. The estimation of the excavation progress is an essential step because it keeps track of the whole process, and it helps to complete each task. This project focuses on developing the algorithm that can provide 3D ground mapping to identify the changes in the ground during the excavation, the ground, and bucket volume estimation.

It is also imperative to identify the properties of the material to be excavated as it has a direct effect on excavation planning. Types of materials significantly determine the forces required for the excavation task. Keeping this point in mind for autonomous excavation, we proposed a methodology of material classification, such as soil and sand.

The introduction of automation in the excavation has also raised safety concerns, environmental monitoring, and excavation progress. The advanced safety algorithms, 3D ground mapping, and estimation of work progress can accelerate autonomous excavation, and therefore the following points are of great importance.

- The nature of the construction sites includes dynamic objects, such as workers and other machines whose presence increases the chances of collision and other potential hazards, thereby requiring the improvement of safety management systems used in autonomous excavation [4].
- For each excavation task, a progress estimation is required to increase efficiency. Also, the excavation progress is significant as it describes the completion of each task [5], which requires the introduction of the sensing algorithm for generating the digging profile and checking the excavation progress.
- The material properties have a direct effect on the excavation, so an algorithm is required to identify the type and properties of the material.

By considering the above reasons, the automation of excavation becomes a broad research topic as it has to deal with the safety concerns, the progress of work done, materials to be excavated, etc. The mobile robotics concepts help in locomotion and navigation of the mobile excavators. Many applications from the robotics help in understanding the kinematics and dynamics of the excavators. The computer vision techniques help in processing the sensor's data.

Sensing the excavation is a challenging task; especially under the urban scenarios, because of compact space, narrow areas, buried gas pipes, cables, etc. Therefore, safety becomes a significant component, and more sophisticated ground mapping is also crucial to achieving safe, efficient, and productive excavation. The advanced safety algorithm avoids potential collision risk among the objects on the site, and ground mapping determines the changes in the ground, along with the objects present underground, such as pipes. The focus of this research is to develop an advanced safety algorithm for urban scenarios, along with efficient ground mapping. The main idea, scope, and objectives of this thesis are described in this chapter.

1.1 Objectives and Scopes

The primary scope of this thesis is to develop the safety and the environmental monitoring algorithms for autonomous excavators. To support the original work, the processing of sensors, instrumentation of excavator, and implementation of software have been applied. The goal is to develop the predictive safety algorithms and to provide methodologies of environmental monitoring for excavation progress.

Detailed objectives are as follows:

Safety Algorithm:

- Development of object tracking algorithm in the cluttered environment for tracking the objects and machines around the excavator on the construction site.
- Development of safety strategies for autonomous excavators to avoid the collision between the excavator and other objects present on the site.
- Development of an algorithm to predict the working area of the excavator based on the kinematic analysis and sensors attached to the excavator.
- Combining object tracking, safety strategies, and working areas of the excavator to achieve the predicted safety algorithm that can evaluate a safety risk in terms of the safe, warning, and emergency braking.

Environmental Monitoring Algorithm:

- Development of ground mapping of an excavated area to construct a map of the ground after each digging.
- Development of volume estimation algorithms using the ground profile and bucket CAD model.
- Reconstruction of a ground map for an occlusion area for excavation where the sensor vision is blocked due to the pile on the ground or the excavator's arm.
- Identification of a soil type using point clouds, an intensity value of a laser beam from a LiDAR, and a force index.
- Classification of soil images using the convolutional neural network to strengthen the soil type classification algorithm.

1.2 Outlines of Thesis

Chapter 1 introduces the main scope, detailed objectives, and expected outcomes of this work by explaining the research area and motivation for this project. The section also covers the tools and software used to support the research work, along with the working foundations.

Chapter 2 provides a literature review of the sensing algorithms for the autonomous excavators. Current research, methodologies, and challenges in the safety and excavation progress algorithms have also been elaborated upon.

Chapter 3 discusses the developed experimental test platform. The section includes the type and working of the sensors selected for this project. Also, the working of the LVDT, pressure sensors, and rotational encoder attached to the arm of the excavator has been addressed. Lastly, the specific excavator and the hardware controller for this thesis have been explained.

Chapter 4 explains the predicted safety algorithm in detail. The section starts with the pre-processing of sensory data that includes the object detection and tracking. Then, it explains the kinematic analysis to calculate the working area of the excavator. Lastly, the safety indices, Warning Index (x), and Time to collision (TTC) have been discussed to predict potential collision risks.

Chapter 5 describes the developed environmental sensing algorithm that includes three different aspects of excavation progress, volume estimation, occlusion area problem, and 5D mapping. Volume estimation deals with the estimation of the ground volume, and the bucket volume after each dig. The occlusion area problem reconstructs the ground map using the bucket trajectory. 5D mapping helps in identifying the type and properties of the material on the digging area.

Chapter 6 presents the experimental results obtained from each theme- safety, volume estimation, occlusion area, and the 5D mapping. The results have been explained by providing different scenarios for each topic. A comparative study between the scenarios has been carried out.

Chapter 7 provides the closing remarks by concluding the thesis, along with the limitations and future work recommendations.

1.3 Working Foundation

This section provides the tools and software used for the project foundation. The framework of the software platform used for this project has been addressed. The structure describes the summary of the tools and their applied libraries.

1.3.1 Veloview

Veloview is a software that performs real-time visualization and processing of LiDAR data [6]. The data can be captured from any Velodyne HDL sensors. It helps in displaying the point cloud that contains the info of distance, intensity of return-of-beam, time, azimuth, and laser identity. The data can be exported in various forms, such as CSV, PCAP, etc. The software has been used to capture the point cloud from LiDAR for offline data processing and preliminary work.

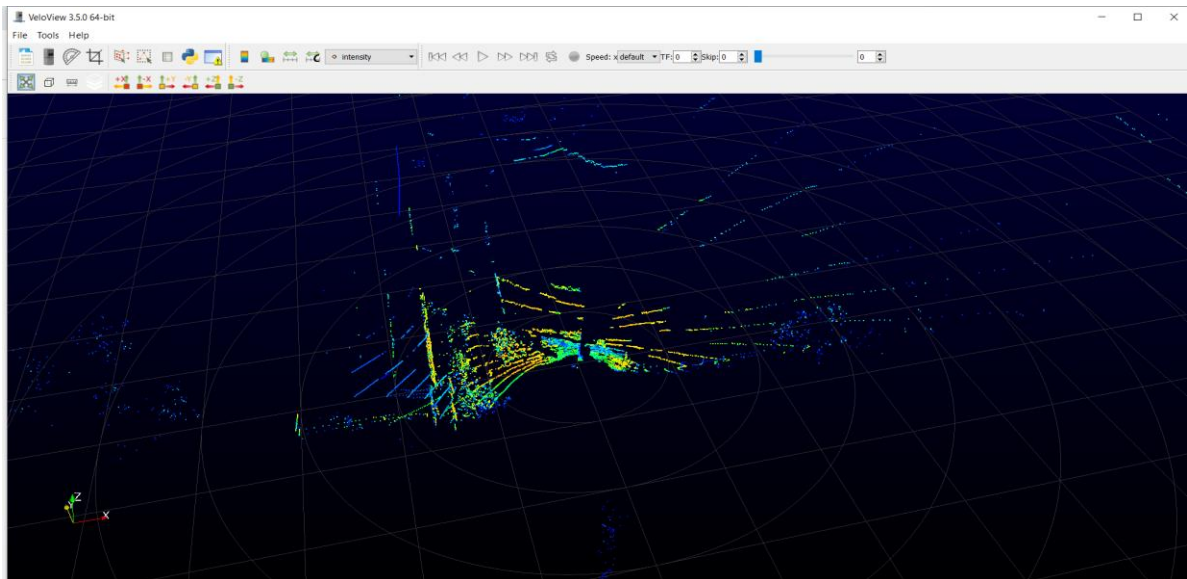


Figure 1.1: Veloview

1.3.2 Stereo Vision Sensing

Stereo cameras are a type of camera with two or more lenses projecting a separate image from each lens. This allows cameras to simulate human binocular vision, therefore provides the ability to capture three-dimensional images. The stereo vision technique uses two cameras to see the same object. A baseline separates the two cameras, the distance for which is accurately known, as shown in Fig. 1.2 [53]. The two images from both cameras are analyzed to note the differences between images. Features like edges can be found easily in one image, and the same feature can be searched in the second image. The disparity between the images helps to get the depth of the point, which enables projecting it in a 3D world [52].

Every point in a point cloud corresponds to a solid angle of operation, and the distance from the point in that direction. In this way, the sensor can scan all the possible solid angles. The distance and angles can be projected into a 3D world for mapping purposes.

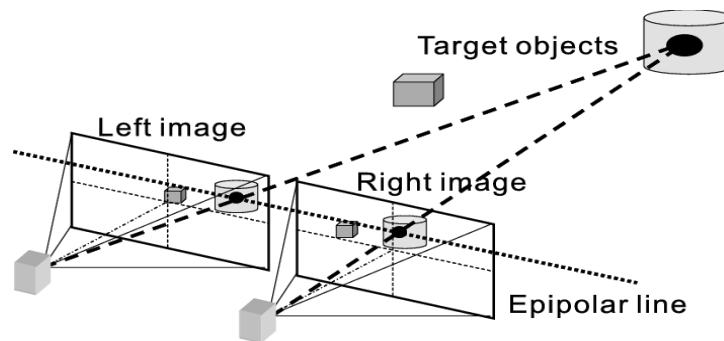


Figure 1.2: Stereo Vision Process [52]

1.3.3 Point Cloud Registration.

Registration is the process of aligning two or more point clouds of the same scene [40]. It helped in reconstructing the same scenes from different sources or locations. The point cloud registration workflow is demonstrated in Fig. 1.3.

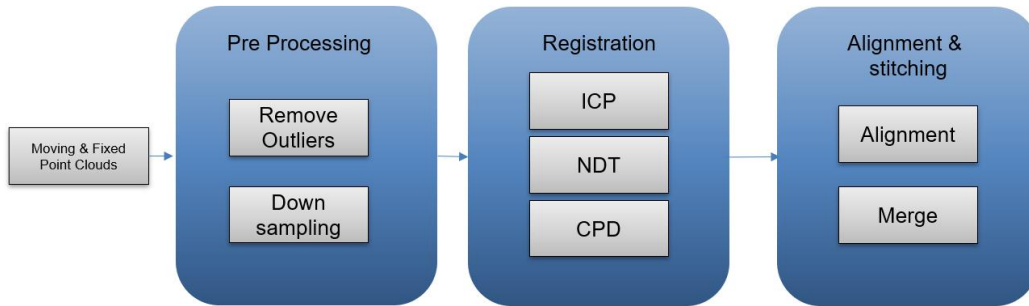


Figure 1.3: Point Cloud Registration Workflow

The point cloud registration is divided into three steps, as shown in Fig. 1.3. Two point-clouds have been chosen. The first point cloud is fixed, and the second is moving. Before applying the registration algorithm, preprocessing should be done on the raw point cloud. The first step in the preprocessing is to remove the outliers, noise, and unwanted objects. The second step of preprocessing is to downsample the data into a smaller number of points that helped in reducing the computational complexity. After the preprocessing, the registration method has been implemented on the preprocessed data. The point cloud registration has been illustrated in Fig. 1.4.

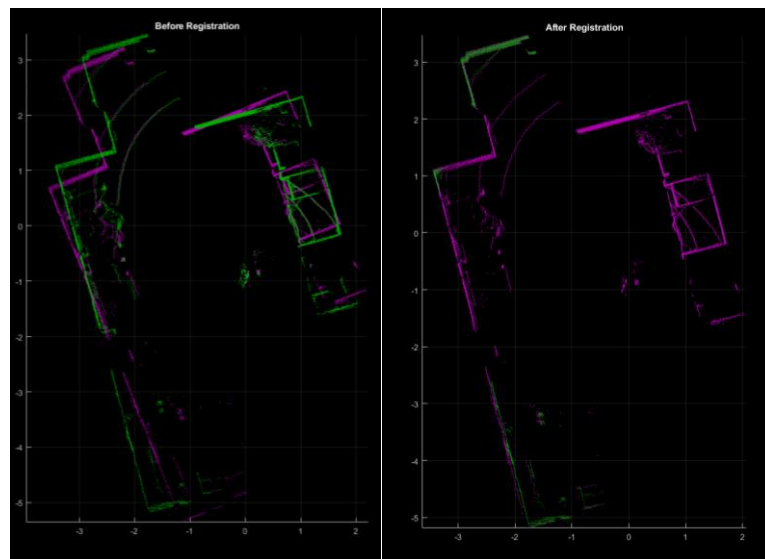


Figure 1.4: Point Cloud Registration

A comparison between different transformation and registration techniques is mentioned in Table 1.1, and 1.2

Table 1.1: Transformation Methods Comparison

Transformation	Description
Rigid	Preserves shape, undergo translation, rotation
Affine	Allows the objects to shear and change scale in addition to translations and rotations.
Non-Rigid	the shape of objects in the scene to change.

Table 1.2: Registration Methods Comparison

Registration Method (function)	Transformation Type	Description	Performance Characteristics
NDT	Rigid	Relies on an initial transform estimate, Better with point clouds of differing resolutions and densities	Fast registration method, but generally slower than ICP
ICP	Rigid	initial transform estimate	Fastest registration method
CPD	Rigid, affine, and non-rigid	does not rely on an initial transformation estimate	Slowest registration method

1.3.4 Geometric Transformations of Point Clouds

Geometric transformation is referred to as the transformation of perceived data from vision sensors. This transformation could be translational, rotational, shearing the point cloud, and scaling. The geometric transformation matrix has been used to perform a

global transformation of the point cloud. Often during the excavation tasks, we use multiple sensors. Since each sensor has its frame of reference, we need to transform each frame of reference to a single global reference. Such transformations can be done using the transformation matrices.

For this project, we are using a stereo vision camera and a LiDAR. Both sensors provide the 3D point cloud. The transformation matrices for 3D point clouds are given in appendix A.

Chapter 2. Literature Review

2.1 Introduction

This chapter covers the literature review of relevant topics in the sensing field of the excavation. State of the art methodologies for sensing construction environment are addressed. In addition to the challenges faced in this field, this chapter also introduces the current research in the areas of safety and excavation progress. The existent studies on safety are reviewed in terms of the type of used sensors, feature, function, and algorithm. Excavation progress research is addressed in various contexts such as volume estimation, occlusion area problem, image-based progress, point clouds, and UAVs.

Finally, the chapter summarizes the currently applied algorithms and technologies in safety management and excavation progress for construction equipment. It also describes the intrinsic limitations of each approach that motivates this study.

2.2 Challenges in Sensing for Autonomous Excavation

Constructions sites are complicated, because of the presence of workers, goods, and machines [12]. The interaction among these objects can create difficulty in perception due to occlusion. A fusion of proprioceptive and exteroceptive sensors can be a solution to this problem [24]. The proprioceptive sensors can be used to identify the dynamics of an excavator such as motor speed, wheel load, robot arm joint angles while the exteroceptive sensors like Lidar can acquire the information of change in the environment by measuring the distance between the excavator and objects.

The machine's external environment sensing is a prerequisite to: planning the tasks and controlling the motion, monitoring the objects around the excavator, autonomous digging operation, and monitoring the progress towards task completion.

Existing researches focus on 3D mapping of the changes in the external environment. This change could be the workspace, terrains, objects around the machine, or

their historical variation due to excavation [11]. The commonly used sensors are stereo vision cameras, or 2D or 3D laser scanners. A stereo vision camera can acquire data rapidly. However, the accuracy is lower than laser scanners. In contrast, laser scanners are expensive and susceptible to vibration that is a significant factor to significantly degrade the sensing performance in excavation machines.

Parameter estimation is an essential factor in autonomous operations. Although some states such as pressure, strokes, rotation, and changes in the ground surface can be directly measured by sensors, estimation of some key states such as position of moving objects around an excavator and interaction force between the bucket and ground is still challenging [20].

2.3 Safety Algorithms for Autonomous Excavators

2.3.1 Sensor-Based Safety Management

This section covers the safety management for construction using different sensor-based technologies, such as vision-based sensing, wireless sensor networks, and the combination of multiple sensors.

Between 2005 to 2019, the distribution of different sensor-based technologies shows that the most widely used technology is RFID, followed by wireless sensor networks, camera-based, and UWB (ultra-wideband) [12]. WLAN (wireless local area network) and ultrasound are the least used technologies. The study of [13] proposed a real-time locating system (RTLS) using the RFID that can achieve safe operations for construction machines. The proposed system includes three key components that are the localization, wireless networking, and an assistant tag to provide robust localization performance in the construction sites. The localization function retains high accuracy in localization, even in the presence of obstacles. The wireless network can transfer real-time data and minimizes information loss. To implement RFID, tags must be linked to target objects, and RFID readers are required to detect the corresponding tags. The necessary preparation work and additional devices have significant disadvantages. RFID requires a

direct line of sight for optimal accuracy, which is a difficult condition to perform in construction. In addition, it requires the installation of multiple labels and receivers which limit their practicality.

[14] provided the idea of material tagging using RFID tags that can be automatically identified and tracked on construction sites. This approach permits the automatic reading of tagged materials by the supervisor. Placing labels on resources involves numerous problems that a vision-based approach does not have. Namely, staff can intentionally remove labels due to privacy issues, reading labels on ferrous materials remains a challenge, and the size and geometry of the label make it difficult to apply. GPS works well for monitoring heavy construction equipment (e.g., earthmoving) but it may not provide accurate positioning data in places where GPS signals cannot reach such as very dense urban environments or indoors.

The vision-based safety management has also gained some attention in recent years. [15] developed a motion capture and recognition framework for safety management that could achieve behavior-based monitoring for unsafe action detection. This framework can be characterized by the main functions of unsafe behavior identification, collection of site videos and motion templates, extraction of a 3D skeleton from the videos, and unsafe action detection using skeleton and motion templates. Unsafe behavior is the data from accident statistics, and historical safety documents, while unsafe action is based on the posture of the worker. Three-dimensional (3D) sensing devices, e.g., stereo-vision camera and depth sensors have been used to determine the distance from given 3D spatial information. However, such sensing devices are limited in their range and are sensitive to lighting, and therefore, they are not feasible for construction safety management.

2.3.2 Algorithms-Based Safety Management

The accident forewarning system (AFS) safety management for construction sites usually adopts “accident prevention” or “accident forewarning system.” It emphasizes upon generating an early warning index that is capable of detecting and identifying unsafe

behavior of persons or machinery around construction sites. The accident forewarning system provides support for prevention and sending alerts to construction workers and managers. [16] proposed the function of accident prevention by implementing internet-of-things in a safety management system for tower crane groups. In their system, an anti-collision algorithm can be generated to check the state of each tower crane using horizontal and vertical position sensors, angle sensors, tilt, and wind speed sensors.

Another approach for construction site safety management is the “safety route prediction and planning (SRPP).” This method can predict trajectories of a worker or a machine and be extended to prevent a collision. [17] proposed the idea of tracking and predicting the states of on-site workers and mobile machines by applying the Kalman filter.

The algorithm takes the input data in the form of video frames from multiple sources and outputs the corresponding predicted states. The limitation of this idea is that the proposed tracking filter works with linear states only. However, the movement of the machines and workers on the construction sites are non-linear. Another demerit of this approach is that the idea shows the state of workers or machines only; and does not provide the interaction between these two.

The next approach is the “integrated safety management.” [18] built an “integrated safety management system” by considering the hot and humid environment on construction sites that enable real-time environmental monitoring, visualization, and notification with the aid of wireless sensors network. Another outcome of this system is to provide reliable data for time-sensitive emergencies of health and safety management. This idea deals with the quality inspection of construction material and the health management of workers.

LiDARs (light detection and ranging) as a remote sensing method have become very popular in the autonomous vehicles research field. There has not been much research work in the field of safety management for autonomous excavators using LiDARs. [19] developed detailed safety algorithms for autonomous excavators using a 2D laser scanner and kinematics analysis.

However, most previous studies have focused on proximity-based safety management using current state detection that is not sufficient to capture potential safety

risks comprehensively. Therefore, the necessity for predicting unsafe conditions and potential risks must be raised for autonomous construction equipment.

2.4 Autonomous Excavation Progress

The fully autonomous excavation system can travel to the work location, corrects the pose, and map the terrain after each dig to monitor the work progress [11].

The excavation progress can be monitored using different sensors such as stereo cameras, LiDARs, UAVs, drones, satellite images, geotagging, etc. The selection of sensors is correctly oriented to the desired type of output.

[21] developed the automation algorithms of autonomous truck loading for a robotic excavator, which can deal with the automatic process of determination of digging areas, dumping soil into a truck, and moving between digging and dumping points. In this study, two laser range finders were used to localize a truck and to estimate the soil. Unless an excavator is situated on top of an elevated bench and a truck stops at a designated location, it can be difficult to recognize either the truck or any other nearby object nearby.

As an example, to apply the digital photograph technique in the area of excavation progress, [22] proposed a methodology to calculate the earthwork volume and progress of excavation using the geotagged photographs. The proposed method could create a mesh to calculate the geometric volume by using point clouds from taken pictures, which was compared with the accumulated software volume.

[23] suggested an idea for the estimation of bucket soil volume using the registration techniques. Range bearing and tilt sensors scan the environment, the bucket was then segmented using the cluster analysis, and the ICP algorithm was used to identify the pose of the bucket. To calculate the bucket soil volume from the payload, height grids that [5] adopted were used but this method is independent of any bucket model prior to the experiments. The container model was generated using the first few frames of point cloud when the bucket was empty and visible. This empty model served as the reference coordinates of the measured point cloud. The volume was calculated by subtracting the

reference point cloud from the current one. The corners of the bucket were marked, and the point clouds from inside, and outside regions of the bucket were segmented. The inside point cloud was used for the volume calculation. Although the results were satisfactory, a generalization of this approach is difficult since a dragline was designed for a specific purpose. Additionally, the bucket moves in the whole range of visibility of the LiDAR in this application, However, other machinery might not have such a visibility range.

To overcome the occlusion area problem, these sensors would not help as much as the other transducers like pressure sensors, and LVDT would do. The occlusion problem has been well addressed in [24]. During an excavation task using an excavator, some digging areas can be unperceived by the sensor vision due to the remaining pile. This situation can be eliminated by integrating the maps from proprioceptive and exteroceptive sensors.

[25] focused on identifying the material type by creating a 4D map. This map combined 3D data (XYZ) and intensity data that is the reflection of the laser beam of the sensor. It can help in the identification of material types since a brighter object (material) show higher intensity than a dark object. However, this study was not extensively developed to classify material (soil) types that is one of the useful information for the planning and operation of autonomous excavation. For the accurate material classification, further information such as ground resistive force and pressure of hydraulic actuators while excavation (digging) would be helpful but was not considered in their study.

2.5 Conclusion

This chapter provides a literature review on the existing studies on safety management and excavation progress in the construction equipment. The proposed algorithms for construction safety management mostly rely on proximity-based solutions, or by using the extra equipment, such as RFID. Installation and management of extra sensors may result in less accuracy of the safety. The tracking of the machines and the workers is the crucial point. However, mostly the proposed ideas are not focussed on estimating or predicting the states of the objects. Predicting the states is an important aspect

as it provides the safety management algorithm to address any potential risk within time. Thus, the state prediction needs to be considered for advanced and s safety features that autonomous excavators require.

The excavation progress algorithms dealt with the estimation of either bucket volume, or the ground excavation volume estimation. However, during the excavation task, the occlusion area may occur, which results in the incorrect mapping, and volume estimation. The researchers except [24] do not address the occlusion area problem, and therefore further research needs to be made. The research gaps in the prediction states of safety management, occlusion area problem, and identifying the material properties motivated us towards this project.

Chapter 3. Experimental Test Platform

3.1 Introduction

This chapter describes the experimental test platform setup. It starts with the test platform excavator, following up with the selection of sensors. The first part of the chapter describes a set-up of the developed test platform for experimental validations that includes a mini excavator, a hardware controller, electrical and hydraulic components. The second part of this chapter provides a rationale to select the required sensors and descriptions of the features of chosen sensors.

3.2 Test Platform

The developed test platform consists of three subsystems, electronic, hydraulic, and mechanical systems. The electronic system comprises a power supply, electro-hydraulic drivers, and sensors mentioned in the above section. The hydraulic system consists of EHPV's (Electro-Hydraulic Proportional Valve), DCV (directional control valves), hydraulic actuators, hydraulic reservoir, and a hydraulic pump. Lastly, the main body, and the three links, boom, arm, and bucket, belong to the mechanical system. The section describes the architecture of the test platform in terms of core components and the functions and features of the selected hardware controller.

3.3 The Excavator

Figure 3.1 shows the excavator prototype, and the specifications of the main components are listed in the following table.

3.3.1 Mechanical System

The mechanical system is composed of the three links; arm, boom, and the bucket. It has the rotation of 360 degrees, 30 degrees for both left and right steering, and a weight of 550 kgs. The lengths of boom, arm, and bucket links are 1460.5 mm, 869.95 mm, and 615.95 mm, respectively. The joint constraints are -29° to 79° , -59° to -155° , and -11° to -157° for boom, arm, and bucket, respectively. The total extended length of the excavator is approximately 2 meters.



Figure 3.1: Test Platform [1]

Table 3.1: Platform Specifications

Description	Specification
Battery	12 V DC
EHPV	Sun Hydraulics FPBF - XD
CBV	Syn Hydraulics 3:1 pilot ratio
DCV	DHE-071 Atos Solenoid Directional Valve
EHD	Sun Hydraulics XMD
Hydraulic Motor	Marazocchipompe , 4.81/min at 1500 RPM, 210-250 bars
LVDT	Baluff micropulse BTL 2UMJ
Pressure Sensor	Baluff Pressure transmitter BSP00H6
Rotary Encoder	Nocotechnik RFC RFC -4800
Host PC	Lambda Tensor- Book
Controller	MicroAutoBox II Embedded PC

3.3.2 Electronic System

Among several components in an electronic system of the test platform, electro-hydraulic drivers were used to supply the current to the EHPV based on the control signal. Through the drivers, the flow rate of the hydraulic fluid to the actuator and its velocity can be controlled. Figure 3.2 shows an integration of EDHs (Electro-Hydraulic Driver) with the other components of the electronic system. The power supply system consists of a 12 volts DC battery. This battery was used to supply power to the central controller, relay box, EHDs, and other instrumentation. The relay box (Fig. 3.3) was used to transmit the current to the DCVs (Directional Control Valves). The logical input from the controller controlled this transmission. The relay box controls the actuator's movement direction and bridges the low voltage side to the high voltage side.

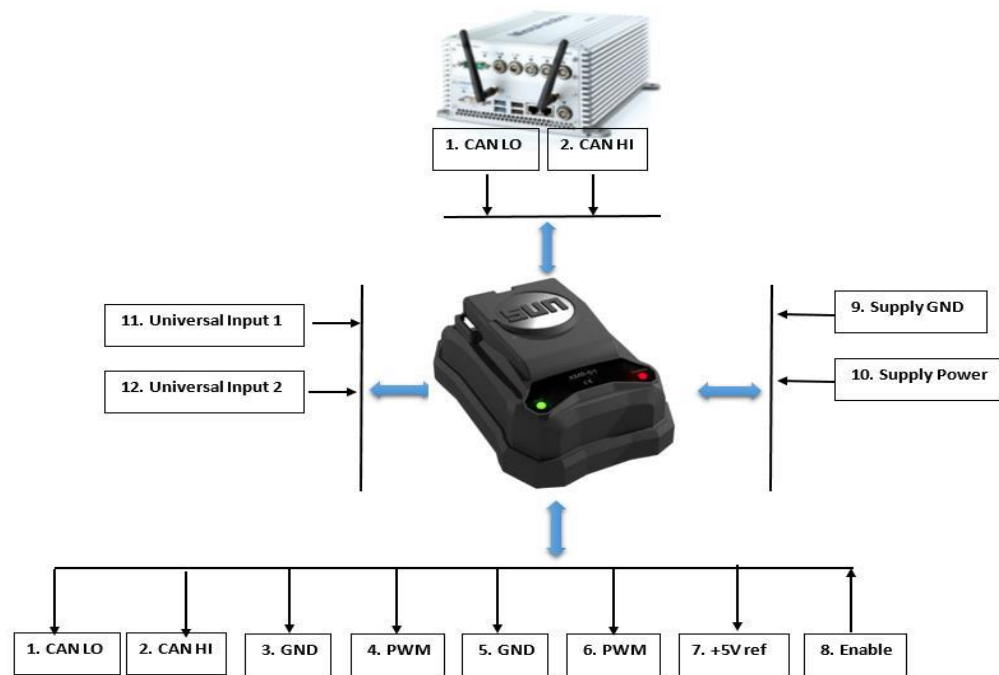


Figure 3.2: Electronics System of Test Platform [1]



Figure 3.3: Relay Box

3.3.3 Hydraulic System

The hydraulic system comprises of the hydraulic actuators, hydraulic pump, EHPVs, DCVs, hydraulic reservoir, and a hydraulic motor. The load valves were used to supply the pressure from the pump to the other valves. The hydraulic pressure using the hydraulic motor was supplied for the functions such as forward, backward movements, steering, stabilizer, rotation of the body, and the motions of the links' actuators. Figure 3.4 shows the position of actuators and links. EHPVs are used for the flow regulation, and DCVs for directional control of the hydraulic actuator.

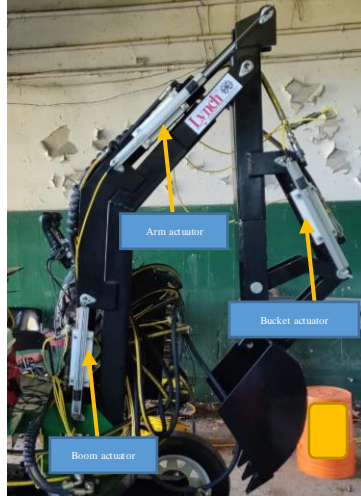


Figure 3.4: Links and Actuators of Excavator

3.3.4 Hardware Controller

The hardware controller used for this project is the MicroAutobox II embedded PC (dSPACE), as shown in Fig. 3.5. It is well used in the Automated Driving Assistance (ADAS) [28], and Development Platform for Safe and Efficient Drive (DESERVE) to interface the vehicle bus, sensors, and actuators. The safety and the excavation progress algorithms were developed using the host PC and uploaded to this hardware controller. The controller also has an option for CAN bus communication, which is used to transmit and receive data from the controller to other instruments. For this project, the safety, and excavation progress algorithms were developed using the MATLAB, and uploaded to the controller. Data from the controller can be downloaded, parameterize, and analyze using the Ethernet communication protocol. The algorithm development and implementation using the controller, follow the below steps:



Figure 3.5: dSPACE MicroAutoBox II [28]

- Step 1: Designing a model
 - The control logic was developed and simulated in the Simulink environment.
- Step 2: The developed algorithm was converted to C language for compatibility with the controller.
 - This option is available in Simulink. The compiled program was uploaded to the controller.
- Step 3: After the successful simulation, the logic was implemented in real-time using the controller
 - The simulation interface blocks were replaced by the blocks for the I/O configuration offered by the dSPACE, as shown in Fig. 3.6. Parameters were specified in the same steps by following the pin layout and the hardware.
 - dSPACE provides a software platform, Control Desk that deals with real-time monitoring, analysis, and recording the data for offline processing and analysis.



Figure 3.6: dSPACE Simulink Interface Blockset

3.4 Sensors

The sensor plays an essential role in the automation of excavators since it can detect changes and risks in the ground and working environment and provide this sensing information to the control, safety, and progress monitoring systems. For autonomous operations and safety control of autonomous excavators, fusion sensing using multiple sensors is essential. The following sub-sections provide the features and specifications of each sensor used in this study for ground mapping, detection of safety risks, and recognition of bucket tip position.

3.4.1 LiDAR Sensor – Velodyne VLP 16

Velodyne VLP-16 is a 3D LiDAR sensor that is the smallest and most advanced product of Velodyne [26]. The sensor is comparatively cost-effective than other sensors available in the market. It provides the critical features of real-time, 3D distance with calibrated reflectivity, along with the coverage of 360 degrees. The detailed specification of the Velodyne VLP-16 is given in Table 3.2 below.

Table 3.2: VLP-16 Specifications

Description	Specification
Range	100 meters

Range Accuracy	± 3 cm
Field of View (Vertical)	+15° to -15° (30°)
Field of View (Horizontal)	360°
Angular Resolution (Vertical)	2.0°
Angular Resolution (Horizontal)	0.1°-0.4°
Power Consumption	~8W
Weight	850 g
Points Generation	~30,000 points per second
Environmental Protection	IP67



Figure 3.7: VLP-16 LiDAR

This sensor was selected to fit the safety control application due to the following features. First, the sensor can achieve the FOV (Field of View) of 360 degrees that enable to detect objects from all orientations around an excavator using a single sensor. Otherwise, multiple sensors needed to cover the same scanning coverage.

The detectable range of this sensor is 100 meters, which is sufficient for urban excavation in tight and narrow space. The range accuracy (± 3 cm) of this sensor is another consideration of selection since it has a significant impact on the accuracy of the gathered data of obstacles and the quality of detection and tracking. Finally, the sensor does not include any rotational part, and this feature makes it convenient to mount on the excavator, experiencing significant vibration during excavation operations.

3.4.2 Stereo Camera – ZED Camera

The ZED camera as a stereo camera is a 3D sensor suited for long-range depth perception and motion detection. The stereo cameras provide objects and applications with the ability to see and understand the physical world.

Table 3.3: ZED Camera Specifications

Description	Specification
Output Resolution	2208 x 1242 (15 fps), 1920 x 1080 (30 fps), 672 x 376 (100 fps)
Interface	USB 3.0
Field of View	Max. 90° (H) x 60° (V) x 100° (D)
Depth Range	0.5 m to 25 m
Depth Accuracy	<2% up to 3m, <4% up to 15 m
Focal Length	2.88 mm
Power Consumption	380 mA /5V
Weight	170 g
Points Generation	~30,000 points per second



Figure 3. 8: ZED Stereo Camera

ZED Camera provides point clouds without preprocessing, which makes it easy to integrate with LiDAR's point cloud. For excavation progress, the sensor should provide dense point cloud data for a targeted position, in which LiDARs are not useful as they provide long-range but lack in dense point cloud due to the vacant spaces between the channels. The ZED camera was selected to meet this requirement. Another selection reason is due to the operational principle that this type of stereo camera processes images from two lenses, which act as the human eyes. In this way, it is hardly affected by the sunlight and outdoor environments compared to other stereo cameras processing the IR beam that is influenced by interference from the sunlight.

3.4.3 LVDT Sensor

LVDT sensors were mounted on each link (arm, boom, and bucket), along with the actuators, as shown in Fig. 3.9. LVDT sensors measure the stroke of each actuator.

The strokes were mapped to get the joint angles. These angles were used to calculate the bucket tip's position and trajectory. The cylinder stroke was calculated using Eq. (3-1). The specifications of LVDT sensors are presented in Table 3-4.

$$Stroke_c = \frac{Stroke_{max}}{V_2 - V_1} \times V_c \quad (3-1)$$

where $Stroke_c$ is the current stroke, $V_2 - V_1$ is the voltage difference between the maximum and minimum positions of the cylinder, $Stroke_{max}$ is the maximum stroke, and V_c is the current-voltage reading from the LVDTs.



Figure 3.9: LVDT Sensor on Excavator [1]

Table 3.4: LVDT Specifications

Description	Specification
Type	Magneto – Strictive Linear Position
Interface	Analogue, Voltage
Operating Voltage	10 – 30 V DC
Output Voltage	0 – 5 V
Measurement Length	500 mm

3.4.4 Pressure Sensor

The pressure sensors (Fig. 3.10) were used to calculate the force exerted by each boom, arm, and bucket and the torque associated with these links. The force calculation was obtained using:

$$F_{cyl} = P_H A_H - P_R A_R \quad (3-2)$$

where F_{cyl} is the force exerted by the corresponding actuator, P_H and A_H are the pressure and area at the piston head side, respectively. P_R and A_R are the pressure and area at the piston rod side. The specifications of the pressure sensor are given in the table.

Table 3.5: Pressure Sensor Specifications

Description	Specification
Unit	Bar
Range	0 – 600 bars
Input Voltage	8 – 32 V DC
Output Voltage	0 – 10 V DC



Figure 3.10: Pressure Sensor on Excavator [1]

3.4.5 Rotatory Encoder

The measurement of the excavator body’s yaw angle was carried out using a rotatory encoder. A contactless rotary encoder was installed at the bottom-center of the body. The encoder helps in measuring the yaw angle during the dumping process that is required to recognize the position of the bucket for safety monitoring and autonomous excavation. The selected rotary encoder is a non-contact type encoder that gives an output signal range of 0.5 to 4.5 V, along with a range of 360 degrees, and requires a supply voltage of 12 V. Figure 3.11 shows the encoder used in this project.

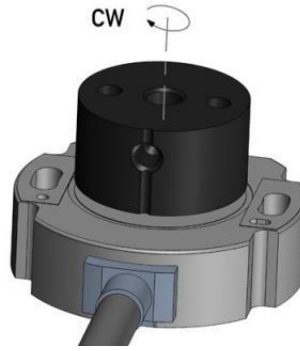


Figure 3.11: Rotatory Encoder [1]

3.5 Conclusion

In conclusion, this chapter describes a set-up of the developed test platform for an autonomous excavator. For the excavator's part, three subsystems of the excavator; mechanical, hydraulic and electronic systems have been addressed. The components of each subsystem have been presented along with their workings and specifications. In the end, the selected hardware controller was introduced in terms of functional features and step to achieve real-time operation.

For the sensors part, several sensors such as LiDAR, ZED stereo camera, rotatory encoder, LVDT, and pressure sensor have been discussed. The LiDAR, due to its long-range and high accuracy, used for the safety algorithms, the stereo camera has been used for excavation progress because of its dense point cloud data, rotatory encoder measured the rotation of the excavator's body, LVDT provided the stroke data from the actuators, that was used to calculate the bucket trajectory, and lastly, the pressure sensor measures the pressure value of each link.

Chapter 4. Safety Modules for Autonomous Excavators

4.1 Introduction

This chapter explains the study of a 3D LiDAR-based safety module for an autonomous excavator. The algorithm predicts the motion of objects around the excavator and evaluates the severity of collision risks in terms of time and distance. The framework for this study is made up of 3 components: Obstacle detection, tracking, and predictive safety evaluation. The object detection was done using the plane fitting, K-means, and bounding box algorithms. Object tracking was carried out using the Extended Kalman Filter (EKF) and Joint probabilistic Data Association (JPDA). The object tracking filter provides the estimated and predicted states of the objects approaching around the excavator. The last component deals with the safety indices with which kinematics of excavator, working areas of the excavator, time to collision (TTC), and warning index (x) was calculated. The framework of the predicted safety module is illustrated in Fig. 4.1. The LiDAR data has been utilized by the object estimation and tracking algorithms for objects states estimation. Kinematic analysis provided the working area of the excavator by processing the measurements from LVDT sensors. The objects estimated position, and the working area of the excavator are processed under the safety indices algorithm to calculate the time and distance to collision.

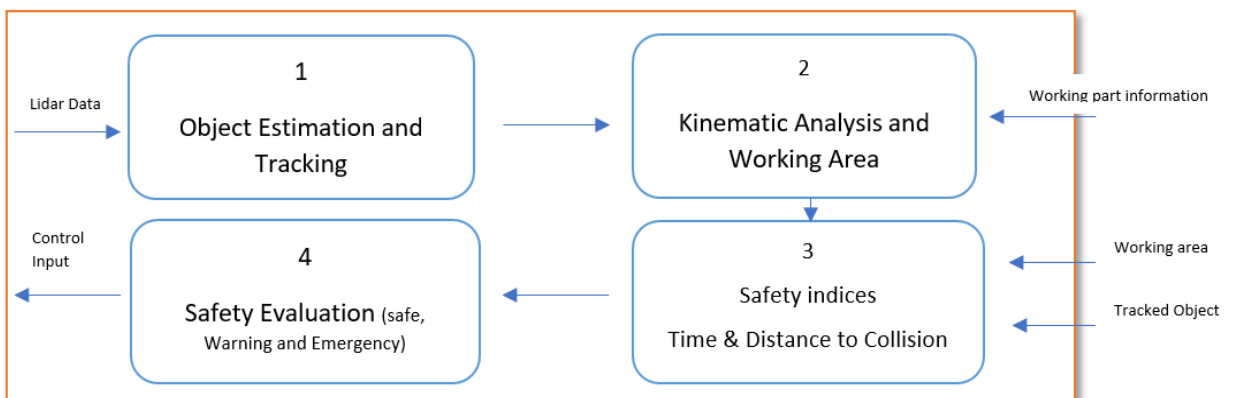


Figure 4.1: Safety Module Process Overview

4.2 Object Detection

This section describes a method of processing LiDAR data and extracting obstacle points. Velodyne VLP-16 was selected as a 3D LiDAR for this task. The selection criteria for a LiDAR have been addressed in the previous chapter. Raw point cloud data from a LiDAR need to be extracted and processed through several essential steps to carry out the obstacle detection. These steps are shown in Fig. 4.2. A detailed explanation is provided as follows:

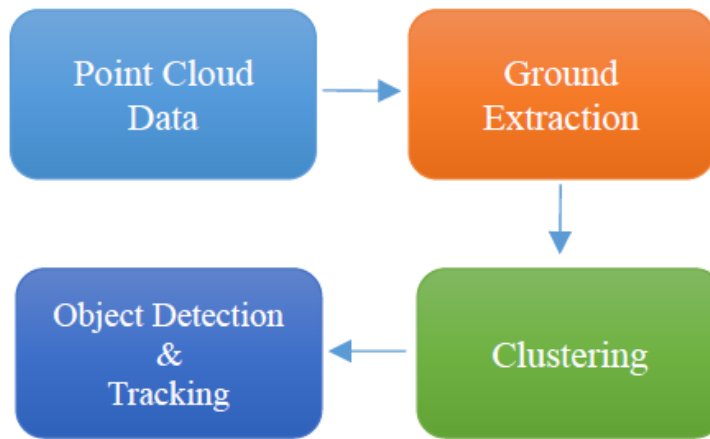


Figure 4.2: Object Detection and Tracking Workflow

4.2.1 Plane Fitting and Ground Points

Ground point detection is a step where the points belonging to the ground (earth surface) were extracted because the developed algorithm focuses on detecting objects rather than ground plane. The extraction of the ground plane is a primary step as it reduces computational costs by removing unwanted points.

In the safety module in Fig. 4.2, the ground plane was detected by RANSAC (Random Sample Consensus) [35] that is a repetitive method to estimate a model from a given data set containing outliers. The M-Estimator sample consensus (MSAC) algorithm, a variant of RANSAC, fits a plane model to the point cloud to get the ground points. RANSAC randomly selections a subset of data set, fits a model to selected points, and find

the number of outliers. After detecting the non-ground points, the next step was to cluster the non-ground points and detect the obstacles, which is discussed in the next section.

4.2.2 Neighboring and Clustering

Once the ground points were detected, the remaining points were labeled as the non-ground points. Then, these non-ground points were formed into clusters. However, clustering the remaining whole point cloud is computationally high, since the scanning range of LiDAR is very long. A radius was defined to restrict a region of interest (ROI) in which points were considered as neighbors [36]. The clustering was done on the neighboring points.

The clustering step was carried out by using the Euclidean distance. The Euclidean distance was set to 0.4 meters, which is almost identical to the average chest width of a worker. The upper bound of a cluster was set to the average vehicle size to eliminate more massive clusters. In such a case, only humans and objects having a similar size of the vehicles were formed into clusters. Objects that are smaller than humans or bigger than vehicles were neglected. The next step after clustering is to set a bounding box on each cluster, which is discussed in the next section.

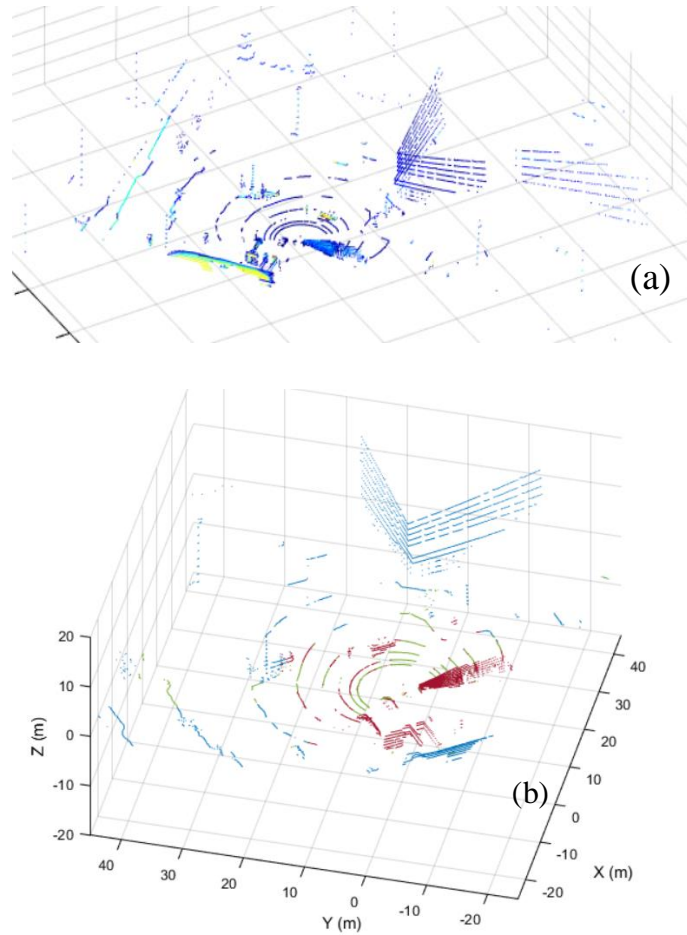


Figure 4.3: Raw Point Cloud (a), and Clustered Point Cloud (b)

4.2.3 Bounding Box

A bounding box was created to fit each cluster to show detected objects [35]. The generated bounding box provided the x, y , and z coordinates of the center point of a detected object. The conversion of each cluster to its corresponding bounding box was made using $[x \ y \ z \ l \ w \ h]$, where x, y , and z refer to the position of the bounding box. l, w , and h are the length, width, and height of the bounding box, respectively.

The bounding box was fitted onto each cluster by using the maximum and minimum points of the object. The corner points of the bounding box were calculated by checking the maximum and minimum distance points from the center point. Figure 4. 4 shows the objects with their bounding boxes.

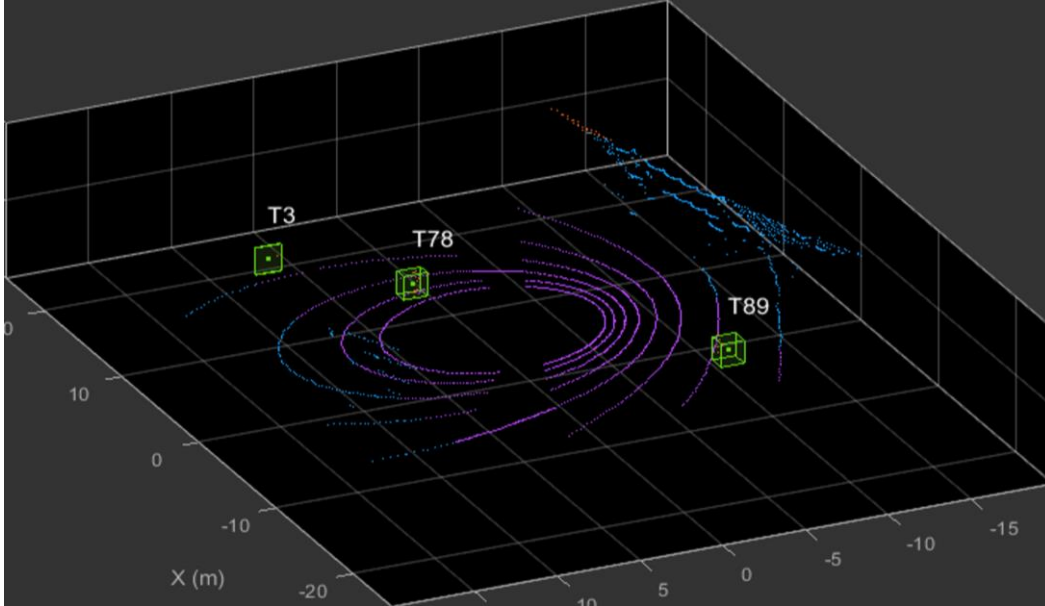


Figure 4.4: Detected Objects with Bounding Boxes

4.3 Object Tracking and Track Management

Object tracking deals with state estimation and prediction of objects around the excavator. Every position of objects was first measured by a LiDAR, then estimated and predicted by the designed filter. Track management can be achieved by the data association algorithm that can assign tags and different properties of each corresponding track. It also helped in determining the number of objects on-site and handling the tracking and prediction information of each object.

4.3.1 Extended Kalman Filter

Object tracking was conducted by applying the Extended Kalman Filter (EKF) [36, 37]. The EKF outperforms the linear filter due to its ability to deal with nonlinear states and processes, such as motions of workers and machines. The procedure to design an EKF is shown in Fig. 4.5, and the model is given as:

$$x_{k+1} = f(x_k, u_k, T) + w_k \quad (4-1)$$

$$z_k = f(x_k, T) + v_k \quad (4-2)$$

where T is the sample time, w_k is the process noise, v_k is the measurement noise, x_{k+1} is the state vector, z_k is the measurement, w_k is the process noise that was assumed to be Gaussian having zero mean and covariance Q_k .

$$\begin{bmatrix} x_{k+1} \\ v_{x,k+1} \\ y_{k+1} \\ v_{y,k+1} \\ z_{k+1} \\ v_{z,k+1} \end{bmatrix} = \begin{bmatrix} 1 & T & 0 & 0 & 0 & 0 \\ 0 & 1 & 0 & 0 & 0 & 0 \\ 0 & 0 & 1 & T & 0 & 0 \\ 0 & 0 & 0 & 1 & 0 & 0 \\ 0 & 0 & 0 & 0 & 1 & T \\ 0 & 0 & 0 & 0 & 0 & 1 \end{bmatrix} \begin{bmatrix} x_k \\ v_{x,k} \\ y_k \\ v_{y,k} \\ z_k \\ v_{z,k} \end{bmatrix} \quad (4-3)$$

$$F(x) = \frac{\partial f}{\partial x} \quad F(w) = \frac{\partial f}{\partial w} \quad (4-4)$$

$$H(x) = \frac{\partial h}{\partial x} \quad H(v) = \frac{\partial h}{\partial v} \quad (4-5)$$

$$x^-_{k+1} = f(x^+_k, u_k) \quad (4-6)$$

$$P^-_{k+1} = F_k P_k F_k^T + W_k \quad (4-7)$$

$$K_{k+1} = P^-_{k+1} H_k^T (H_k P^-_{k+1} H_k^T + V_k)^{-1} \quad (4-8)$$

$$x^+_{k+1} = x^-_{k+1} + K_{k+1} (z_{k+1} - H_k x^-_{k+1}) \quad (4-9)$$

$$P^+_{k+1} = (I - K_{k+1} H_k) P^-_{k+1} \quad (4-10)$$

where F is state Jacobian matrix, H is the observation matrix, x^-_{k+1} is the priori state, P^-_{k+1} is the priori covariance, K_{k+1} Kalman gain, x^+_{k+1} is the posteriori estimate, and P^+_{k+1} is the posteriori covariance.

The EKF was modeled as the constant velocity, assuming that the objects being tracked are moving at a constant velocity, as mentioned in Eq. (4-1). Eqns. (4-4) and (4-5) describe the Jacobian matrices of state and observation. The filter adopted the linearization method for the nonlinear state equations, while the covariance matrices remain linear. The position and velocity of each object were predicted using the above equations, (4-8) - (4-10).

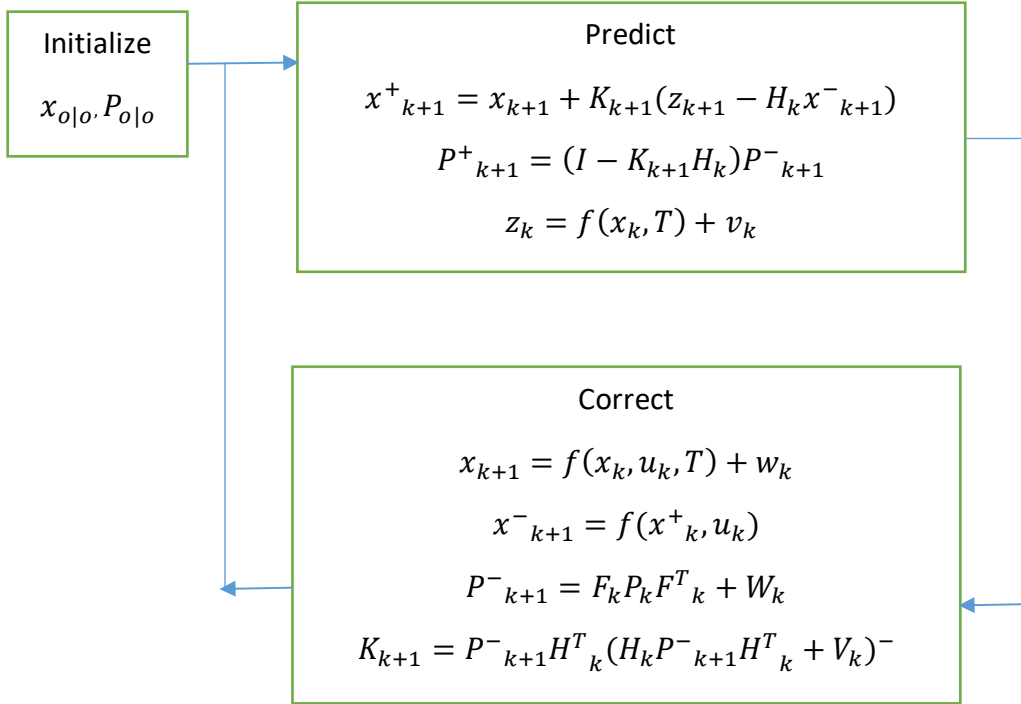


Figure 4.5: EKF Procedure

4.3.2 Joint Probabilistic Data Association

Data association is the process of assigning tags and different entities such as position, velocity, tracking information, and predicted states to each object. For this project, the data association for the object tracking filter was handled by the Joint Probabilistic Data Association (JPDA). The JPDA is capable of handling data from multiple sensors and objects to assign the detection information. The JPDA algorithm associates multiple detected objects to their corresponding tracks from the previous frames [38].

The logic flow of JPDA is as follows [39]:

- Division of detections into multiple groups for multiple sensors.
- For each sensor:
 - Calculation of distances from detections to existing tracks.

- Calculation of validation matrix.
- Separation of tracks and detection into clusters.

Following are the steps to update each cluster:

- Generation of feasible joint events.
- Posteriori probability calculation for each joint event.
- Calculation of marginal probability of each detection-track pair.
- Reporting of weak detections that are within the validation gate of at least one track.
- Unassigned and weak detections get new tracks
- Deletion of tracks: tracks are deleted based on the defined number of scans without detection.
- All tracks are predicted to the latest time value.

The workflow of the JPDA needs to identify if the detections can be associated with any of the existing tracks. The assignment of estimated, and predicted states to each detection can be done by evaluating a *validation gate* around predicted measurement. The validation gate is a spatial boundary centered at the predicted measurement. The validation gate is defined using the probability of state estimation and covariance of the existing track. The correct detections have a high chance of falling within the validation gate. The next step of JPDA is to determine if the measurement of objects position falls within the validation gate.

The data association becomes complex in the case of multiple tracks because one detection can fall into the validation gates of multiple tracks, as shown in Fig. 4.6. In this figure, T_1 and T_2 are the tracks, and ellipses are the validation gates. D_2 is at the intersection of both validation gates that forms a cluster, i.e., a set of connected tracks and associated detections.

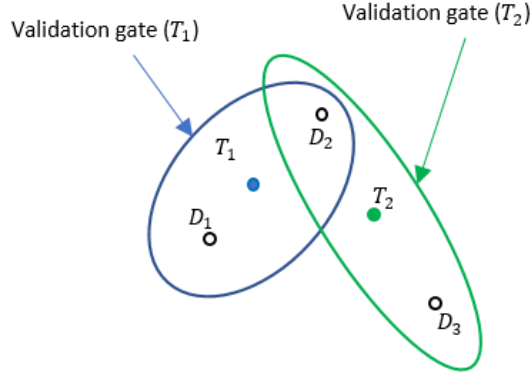


Figure 4.6: JPDA Events

To represent a relationship of association among the tracks in a cluster, a validation matrix was used. Each row of the matrix corresponds to a detection while a column represents a track. The first column was added and usually referred to as “Track 0”. If the detection D_i is inside the validation gate of track D_j , the $(j, i + 1)$ entry of the matrix is set as 1, otherwise zero. The validation matrix (Ω) for the above case (Fig. 4. 6) is given as:

$$\Omega = \begin{bmatrix} 1 & 1 & 0 \\ 1 & 1 & 1 \\ 1 & 0 & 1 \end{bmatrix} \quad (4-11)$$

Note that all the elements of the first column are 1, because of clutter or false alarm. The value of 1 in the first, and second row of the second column shows that *Track1* validation gate has detections 1 and 2 while *Track2* has second and third detection represented by 1 in the second and third row of the third column.

4.4 Safety Indices

This section explains the modeling and calculation of the safety module using the defined safety indices of time to collision (*TTC*) and warning index (x). The time required for an object to collide with the excavator is known as *TTC*. x is the warning index that is used to evaluate a collision based on the distance information.

4.4.1 Kinematic Analysis and Working Area of Excavator

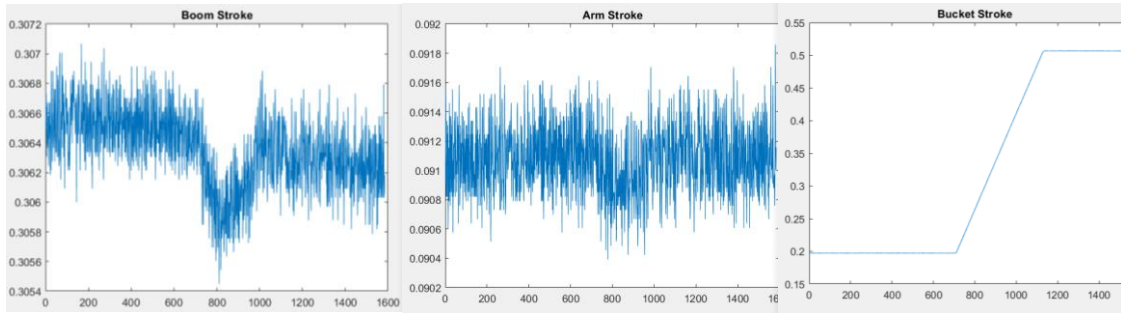
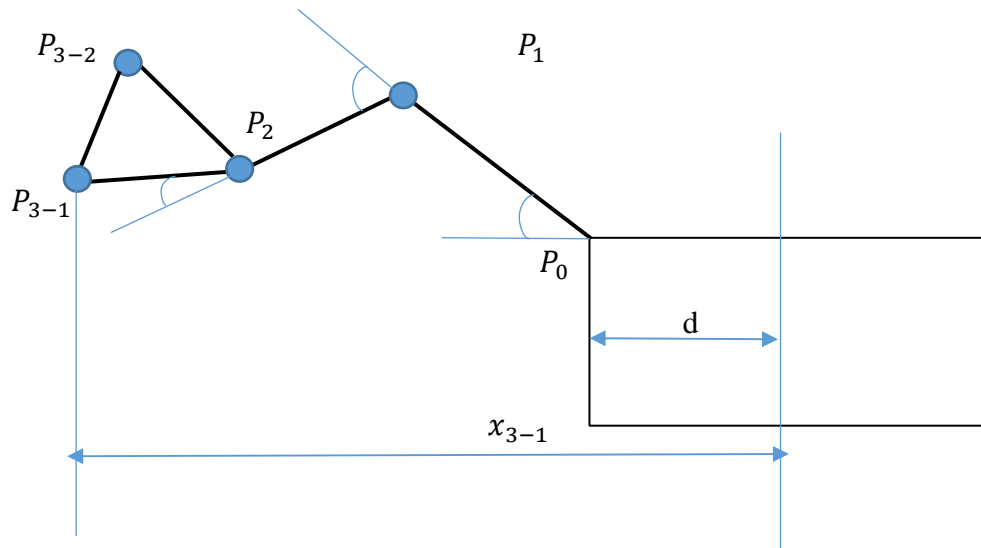


Figure 4.7: LVDT- Stroke Data

The angles for each joint of the excavator's manipulator were calculated using the stroke data from the LVDT sensors. Kinematic analysis was conducted to calculate the actual and predicted working areas of the excavator, using the converted angles. Figure 4.8 shows the main points on each link. P_1 , P_2 , P_{3-2} , and P_{3-1} denote the arm joint, bucket joint, midpoint of the bucket, and bucket tip, respectively. d is the distance from the center of the main body to the base of the boom, and θ is the angle of each joint. x_{3-1} denotes the maximum working area of the excavator when each link is fully extended.



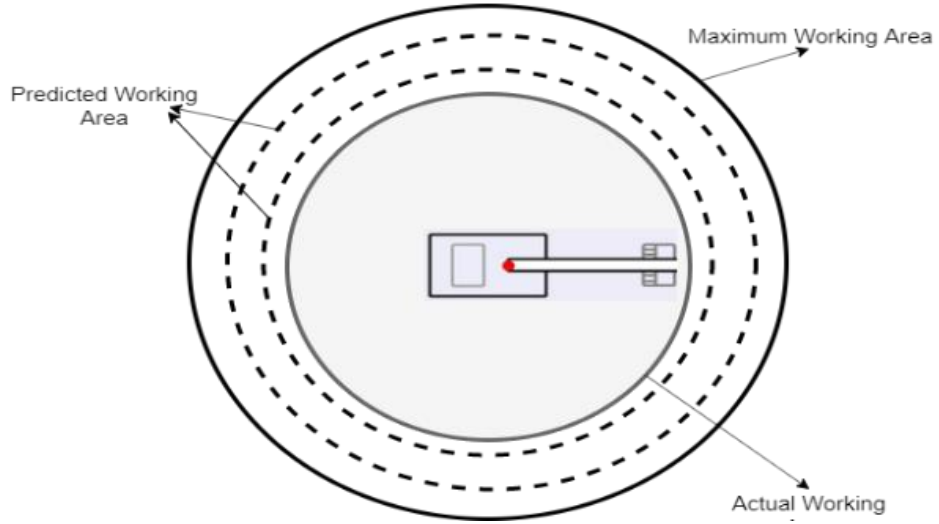


Figure 4.8: Working Area of the Excavator [19]

The maximum working area of the excavator is fixed. The actual working area of the excavator was determined by calculating the maximum value of all x components. The predicted angle of each part was calculated by:

$$\Delta\theta_i = (\dot{\theta}_{working\ part} + 3\sigma)i\Delta t \quad (4-12)$$

where σ is the standard deviation of noise in the angular velocity signal. 3σ represents the maximum possible noise value. Δt , and i are the discrete-time and prediction steps, respectively.

$$\begin{bmatrix} \Delta x_1 \\ \Delta x_2 \\ \Delta x_{3-1} \\ \Delta x_{3-2} \end{bmatrix} = \begin{bmatrix} A_{11} & A_{12} & A_{13} & A_{14} \\ A_{21} & A_{22} & A_{23} & A_{24} \\ A_{31} & A_{32} & A_{33} & A_{34} \\ A_{41} & A_{42} & A_{43} & A_{44} \end{bmatrix} \begin{bmatrix} \Delta\theta_{boom} \\ \Delta\theta_{arm} \\ \Delta\theta_{bucket} \end{bmatrix} \quad (4-13)$$

$$x_{pre,p,i} = x_{pre} + \sum_{j=1}^i \Delta x_{p,j} \quad (4-14)$$

Using the predicted angles and Jacobian matrix in Eq. (4-13), the length, l of each working part can be calculated. Then, the predicted horizontal displacements can be

derived using Eq. (4-14). The maximum value among the predicted displacements was selected as a maximum radius for the predicted working area. In Eq. (4-14), p represents the current main points ($P_1 \sim P_{3-2}$). Figure 4.8 presents the horizontal displacements using p (upper figure), and the maximum predicted working areas (lower figure).

4.4.2 Time to Collision (TTC)

TTC is defined as the amount of time that will pass before the object, and the target collide. The following equations were used to calculate TTC .

$$\|r_{obs}\| = \sqrt{x_{obj}^2 + y_{obj}^2} \quad (4-15)$$

$$\theta_{ATC} = \tan^{-1}\left(\frac{y_{obj}}{x_{obj}}\right) - \varphi_{sw} \quad (4-16)$$

$$c = \|r_{obs}\|\theta_{ATC} - B_c \quad (4-17)$$

$$TTC = \frac{\theta_{sw,k} - \theta_{obj,k}}{\theta_{ATC}} ; \text{ if } \theta_{ATC} < 0, TTC^{2nd} \leq tm. \quad (4-18)$$

$$TTC = \frac{\theta_{sw,k} - \theta_{obj,k}}{\theta_{ATC} + \pi} ; \text{ if } \theta_{ATC} \geq 0, tm \leq TTC^{2nd}. \quad (4-19)$$

where x_{obj} and y_{obj} are the object's estimated coordinates, r_{obs} is the distance between the object and excavator's body center, φ_{sw} is the excavator's swing angle, θ_{ATC} is the angle to the collision, B_c is the bucket clearance, c is the clearance between the excavator and an object, θ_{sw} is the swing velocity, tm is the predicted time to reach maximum velocity, $\theta_{obj,k}$ is the object angular velocity, and TTC^{2nd} is the second-order TTC that represents TTC while considering the current swing acceleration.

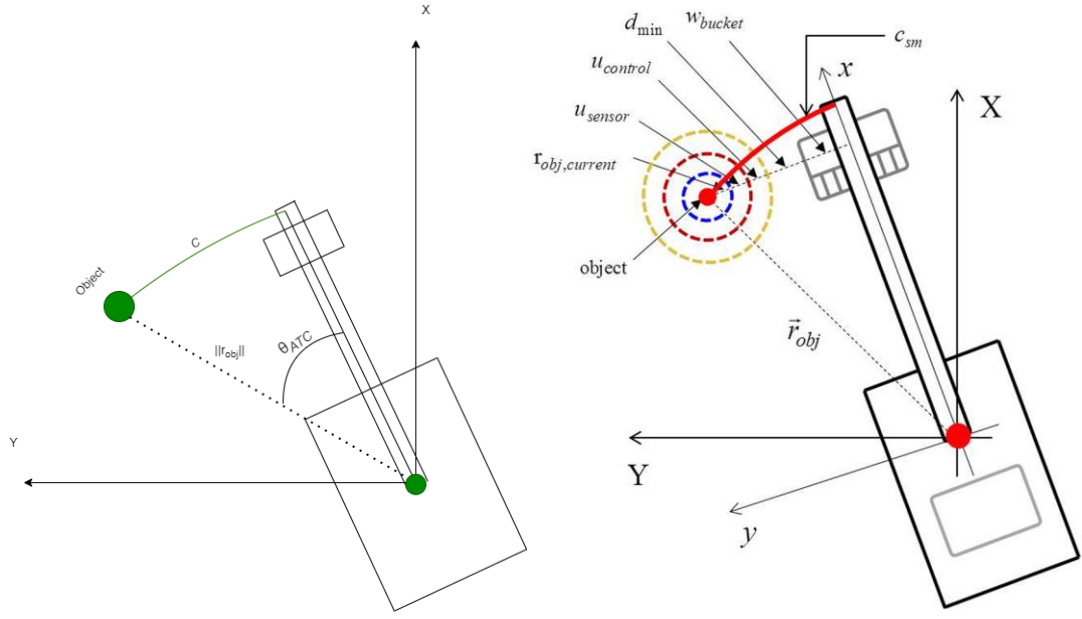


Figure 4.9: Variables Illustration for TTC (left), Variables Illustration for Warning Index [19]

4.4.3 Warning Index (x)

The warning index was calculated by:

$$c_{br} = \frac{\|r_{obj}\| \theta_{sw}^2}{2\alpha_{decel,max}} \quad (4-20)$$

$$c_{sm} = \left\| \|r_{obj}\| \right\| \sin^{-1} \left(\frac{r_{obj,current} + u_{sensor} + u_{control} + d_{min}}{\|r_{obj}\|} \right) \quad (4-21)$$

$$x = \frac{c - c_{sm}}{c_{br}} \quad (4-22)$$

where r_{obj} is the object's position vector, $\alpha_{decel,max}$ is the maximum deceleration of the main body rotation, c is the clearance between the excavator and an object, c_{sm} is the safety margin of clearance, c_{br} is the breaking distance, x is the warning index, d_{min} is the minimum clearance, u_{sensor} and $u_{control}$ are the sensor signal noise and control

uncertainties, respectively. The smaller x represents a more dangerous situation (i.e., high collision risk).

4.5 Safety Level Decision

For this project, three safety levels (safe, warning, and emergency requiring a breaking action in Fig. 4.9) were considered according to the calculated values of TTC and x . The safe region means that the excavator can continue to work without any collision risks. In the warning region, alarm signals are generated for an operator to recognize dangerous situations. In the emergency, the immediate breaking action should be generated at the maximum deceleration to avoid collision accidents. The values of thresholds were calculated based on the physical experiments. These results are discussed in chapter 6.

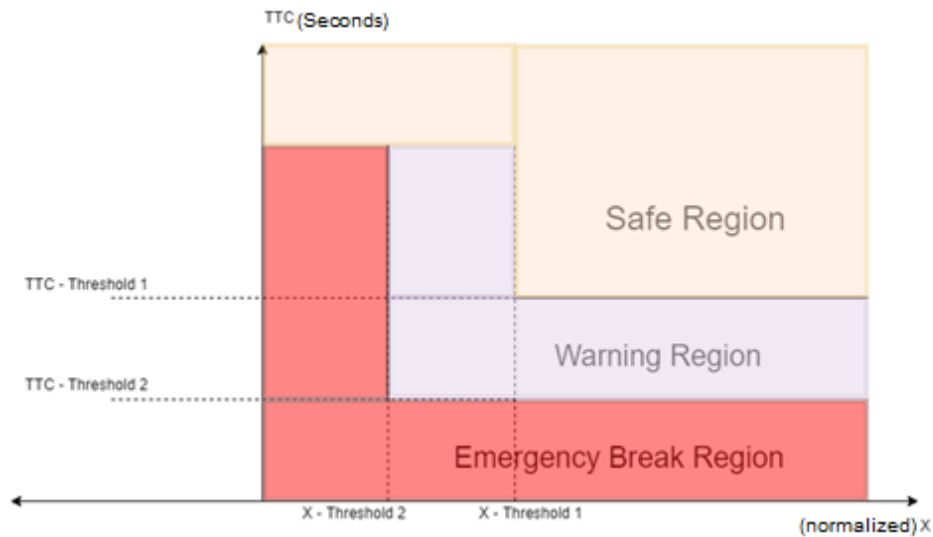


Figure 4.10: Safety Level Indices

4.6 Conclusion

The proposed safety module was discussed in this chapter. The designed algorithm can be used to avoid the potential collision among the workers and the machines on the

construction site. The proposed algorithms used the data from VLP-16 LiDAR, pressure sensors, and a rotation encoder.

The object detection was done using raw data from the sensors and processing it by removing the ground points, clustering, and bounding boxes. A constant-velocity EKF coupled with JPDA provides the functions of tracking, prediction of the moving objects, and track management of the detections for assigning corresponding tracking details for each detection, from the object detection algorithm.

Using the predicted states of the moving objects and working areas of the excavator from the kinematic analysis, the safety indices, TTC and x were calculated. The introduced safety indices define the degree of potential risks of collision accidents.

Chapter 5. Autonomous Excavation Progress

5.1 Volume Estimation Algorithm

This section describes the algorithms for calculating the volume of excavated areas. The volume calculation is the first step towards the excavation progress, i.e., how much excavation is progressed. Two different estimation methods were adopted for this task. The first is to estimate the excavation volume from the ground surface after each dig (i.e., direct estimation), and the second is to estimate it through the soil volume contained in the bucket that is accumulated after each dig (i.e., indirect estimation). The detail working is explained in the below sections.

5.1.1 Point Cloud registration using NDT

Registration is the process of aligning two or more point clouds of the same scene [40]. It helped in the reconstruction of the same scene from different sources or locations. The registration technique has been used to properly align and merge the reference (fixed), and the actual (moving) point cloud.

In our case, Normal Distribution Transform (NDT) [42] was applied for point cloud registration as it showed more robust results for aligning point clouds than the other two mentioned in Table 1.1, and 1.2. The output of the registration step is the transformation matrix that provides the information of the transformation between the moving and fixed-point clouds.

Once we have the transformation matrix, the next step is to align the two point clouds using the transformation matrix provided by the registration method. The aligned point clouds are stitched and merged. Merging of point clouds for each frame leads to the accumulation of point clouds and map building.

This section describes the formulation of NDT for a single laser scan. The collection of local normal distributions helps NDT in modeling the distribution of all

reconstructed points for a single scan. The normal distribution is also known as a gaussian distribution that has the symmetric probability about the mean and appears as a bell curve in the graph form.

First, the environment (point cloud) is subdivided into regular cells with a constant size. Each cell must contain at least three points. Any cell having less than three points fails to provide accurate normal distribution, and hence regard as empty. For each cell, the following steps are done.

1. Calculation of all the points in a cell $x_i = 1..n$.
2. Calculation of mean $q = \frac{1}{n}\sum_i x_i$.
3. Calculation of covariance $\Sigma = \frac{1}{n}\sum_i (x_i - q)(x_i - q)^t$.
4. The probability of measuring a sample point in a cell is modeled by the normal distribution $N(q, \Sigma)$.

The NDT forms the regular subdivision similar to the occupancy grids. However, it represents the probability of a position for the sample point within a cell rather than the probability of a cell being occupied or not.

Steps for aligning point clouds:

1. Build the NDT for the first scan (point cloud).
2. By zero or using the odometry data, initialize the parameter estimate.
3. Using the second scan, map the points into the coordinates of the first scan.
4. Calculating the normal distribution of each mapped point.
5. Calculating the score of parameters by the evaluation of distribution.
6. Calculation of new estimates by optimizing the score. The optimization was done using newton's method.
7. Repeat from step 3 until the criterion is met for convergence.

5.1.2 Ground excavation volume estimation

The first method to calculate the excavation progress is to estimate the volume of dug areas by comparing the pre-excitation or reference ground profile (reference point cloud) and actual one (current point cloud) after excavation.

The workflow for the ground excavation volume estimation is as follows:

1. Capturing the reference or pre-excitation ground point cloud, as shown in Fig. 5.1.

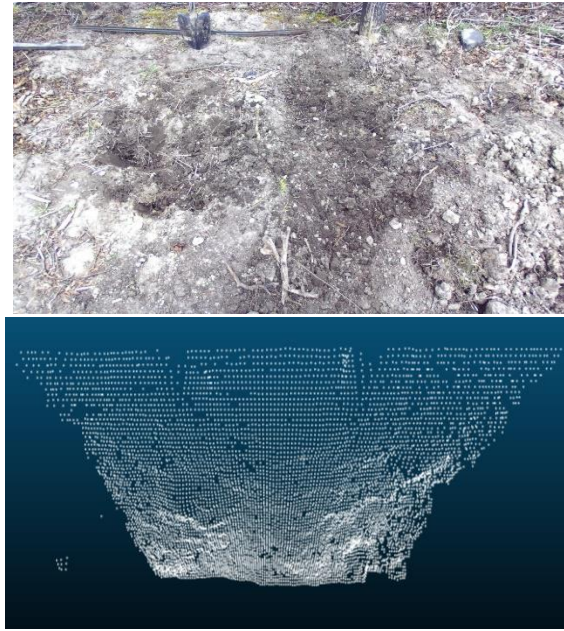


Figure 5.1: Pre-Excavation Ground Image and Point Cloud

2. Since the focus is on the ground and thus the stereo camera was at a tilted position (Fig. 5. 5), so we applied the transformation matrix for the camera tilting [42]. Since the transformation was done only for eliminating the rotation, the affine type of transformation was chosen. The affine type provides the transformation as translation, scale, rotation, and rotation [43]. Equation 5-1 shows the transformation matrices for x , y , and z coordinates.

$$T = [x][y][z] = \begin{bmatrix} 1 & 0 & 0 & 0 \\ 0 & \cos(a) & \sin(a) & 0 \\ 0 & -\sin(a) & \cos(a) & 0 \\ 0 & 0 & 0 & 1 \end{bmatrix} \begin{bmatrix} \cos(a) & 0 & -\sin(a) & 0 \\ 0 & 1 & 0 & 0 \\ \sin(a) & 0 & \cos(a) & 0 \\ 0 & 0 & 0 & 1 \end{bmatrix} \begin{bmatrix} \cos(a) & \sin(a) & 0 & 0 \\ -\sin(a) & \cos(a) & 0 & 0 \\ 0 & 0 & 1 & 0 \\ 0 & 0 & 0 & 1 \end{bmatrix} \quad (5-1)$$

3. Capturing the point cloud to show the current ground profile after the digging (Fig. 5.2).



Figure 5.2: Ground Image and Point Cloud After Digging

4. The same transformation in Eq. (5-1) was also applied to the point clouds for the current ground profile.
5. The next step was to register the point clouds. Point cloud registration is the method of aligning two or more point clouds of the same scene and integrating them into a common coordinate system (section 5.1.1).
6. After registration, the last step was to subtract the excavated point cloud from the reference one. The subtracted region is the difference between two point clouds and provides the info of accumulated excavation volume.

5.1.3 Bucket CAD Model

The role of the bucket CAD model is to serve as a reference for bucket volume estimation. The CAD model was designed using SIEMENS NX software [44]. Since the designed CAD file format is a PRT file, there was a need to achieve this bucket in the point cloud form for processing with the camera point clouds. The bucket model was first converted to a mesh using the triangulation method [45], and then the mesh was sampled

with approximately ten thousand points. These sampling points represent the coordinates of the bucket. The sampled points were finally converted to point cloud format. The created bucket CAD model is shown in Fig. 5.3 (a). Figure 5.3 (b) shows the point cloud of the bucket CAD model.

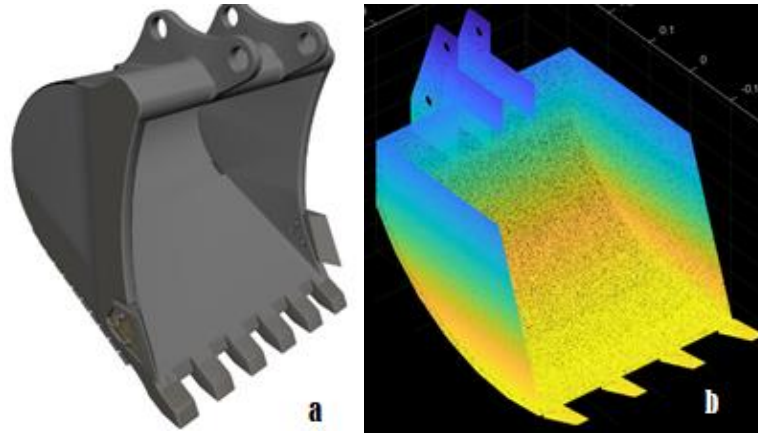


Figure 5.3: Bucket CAD model (a), and Bucket CAD Model Point Cloud (b)

5.1.4 Bucket Volume Estimation

The bucket volume estimation is an important method for volume estimation as the bucket is captured at all times during the excavation process. Also, there might be chances of occlusion area in the ground map that can affect the ground excavation volume estimation. Hence, bucket volume estimation can cover that gap, as it does not have any occlusion issue.

The bucket volume estimation is the second method in volume estimation. For this project, the bucket CAD model in Fig. 5.3 was used as a reference. The sensor position was fixed to a point where the bucket can be fully captured during the excavation process. The bucket volume estimation process is as follows:

- Fix the camera position to capture the bucket containing the soil, as shown in Fig. 5.4.
- Capture the point cloud during the dumping process, as shown in Fig. 5.5.
- Introduce the bucket CAD model as a reference point cloud.

- Apply the registration technique to integrate the bucket point cloud containing soil and the CAD model, Fig 5.6.
- Apply the triangulation [45] technique for filling vacant spaces in the point cloud.
- Identify the difference between the two point clouds and compute the excavation volume.



Figure 5.4: Stereo Camera Position



Figure 5.5: Bucket Containing Soil Point Cloud (left) and Actual Image (right)

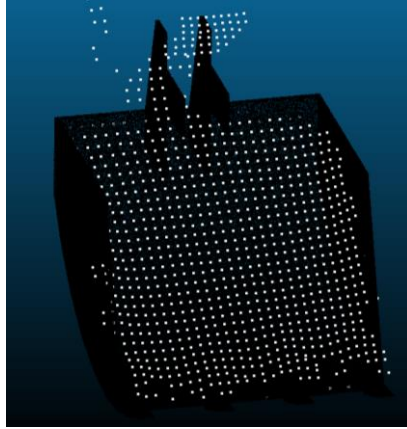


Figure 5.6: Bucket CAD Model and Registered Point Cloud

5.1.5 Volume Estimation Algorithm Summary

Two different techniques, ground excavation volume estimation and bucket volume estimation, were adopted to calculate the excavation progress. The registration technique was used to stitch and align the point clouds for accurate volume estimation. The ground excavation volume estimation was carried out by subtracting the excavated ground from the pre-excavation ground. In contrast, bucket volume was estimated by comparing the bucket CAD model and a bucket containing soil after each dig.

Other factors such as camera position, registration algorithm, and type of transformation play an essential role. The camera position was selected to a point where the arm of the excavator does not block the camera view, and also fully capture the bucket during the excavation process.

5.2 Occlusion Detection

Another technical challenge in ground mapping and estimation of autonomous excavation progress is the limited range of sensing due to occlusion areas. Specifically, piles and other surrounding obstacles on the ground may block the field of view of sensors and result in limited environmental monitoring. [46] proposed an idea of combining the exteroceptive and proprioceptive sensors for legged robots and [24] extended this idea to

the application of an autonomous excavator's arm. Proprioceptive sensors measure values internal to the system, such as motor speed, body rotation, joint angles, and battery voltage, while exteroceptive sensors acquire information from the environment; e.g. distance measurements, light intensity, and point clouds. For this project, we adopted the idea of using the exteroceptive and proprioceptive sensors to overcome the occlusion problem from the piles on the ground and reconstruct a map for the occluded area.

5.2.1 Sensor Vision occlusion

As shown in Fig. 5.8, the pile in front of the excavator blocks the vision of the sensor. In this case, the perceived data is unaware of the ground on the other side.

The only information available for this region is the bucket trajectory. The occlusion can happen before or during the excavation. The next section describes the procedure of the initial map and identifying the bucket trajectory of occluded areas.

5.2.2 Initial Exteroceptive Map

The exteroceptive sensor was used to scan the ground surface of the excavation area. Due to the presence of any blockage such as piles, this sensor was unable to perceive the data on the other side of the pile. Figure 5.7 shows the initial ground map constructed by the ZED stereo camera which acts as the exteroceptive sensor. As shown in the figure, occluded areas can be seen on the opposite side of the pile where the sensor vision is blocked. To overcome the occluded area, proprioceptive mapping is added to the purely exteroceptive mapping.



Figure 5.7: Initial Occluded Area Ground Map

5.2.2 Identification of Bucket Trajectory using Kinematic Analysis

Proprioception is achieved by tracking the bucket trajectory as it moves through the soil as illustrated in Fig. 5.8. The first step in reconstructing a map in an obstructed environment is to recognize a bucket trajectory. This was done using the stroke data measured using LVDT sensors attached to the arm, boom, and bucket links. The stroke data was converted to each joint angle, and these angles were converted to the x , and y coordinates through a kinematic analysis. Figure 5.9 illustrates the corresponding angles of each joint, and Table 5.3 shows the physical measurements of the excavator.



Figure 5.8: Occlusion Area in Front of Excavator

5.2.2.1 Conversion of Stroke to Bucket Position

Table 5.1: Physical Measurements of Excavator

<i>Measurement</i>	<i>Value</i>	<i>Measurement</i>	<i>Value</i>
<i>FB</i>	<i>0.175 m</i>	<i>FG</i>	<i>0.576 m</i>
<i>HC</i>	<i>0.549 m</i>	<i>CK</i>	<i>0.187 m</i>
<i>LN</i>	<i>0.450 m</i>	<i>NM</i>	<i>0.298 m</i>
<i>PQ</i>	<i>0.249 m</i>	<i>DQ</i>	<i>0.120 m</i>
<i>ND</i>	<i>0.111 m</i>	β_b	31°
α_b	45°	β_a	157.5°
α_a	34°	β_k, α_k	$15^\circ, 87^\circ$

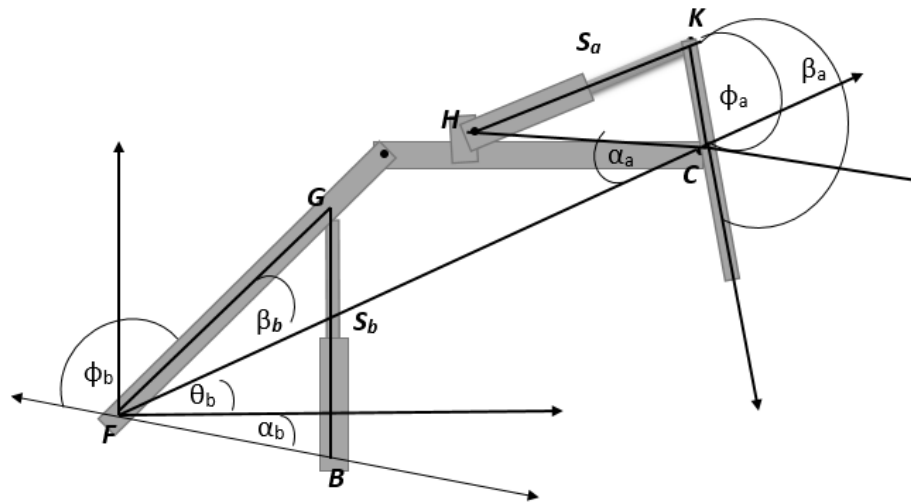


Figure 5.9: Boom, Arm, and Bucket Links and Their Corresponding Angles

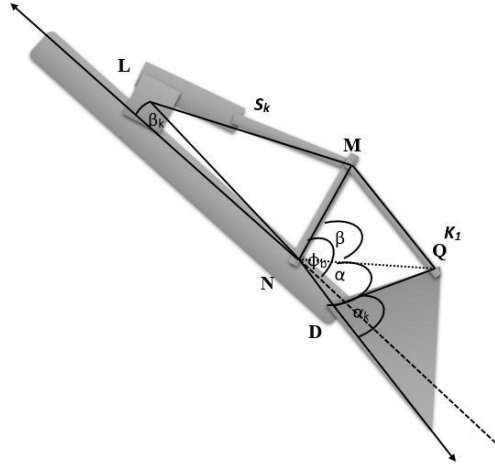


Figure 5.10: Bucket Actuator and Corresponding Four-Bar Mechanism

where θ_b , θ_a , and θ_k are the boom, arm, and bucket angles, respectively.

The boom angle was calculated as:

$$\Phi_b = \text{acos} \left(\frac{FB^2 + FG^2 - S_b^2}{2.FB.FB} \right) \quad (5-2)$$

$$\theta_b = \pi - \beta_b - \alpha_b - \Phi_b \quad (5-3)$$

The arm angle θ_a was calculated using the equations below:

$$\Phi_a = \text{acos} \left(\frac{S_a^2 - HC^2 - CK^2}{2.HC.CK} \right) \quad (5-4)$$

$$\theta_a = 2\pi - \beta_a - \alpha_a - \Phi_a \quad (5-5)$$

The bucket motion is driven by the four-bar mechanism NMQD (Fig. 5.10). The bucket angle θ_k can be calculated using the bucket stroke S_k in the equation below:

$$\Phi_k = \text{acos} \left(\frac{LN^2 + NM^2 - S_k^2}{2.LN.NM} \right) \quad (5-6)$$

$$MND = \pi - \beta_4 - \Phi_k \quad (5-7)$$

$$k_1 = \sqrt{NP^2 + ND^2 - 2.ND.NP.\cos(MND)} \quad (5-8)$$

$$\alpha = \text{acos} \left(\frac{ND^2 + k_1^2 - NP^2}{2.FB.k_1} \right) \quad (5-9)$$

$$\beta = a \cos \left(\frac{k_1^2 + DQ^2 - PQ^2}{2.DQ.k_1} \right) \quad (5-10)$$

$$\mu = \alpha + \beta \quad (5-11)$$

$$\theta_k = 3\pi - \mu - \alpha_k \quad (5-12)$$

After computing the angles for each joint, the next step is to generate x , and y coordinates of bucket trajectory using the angles. The coordinates were calculated using the cosine law.

$$BucketTrackX = L2 \times \cos\theta_b + L3 \times \cos(\theta_b + \theta_a) + L4 \times \cos(\theta_b + \theta_a + \theta_k) \quad (5-13)$$

$$BucketTrackY = L2 \times \sin\theta_b + L3 \times \sin(\theta_b + \theta_a) + L4 \times \sin(\theta_b + \theta_a + \theta_k) \quad (5-14)$$

where $BucketTrackX$, and $BucketTrackY$ are the x , and y coordinates of the bucket trajectory.

Figure 5.11 shows the bucket trajectory after all the computations above.

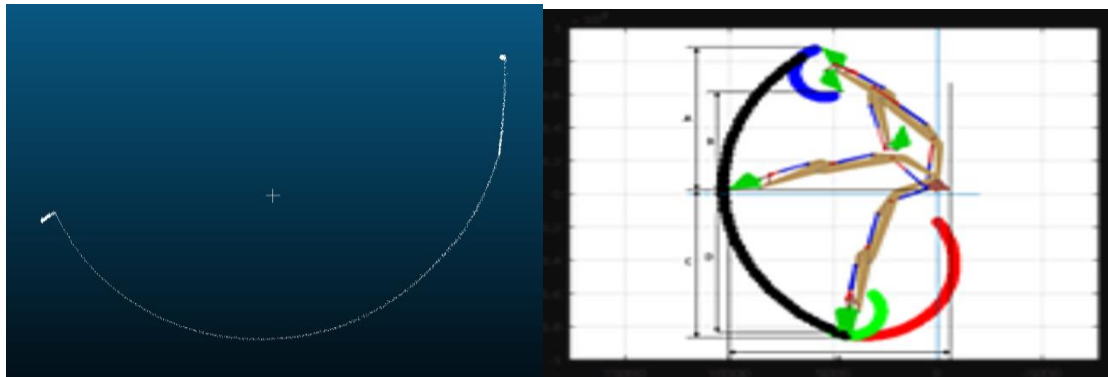


Figure 5.11: 2D Bucket Trajectory

5.2.2.2 Conversion of 2D Bucket Trajectory to 3D

The calculation of a 2D bucket trajectory was addressed in the previous section. This 2D trajectory helped identify a path of the bucket but it needs to be converted to 3D to reconstruct a map. For this conversion, we added the bucket width that can provide the 3D spatial info through merging with the 2D bucket trajectory. Figure 5.12 illustrates the conversion of the bucket trajectory in 3D space.

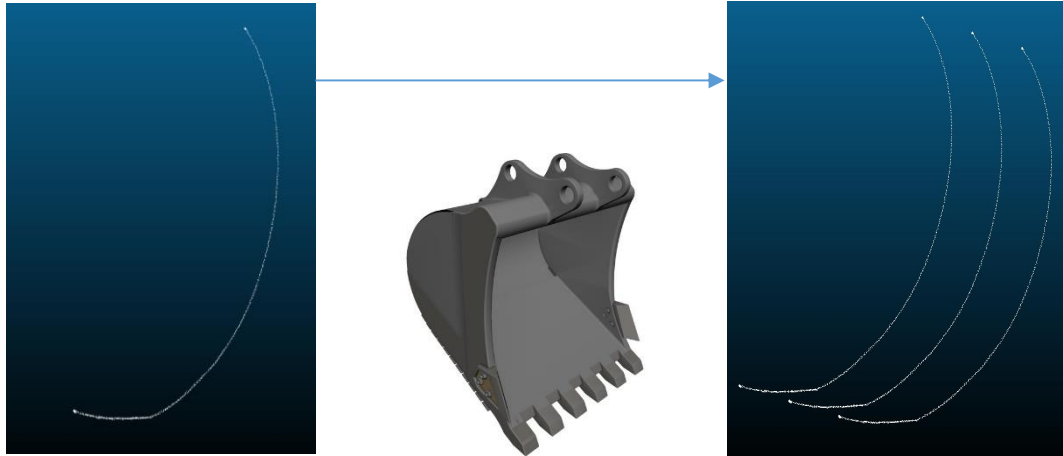


Figure 5.12: Conversion of The Bucket Trajectory in 3D Space

5.2.2.3 Meshing and Triangulation of Bucket Trajectory

Meshing is a representation of 3D surfaces as a series of discrete facets [47]. 3D meshes are geometric data structures most often composed of a bunch of connected triangles that explicitly describe a surface. Meshing creates a surface that is a closed-form representation of the scanned point cloud. The converted 3D trajectory of the bucket provides three lines. To cover vacant spaces between these lines, we applied the meshing technique that enables us to fill the vacant spaces, as shown in Fig. 5.13. Without meshing, the reconstructed map would lose many points.

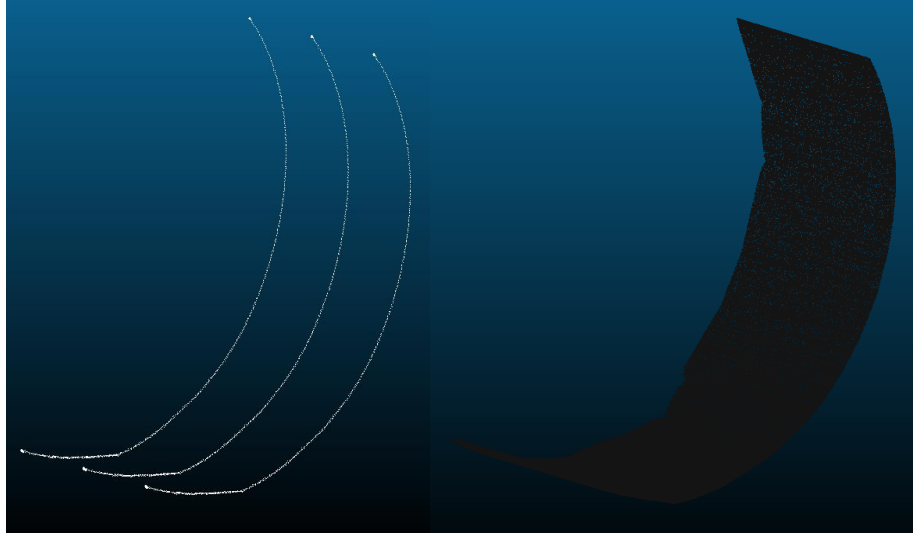


Figure 5.13: Conversion of Bucket Trajectory to Mesh

5.2.3 Reconstruction of a Map for Occlusion Areas

The next step after generating a 3D trajectory mesh was to reconstruct a map to overcome the occlusion area. For this task, the single frame of reference or a global coordinate was firstly determined. The global coordinate system was achieved using the transformation matrices mentioned in Section 5.1.2. The sensor coordinates were converted to the coordinates of the boom base that was set as the global origin at which because the bucket trajectory was calculated.

After achieving the unified coordinate system, the next step was to merge a 3D mesh of the bucket trajectory with the initial map. Once the bucket is passes through the occluded area, the erroneous area in the exteroceptive map is merged with the proprioceptive trajectory mesh. Both, the mesh from proprioceptive and the initial map from exteroceptive are point clouds and hence they can be merged directly. The state of the map after a proprioceptive update can be seen in Fig. 5. 14. Fig.5. 15 illustrates a finally reconstructed map. The reconstructed ground map after merging the bucket trajectory fills out the occluded area in the initial map. Thus, the reconstructed map covers the geometrical area.

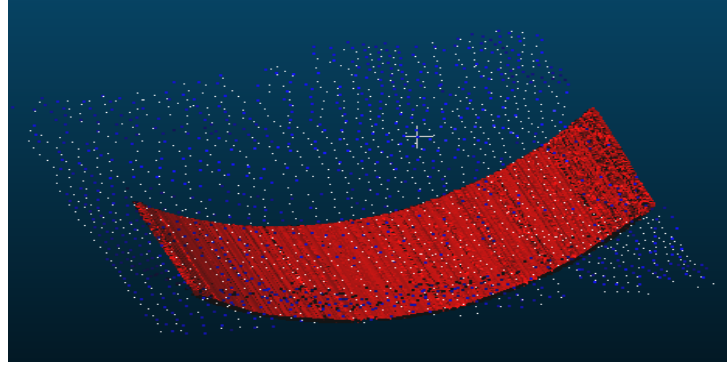


Figure 5.14: Map Update After Proprioceptive Merging

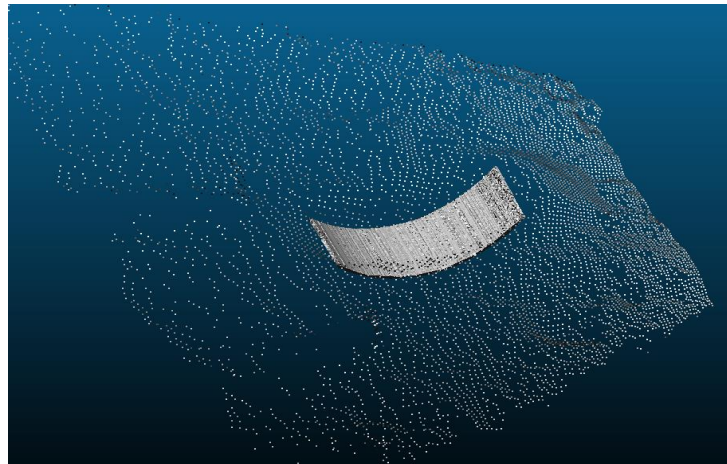


Figure 5.15: Reconstructed Map: Occlusion Area Problem

5.3 5D mapping

This study, 5D mapping, is referred to as a map that consists of a 3D ground map, intensity info based on LiDAR's beam reflectivity (1D), and force index (1D). The last 1D can be used to identify the properties of excavated materials and resistive ground force during digging.

The combination of all these entities generates a 5D map that can provide a broad spectrum of the excavated ground info. To support the classification of materials, we also applied the neural network (NN) using images taken during the excavation. [25] introduced the concept of 4D mapping, but this map lacks the info of the identified material type. So,

we extend this concept to a 5D map with the NN based image classification to identify material properties.

For this topic, we split the digging space into six segments for experimental tests. Each segment contains a different type of material. We built a 5D map and compared the properties of each material type.

5.3.1 Building 3D Geometrical Map

A 3D map includes the geometric information of the ground surface for excavation such as x, y , and z coordinate, shape, etc. To get the geometrical map, a stereo camera was used as it provides the dense point cloud and less vacant spaces between the channels. To cover the full area, the registration technique was introduced as it helped in building and accumulating the point clouds in a scene. Figure 5.16 shows the 3D geometrical map of the excavation ground containing three different materials (artificially supplied) and three natural ground material.



Figure 5.16: Excavation Ground Image

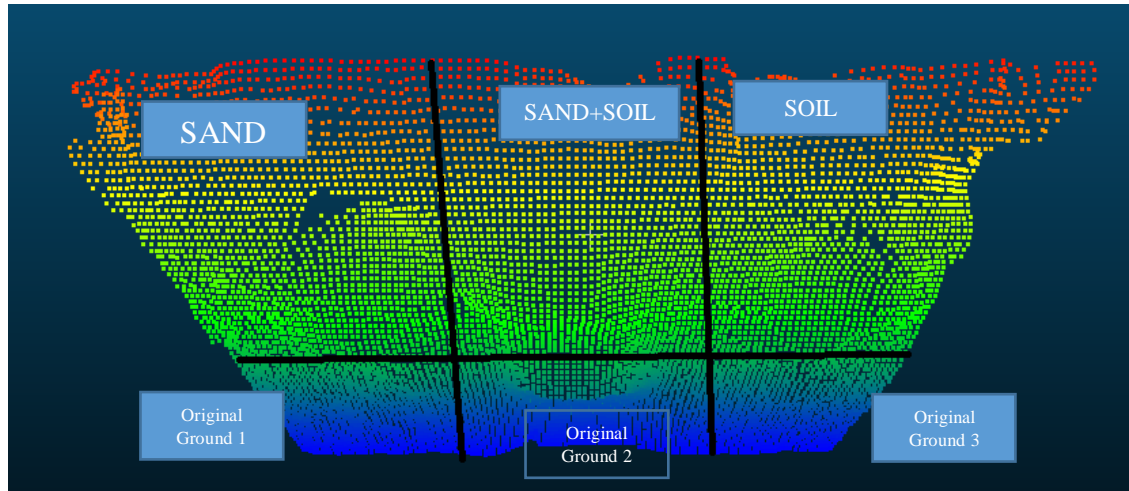


Figure 5.17: Excavation Ground Point Cloud

5.3.2 Materials Classification using LiDAR's Intensity

The stereo camera can provide the geometrical data for the 3D map but provide the beam reflectivity or intensity data that can be the additional crucial info of the excavation material.

To overcome this limitation, we fused a stereo camera with a LiDAR sensor that can provide intensity data, which can be used for numerous applications, such as feature detection, land cover classification, identifying wet areas, and vegetation classification [48]. For this project, we utilized its intensity value that can be considered as an index to identify the material type. Figure 5.18 shows the intensity map of the same scene from the previous Fig. 5.17.

Note that the intensity alone cannot classify the material as it changes with the material's outer surface. If two surfaces have identical outer colors, then their intensities would be similar. To strengthen the informative feature of our created map with the intensity and geometrical data, we introduced the force index for material classification.

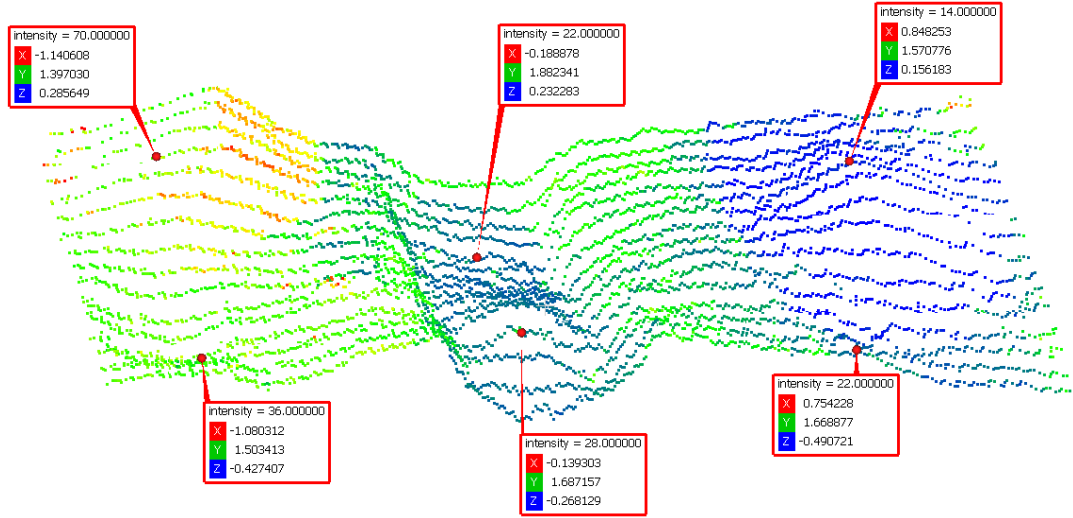


Figure 5.18: Intensity Index for Soil

5.3.3 Soil Type Classification Using Neural Network

To strengthen our 5D map, we added the image classification using neural networks. Images were taken during the whole excavation process after each dig. The MATLAB's deep learning toolbox provides the pre-trained image classification networks [49]. The Pretrained image classification networks were trained over a million images and can classify hundreds of objects. For our project, we classified the images of soil and sand, that were taken during the excavation process. We came up with the idea of a transfer learning concept. Transfer learning is commonly used in deep learning applications; we can take a pre-trained network and use it as a starting point to learn new tasks. The fine-tuning step is more comfortable and faster with a pre-trained network than training a network from scratch. The learned features can be transferred to a new task using a smaller number of images.

There are numerous pre-trained networks available, but we chose GoogleNet [50], as this network less error rate, provides better transfer learning, and it is relatively faster than other pre-trained networks [54]. Every neural network has several layers; the first element of the layers is the image input layer. For GoogleNet, the first layer requires the image of size 224-by-224-by-3.

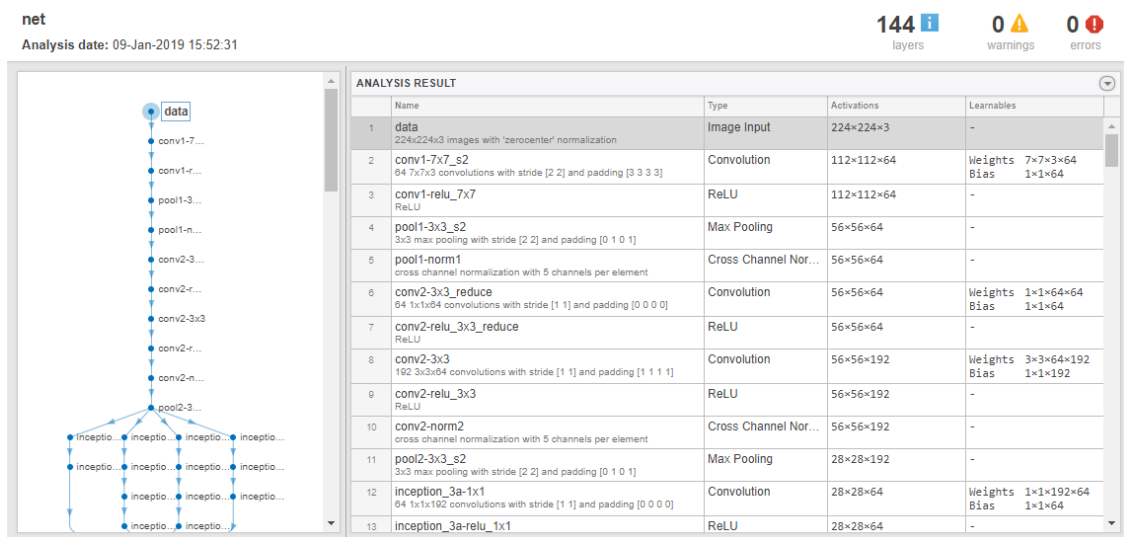


Figure 5.19: Network Architecture and Network Layers Information

GoogleNet is a 22 layers deep network when considering only layers with parameters. The total number of layers for the construction of the network is about 100. However, this figure depends on the infrastructure of the machine learning system. For our case, the total number of layers are 144. The weight of the network is set in a way that it trains on the “Places365” dataset.

The convolutional layers of the network extract image features using the last learnable layer and the final classification layer that are used to classify the input images. For this purpose, we replaced the final two layers of the pre-trained network, ‘loss3-classifier’, and ‘output’ with new layers adopted to the new data set. The classification layer was replaced with a new classification layer that specifies the output classes of the network.

The convolutional network has been trained over 100 images of sand and soil. These images were taken during the excavation process. The entire data set was divided into 70% of training, 20% of validation, and 10% of testing datasets. During the excavation progress, the images were given to our trained neural network for image classification. The output of the neural network is shown in Fig. 5.20.



Figure 5.20: Image Classification Using CNN

5.3.4 Construction of 5D Map

Construction of 5D mapping is the process of merging all the above information into a single map. The information covers the geo info of the excavated ground, intensity values, and force index. For this project, we divided the map into six segments with different types of materials. Each material has its corresponding 5D values with it.

Our contribution from building a 5D map is vital as it can help in identifying the types of soil, and underground structures, that are one of the major concerns in the urban excavation. We started with capturing the point cloud from the ZED stereo camera, which can provide the 3D geometrical ground info. The next implemented step was to introduce the reflectivity (intensity) concept using the LiDAR sensor and to apply the pressure/force index to provide the additional info of material type and resistive ground force in the form of a 5D map. Finally, the additional feature added to the 5D map is the image classification using neural network techniques.

Chapter 6. Results and Analysis

6.1 Introduction

In this chapter, the experimental results are discussed and analyzed. The chapter starts with the sensor selection for each algorithm. As we have discussed in Chapter 3, different sensors opted for this project, and each sensor was chosen based on the application of each theme. After the sensors selection, the chapter starts the analysis of results from each topic. Starting with the safety algorithm, the sensor location, obstacle detection, tracking, and safety indices for single and multiple objects are addressed. The second part of the chapter focuses on the volume estimation algorithm, in which ground volume, and bucket volume estimation techniques have been analyzed. The last phase of this chapter deals with the material type classification. This part presents the results for 5D mapping. Each component of the 5D map is discussed and analyzed.

6.2 Sensors Selection

Two vision sensors have been chosen for this project, VLP-16 LiDAR, and a ZED stereo vision camera. The VLP-16 LiDAR provides a long-range, along with the 360 degrees field-of-view. The 16 channels of the LiDAR provide a long-range, but less dense point cloud data. On the other hand, the ZED camera does not provide a long-range, or 360 degrees field-of-view, but the point cloud is dense and concentrated to a smaller region and short-range. We can analyze from the figure that LiDAR provides a good range, but there are some vacant spaces between the channels, while the stereo camera lack in range but has a dense point cloud.

For safety algorithm, LiDAR has been chosen as it covers the whole area around the excavator. For volume estimation and ground mapping, the stereo camera was chosen as it provides a dense point cloud on a specific region. For 5D mapping, both sensors were integrated, stereo camera provided the geometrical info, and LiDAR provided the intensity

data. Other proprioceptive sensors, such as pressure sensors, LVDT, and rotational encoder, have been used to support both safety and estimation of excavation progress.

6.3 Predicted Safety Algorithm Results

The first developed algorithm was the predicted safety algorithm. The algorithm was tested under different conditions, such as a single object and multiple objects. This section describes the location of the sensor for this task and results from single and multiple objects.

6.3.1 Sensor Location

The sensor location was set to a stationary position using the tripod, and the excavator was also in the stationary position. The origin of the global coordinate reference was chosen as the boom link of the excavator. Since the position of the sensor is fixed, the transformation was done before the experiments and the same transformation matrix was used for each experiment as the sensor is fixed to the specific location. Figure 6. 1 shows the location of the LiDAR sensor.



Figure 6.1: LiDAR Position

Note that the excavator does not have a rooftop where the sensor can be mounted. So, we decided to use a tripod for the LiDAR sensor.

6.3.2 Experimental Test Scenario

Experimental tests were carried under the situation where two static objects, and two moving objects were around the excavator to reproduce the scenarios for the collision that may occur at construction sites.

In Fig. 6.2, two static objects, *T1* and *T4*, and two moving objects, *T15* and *T16* are indicated. The objects carry their unique labels, as long as they are present inside the region interest (ROI). The label has two parts, “*T*” represents the track and the number represents the specific number of that object. Once the object leaves the ROI, its label is deleted and upon returning back to the ROI, a new label will be assigned. Therefore, some labels are missing from Fig. 6. 2, as those objects are not present in ROI anymore. Object detection, tracking, and safety evaluation were performed when the moving objects enter the ROI and continue to move closer to the excavator.

Note that some points in Fig. 6.2, and 6.3 are not clustered due to the processing issue. Specifically, those points are not to be formed into clusters yet at the given time frame and could be clustered after one or two frames. Experimental results are provided in the following section.

6.3.3 Obstacle Detection and Tracking

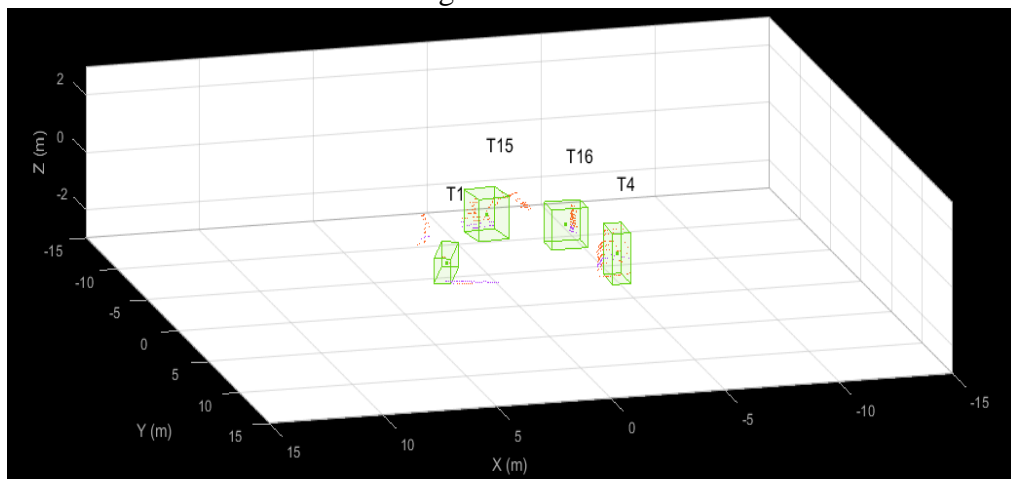


Figure 6.2: Multiple Object Detection

Figure 6.2 illustrates the raw point cloud data for detected objects obtained using the VLP-16 LiDAR sensor. Note that each object has its unique track ID ($T1$, $T4$, $T15$, and $T16$ in this case) that facilitates track management to associate data to each detected object and count the number of objects around the excavator.

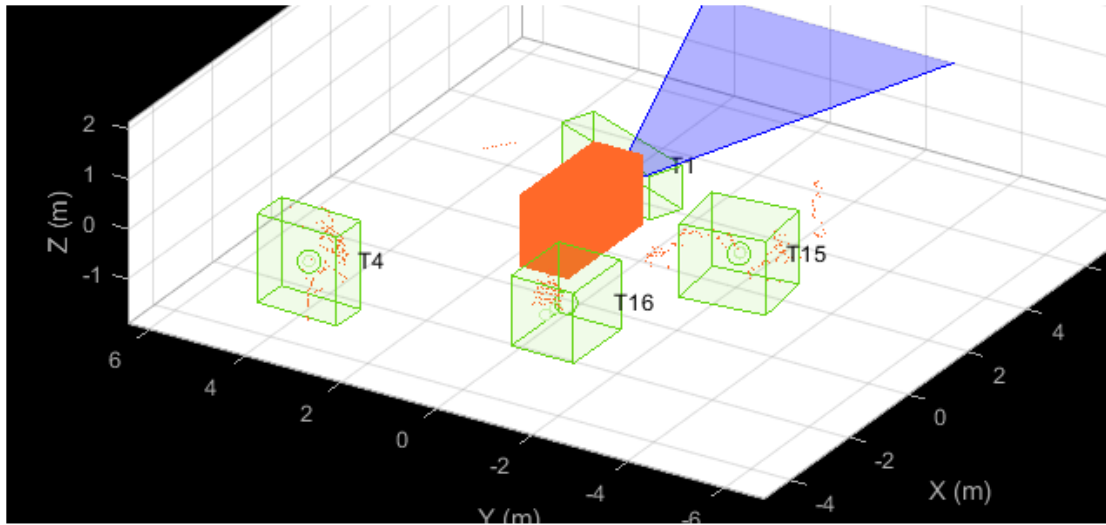


Figure 6.3: Operator's View

Figure 6.3 shows the operator's view. The box in the middle represents the excavator, and the fan-shaped area in the front of the excavator shows the visible sight of the operator, and bounding boxes present objects around the excavator. The track IDs in Fig. 6.2, 6.3, and 6.4 are identical, in order to maintain a unique label for each object.

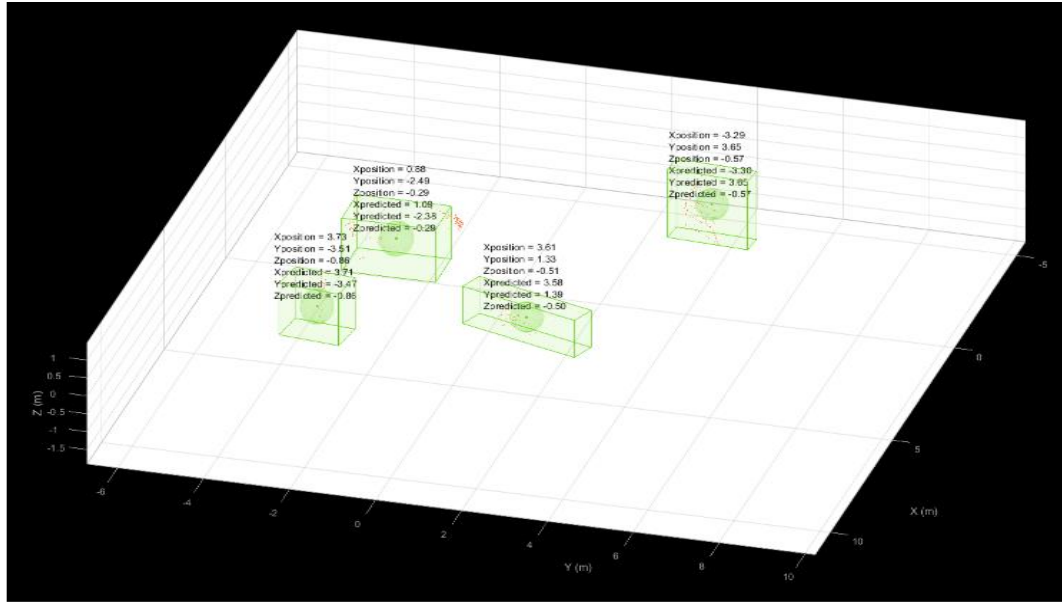


Figure 6.4: Tracking Details for Multiple Objects

Figure 6.4 shows the detailed tracking results by indicating the $x, y,$ and z coordinates of each object. These coordinates indicate both current and predicted positions. The predicted positions are 1 second ahead of the current positions. The sensor location act as a reference origin for the tracking details. These details are used for object tracking and safety evaluations.

6.3.4 Safety Evaluation Results

Figure 6.5 presents the working areas of the excavator, which include the maximum, and actual working area. Figure 6.5 also demonstrates the rotation of the excavator, heading orientation of the tracked moving objects, and their predicted states. Note that the maximum working area shows the working areas when the arm, boom, and bucket are fully extended while the inner circle illustrates the current actual working area that was calculated using the kinematic analysis based on the stroke data for the manipulator parts. The safety indices were calculated by using the actual working area.

Note that $T14$ and $T1$ are the static objects; hence their predicted and current positions are almost the same.

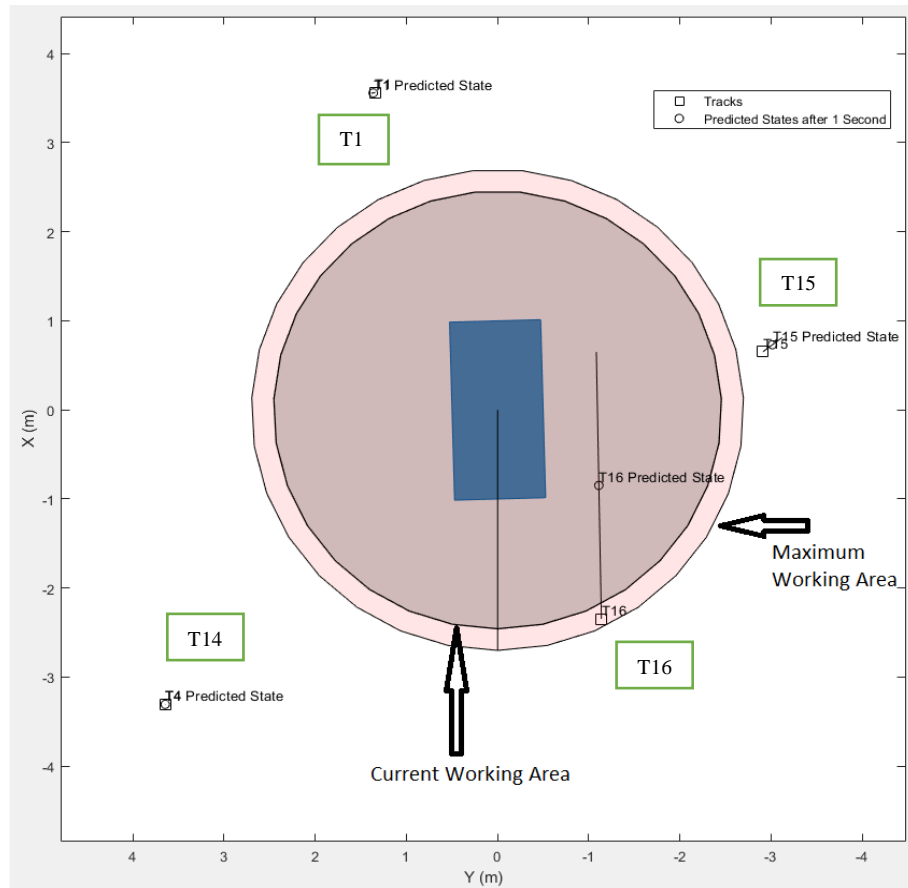


Figure 6.5: Excavator Working Area - Multiple Objects

Finally, Fig. 6.6 shows safety evaluation results with computed safety indices. The current state of $T15$ and $T16$ belong to the safe region. However, the predicted state of $T16$ indicates that it is entering the emergency region (i.e., a collision accident can occur while the worker is moving), a collision risk is expected. Thus, immediate breaking is required to avoid a collision.

In Fig. 6.6, only dynamic (moving) obstacles are considered for safety indices as all the static objects were away from the maximum working area, and therefore, they do not cause potential hazards.

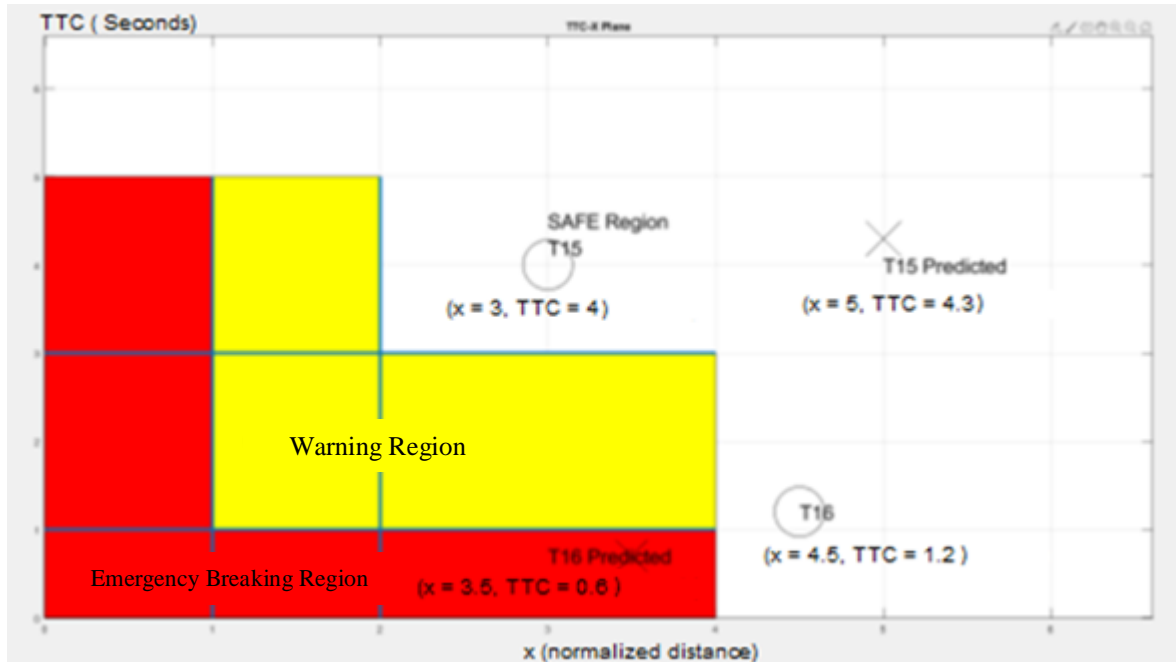


Figure 6.6: Safety Evaluation for Multiple Objects

In addition to the multiple objects, experiments were carried under the condition of a single object. Figure 6.7 shows the working area of the excavator along with the current and predicted (1 sec ahead) states of the object. From the figure, the object is in the close proximity of the excavator, and the predicted states show that the object would collide with the excavator and the chances of collision is high. To support this result, Fig. 6.8 was also analyzed. The current state of object *T2* in Fig. 6.8 is in the safe region, but the predicted states are indicating the entering of the object in the emergency region, and the risk of collision becomes high. Thus, the prediction is crucial as it indicates in advance about the potential accidental risk.

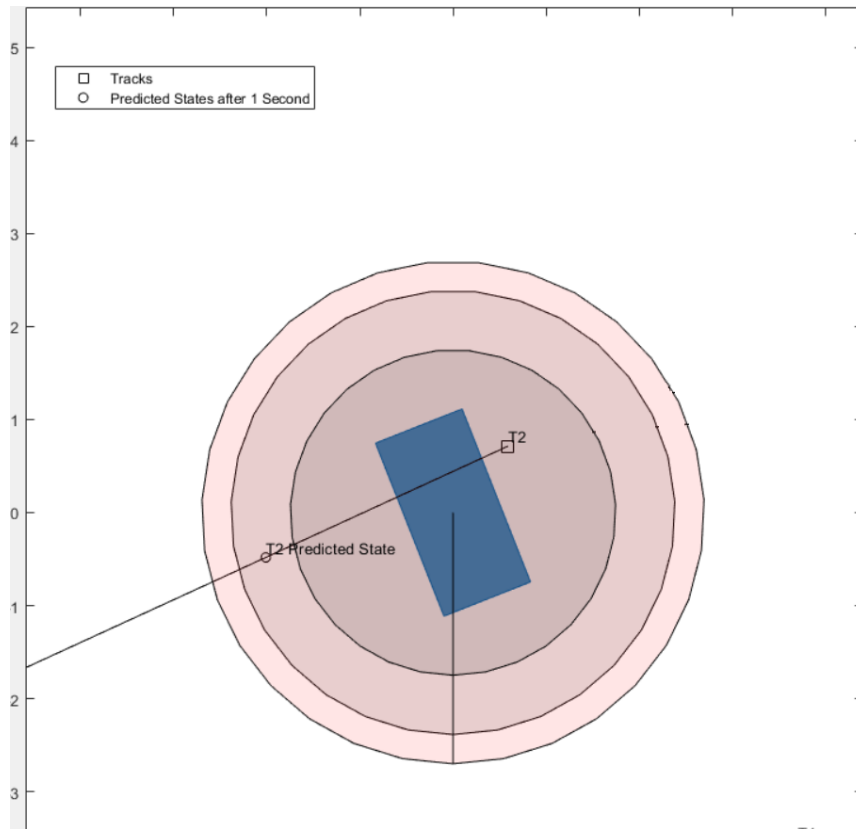


Figure 6.7: Working Area- Single Object

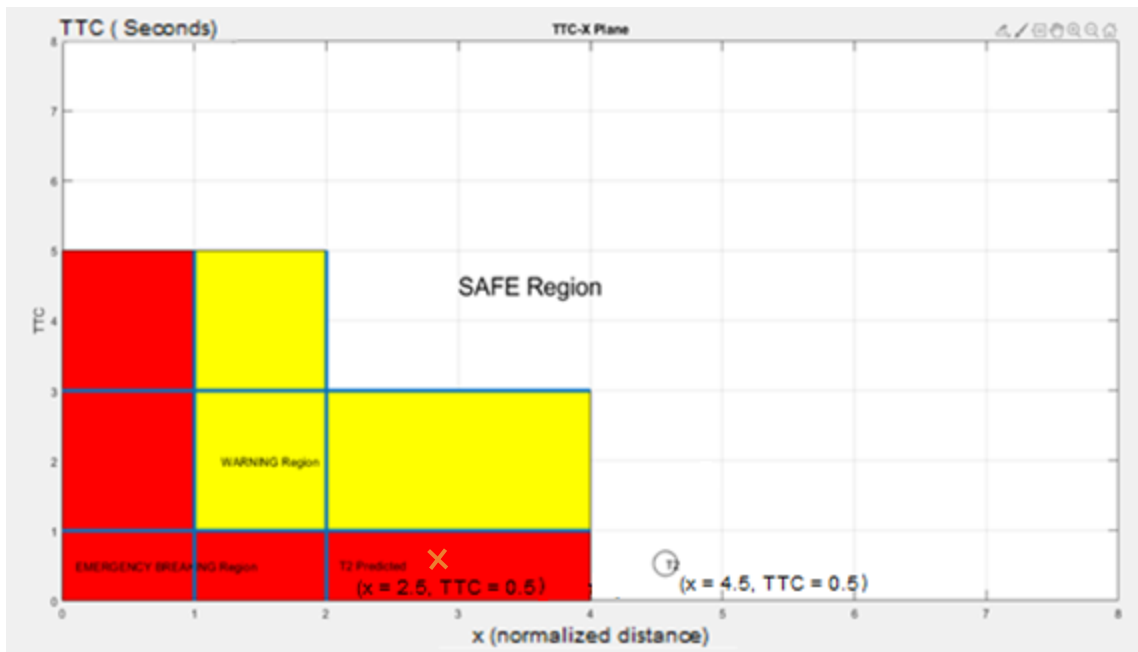


Figure 6.8: Safety Evaluation - Single Object

6.4 Volume Estimation Results and Analysis

This section covers the comparative results of the ground excavation volume estimation and bucket volume estimation algorithm. To calculate the volume, we added the contribution of each cell. This contribution is simply the volume of the elementary parallelepiped corresponding to the cellular footprint multiplied by the height difference.

$$V = \text{area} * \text{average grid height} \quad (6-1)$$

6.4.1 Bucket Contained Volume Estimation

The bucket contained volume is referred to as the soil volume that the bucket carried after each dig. Note that the bucket point cloud and image were captured after each dig during the excavation process. The captured bucket image is shown in Fig. 6.9, while the bucket point cloud in Fig. 6. 10.



Figure 6.9: Filled Bucket Image

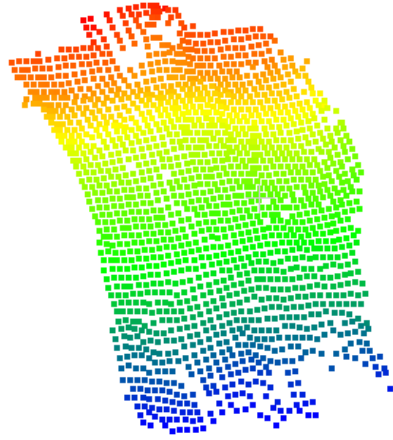


Figure 6.10: Filled Bucket Point Cloud

The captured point cloud was then registered and merged with the bucket CAD model. Figure 6. 11 shows the registration and merging of filled bucket point cloud with the bucket CAD model along with their images for two different cases.

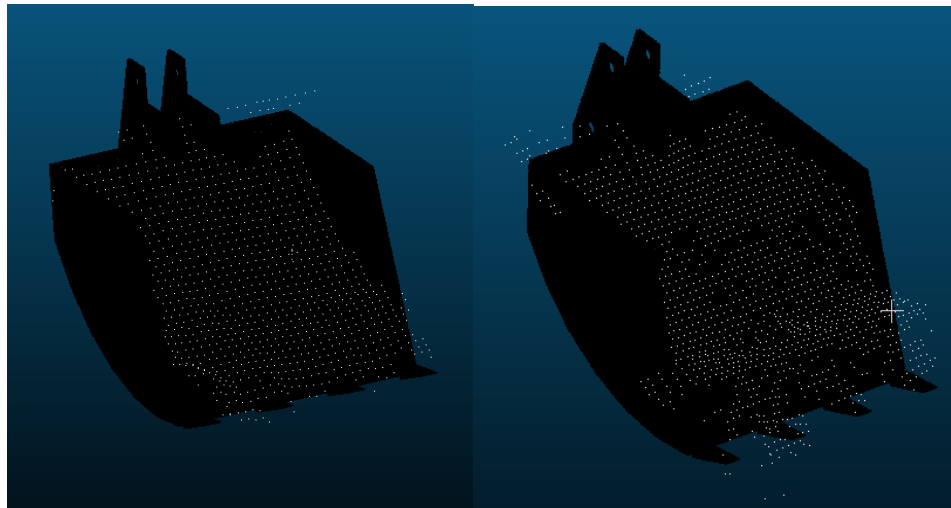


Figure 6.11: Filled Bucket Point Cloud and Bucket CAD Model Merged

To analyze the results, two different scenarios are presented in the graphical form. The first scenario represents a case when each dig carries almost the same amount of volume, while the second scenario have different volume level in each dig. Figure 6. 12 shows the graph for the first scenario, whereas Fig. 6.13 illustrates the second scenario. The digging occurred five times in both scenarios. Note that the volume is continuously

increasing because the graph shows the accumulated volume. Accumulated volume is the cumulative volume after each dig.

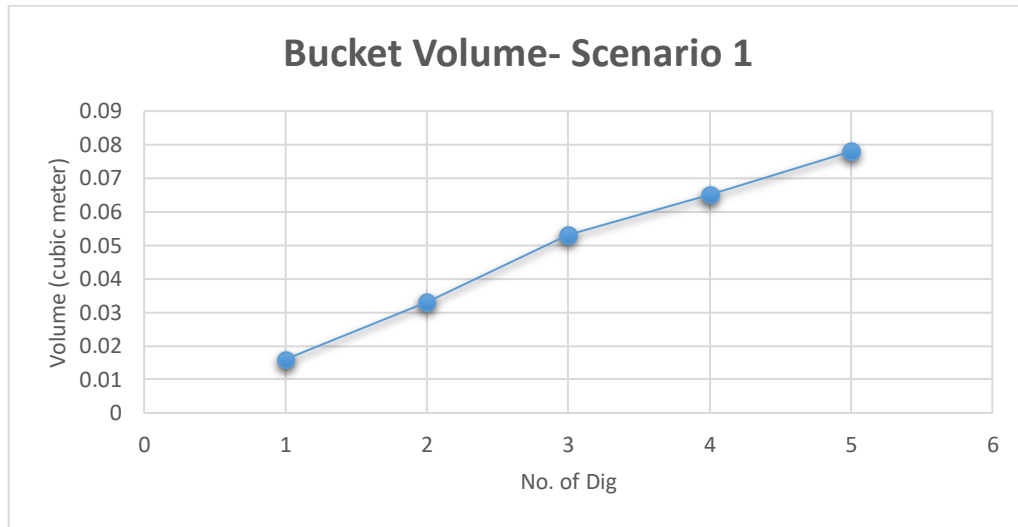


Figure 6.12: Scenario 1 - Accumulated Bucket Volume

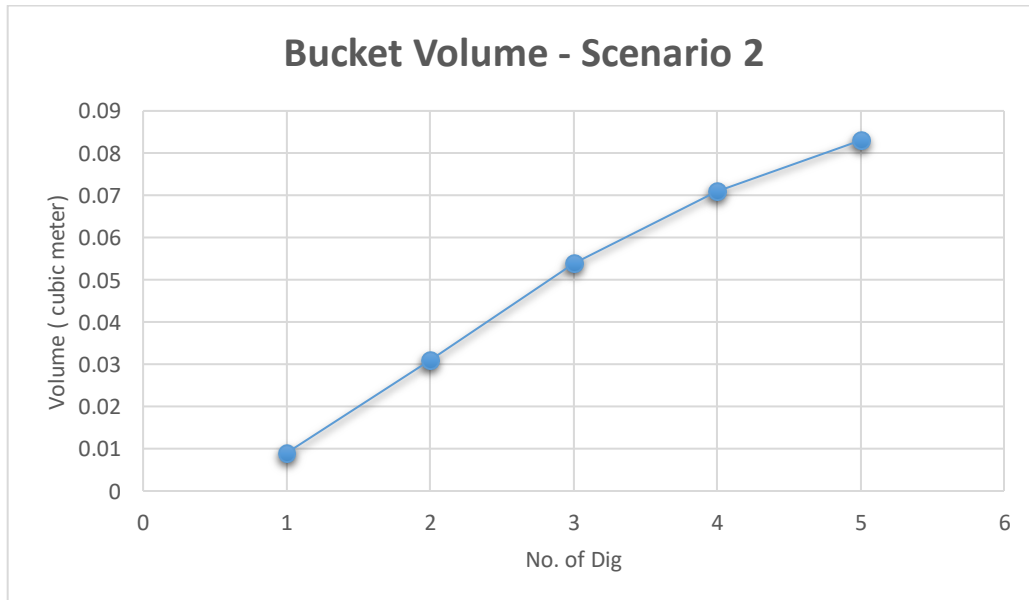


Figure 6.13: Scenario 2 - Accumulated Bucket Volume

For the first scenario, we tried to have a uniform volume for each dig, and hence the first graph shows the relationship closer to the linear model. For the second scenario, each dig contains a different amount of soil, and hence the relationship in the second graph is increasing without following a linear line.

The graphs show a reasonable volume, i.e., increasing accumulated volume after each dig. The results have been compared with the ground excavation volume estimation and actual volume to check the accuracy of estimation. A comparison is provided in the 6.4.3

6.4.2 Ground Excavation Volume estimation

The ground excavation volume estimation is the process of gathering point cloud from the ground surface after each dig and estimating the dug volume. After each dig, some volume of the ground can be removed, and comparing it with the initial point cloud (initial ground volume) can provide the volume change. Figure 6.14 and 6.15 show point clouds of the ground before and after the excavation, respectively.



Figure 6.14: Ground Surface Point Cloud Before Excavation

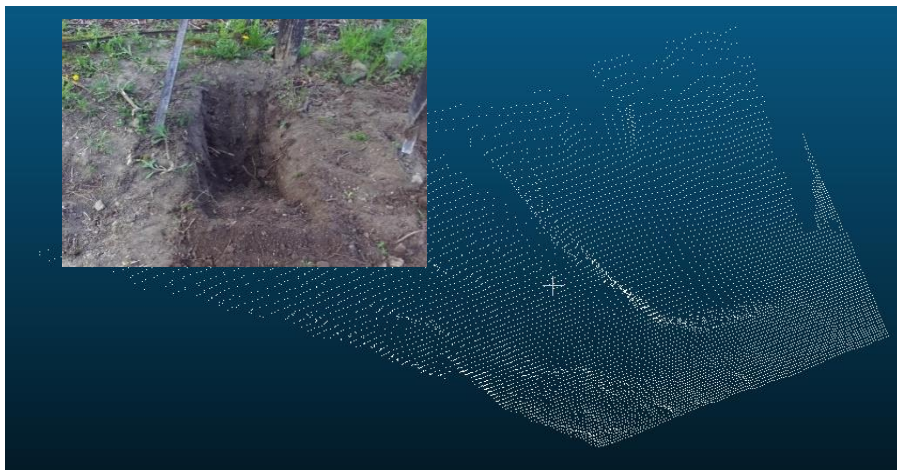


Figure 6.15: Ground Surface Point Cloud After Digging

For the ground excavation volume estimation, the same two scenarios used in the bucket volume estimation were chosen as the bucket volume estimation. The first scenario has the same volume of soil in each dig, while the second scenario has different volumes in each dig. Below are the two graphs that show the ground excavation volume estimation of each dig for the two scenarios.

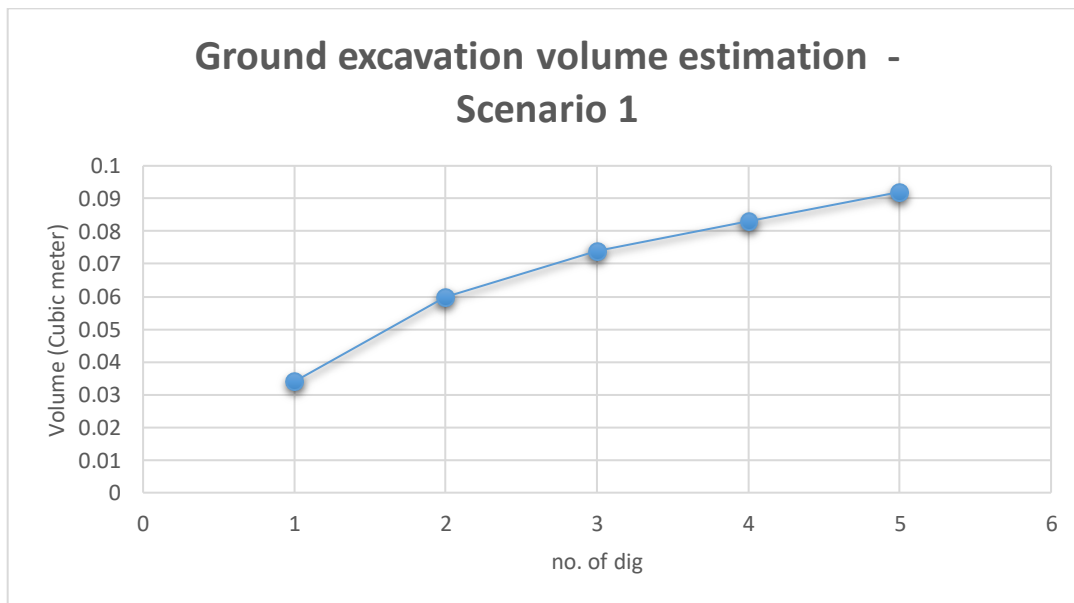


Figure 6.16: Scenario 1 - Ground Volume

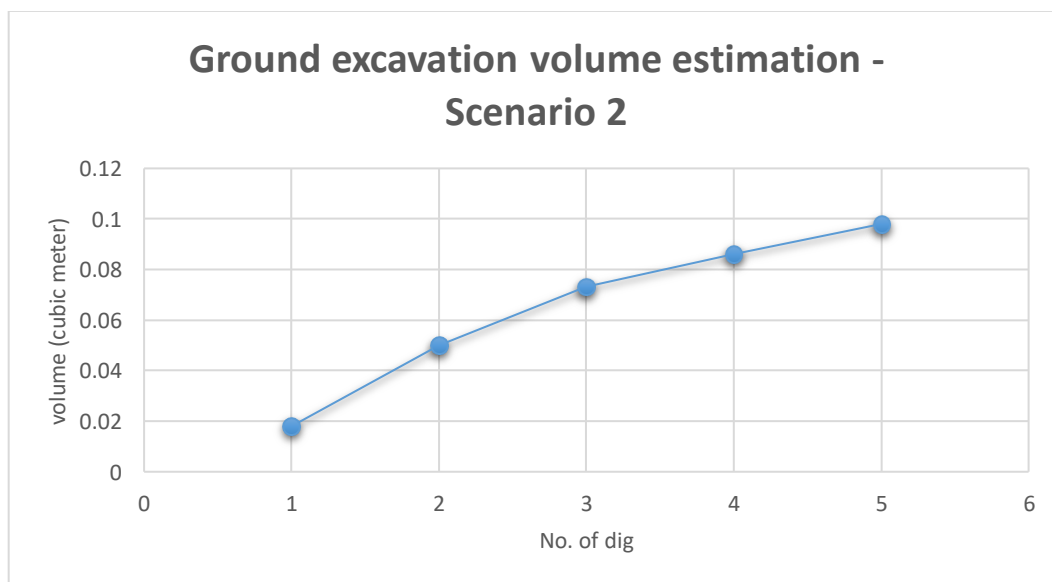


Figure 6.17: Scenario 2 - Ground Volume

6.4.3 Relationship between ground and bucket volume

Figure 6. 18 shows the comparison of scenario one and Fig. 6.19 for scenario 2.

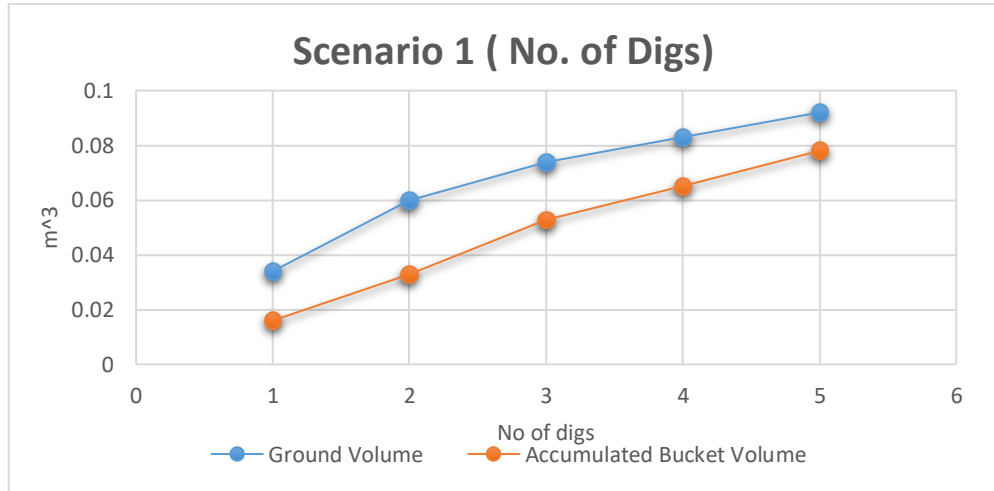


Figure 6.18: Scenario 1 - Bucket and Ground Volume Comparison

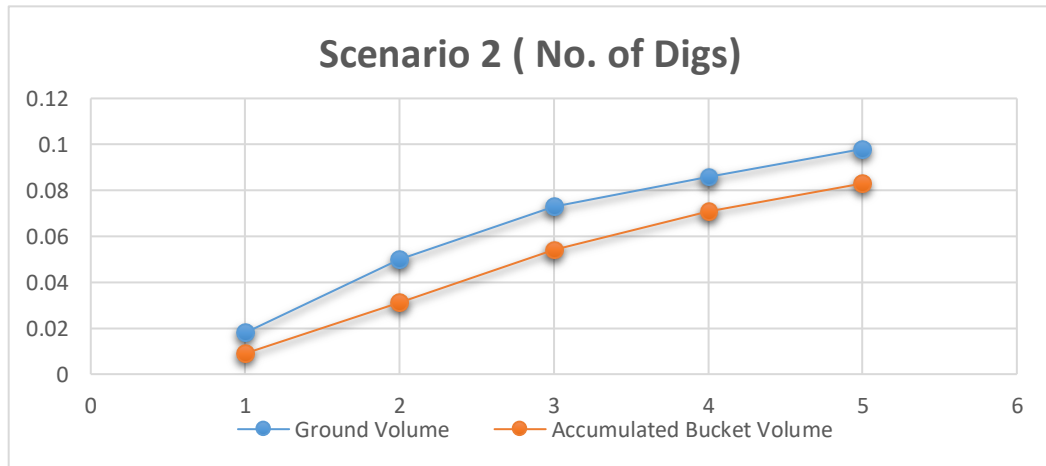


Figure 6.19: Scenario 2 - Bucket and Ground Volume Comparison

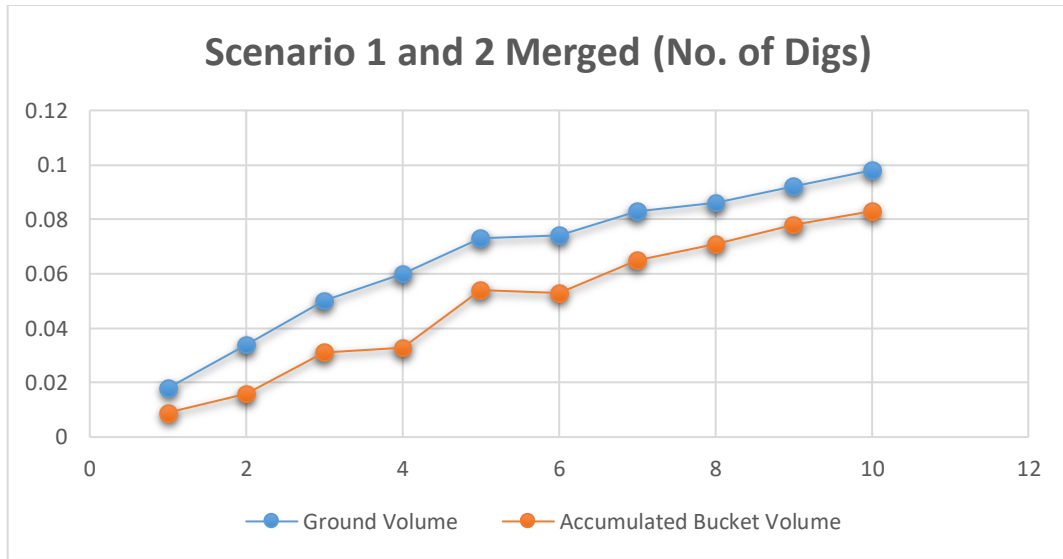


Figure 6.20: Scenario 1, and 2 Merged - Bucket and Ground Volume Comparison

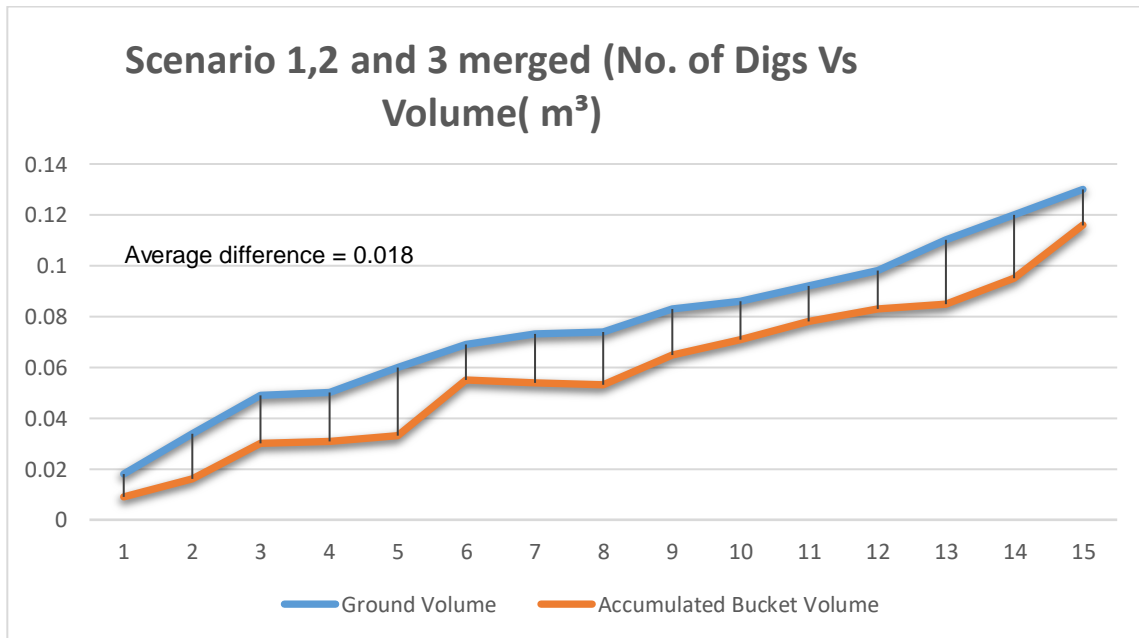


Figure 6.21: Scenario 1,2, and 3 Merged - Volume Estimation Comparison

By analyzing the two graphs, we can see that bucket volume and ground volume follow the same pattern with an offset separating each other. This is because the ground and bucket volume estimation are based on the same two digging scenarios. Thus, the actual dug volume must be almost identical or similar between these two, although there should be somewhat different values due to applying the different methods. The bucket

point cloud was taken from the stereo camera that provides a dense point cloud, but the sharp edges are hard to get. The registration technique can match the landmarks in two point clouds. Landmarks are the sampled points from the 3D surface. The number of landmarks is insufficient in the case of matching bucket's point clouds with a CAD model. In contrast, landmarks in the ground surface point clouds are sufficient. So, the registration technique provides better results when there are sufficient landmarks available, as in the case of the ground excavation volume estimation. We can validate our assumption by introducing the 3rd scenario in Fig. 6.21. The 3rd scenario also has five digs with different amounts of volume. The introduction of the 3rd scenario adds more points in our volume graphs for comparison. This can be useful in validating our assumptions. The 3rd is merged along with other scenarios.

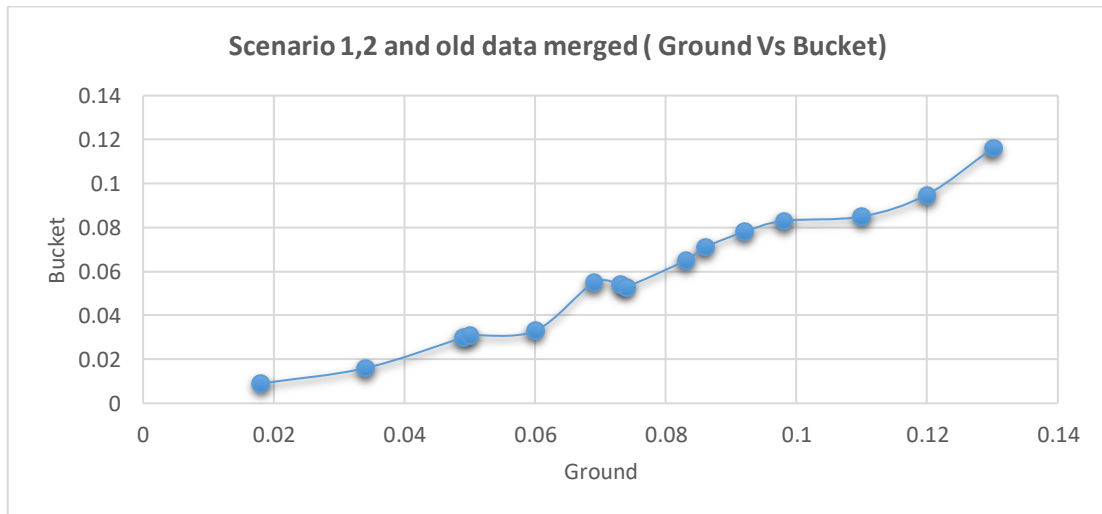


Figure 6.22: Ground and Bucket Volume Relationship

The graph in Fig. 6.22 shows the relationship between the ground volume and bucket volume. From the graph, we can see the pattern closely follows the linear relationship except a few points. Table 6.1 shows the difference between ground and bucket volume. The bucket volume estimation is important because the bucket can be always monitored and the bucket volume can be estimated without any occlusion issue.

Table 6.1: Estimated Volume Comparison

No. of Digs	Accumulated Ground Volume (m^3)	Accumulated Bucket Volume (m^3)	Difference (m^3)
1	0.018	0.009	0.009
2	0.034	0.016	0.018
3	0.049	0.03	0.019
4	0.05	0.031	0.019
5	0.06	0.033	0.027
6	0.069	0.055	0.014
7	0.073	0.054	0.019
8	0.074	0.053	0.021
9	0.083	0.065	0.018
10	0.086	0.071	0.015
11	0.092	0.078	0.014
12	0.098	0.083	0.015
13	0.11	0.085	0.025
14	0.12	0.095	0.025
15	0.13	0.116	0.014

For ground excavation volume estimation, the rate of excavation progress is given as:

- $Rate = \text{cut ground volume} / \text{initial ground volume}$
- $\text{cut ground volume} = \text{initial point cloud} - \text{remaining point cloud}$

For bucket volume estimation, the rate of excavation progress is given as:

- find the bucket volume (m^3)
- Using the linear relationship in Fig. 6.22 and average offset (between (cut) ground volume and bucket volume), we can estimate the (cut) ground volume (m^3)
- $Rate (\%) = (\text{cut}) \text{ ground volume} / \text{initial ground volume}$
- $\text{Bucket Volume-based Ground Volume} = \text{internal bucket volume} + \text{average offset}$ (Fig. 6.23)

Table 6.2 shows the excavation progress rate for ground excavation volume estimation and bucket volume estimation.

Table 6.2: Excavation Progress Rate

No. of Digs	Ground Volume (rate) - A	Internal Bucket Volume - B	Bucket Volume-based Ground Volume - C	Difference (A-C)
1	13%	6%	14%	1%
2	24%	11%	19%	5%
3	35%	21%	29%	6%
4	36%	22%	29%	7%
5	43%	24%	31%	12%
6	49%	39%	46%	3%

7	52%	39%	46%	6%
8	53%	38%	45%	8%
9	59%	46%	54%	5%
10	61%	51%	58%	3%
11	66%	56%	63%	3%
12	70%	59%	66%	4%
13	79%	61%	68%	11%
14	86%	68%	75%	11%
15	93%	83%	90%	3%

6.5 Occlusion Area Problem Results and Analysis

The occlusion area problems occur when there is a block in the vision of the sensor. Figure 6.23 shows a typical example of an occluded area (blue region).

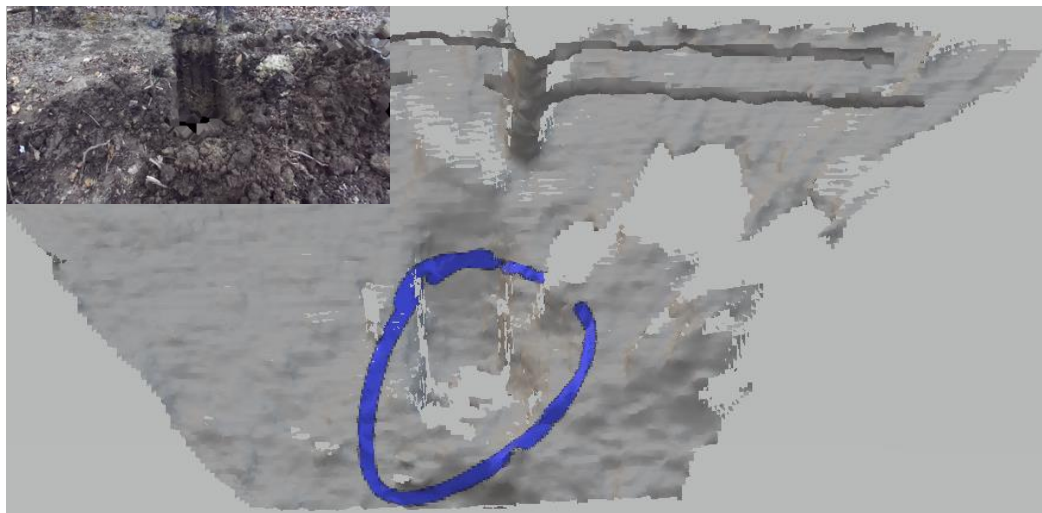


Figure 6.23: Occlusion Area Problem

6.5.1 Bucket Trajectory formation

In Fig. 6.24, the green box presents initial point clouds of the occluded region in the considered test scenario.



Figure 6.24: Occluded Area Point Cloud

The total number of gathered numbers for this specific case is 1384 over 14 seconds, with approximately 100 measurements per second. The angle data is then converted to x , and y coordinates using the kinematic analysis. The point cloud of the bucket trajectory was generated using the x , and y coordinates. The bucket trajectory of this specific case is shown in Fig. 6.25. This bucket trajectory is then converted to the 3D trajectory using the bucket width, which is 15 inches (7.5 inches each side)

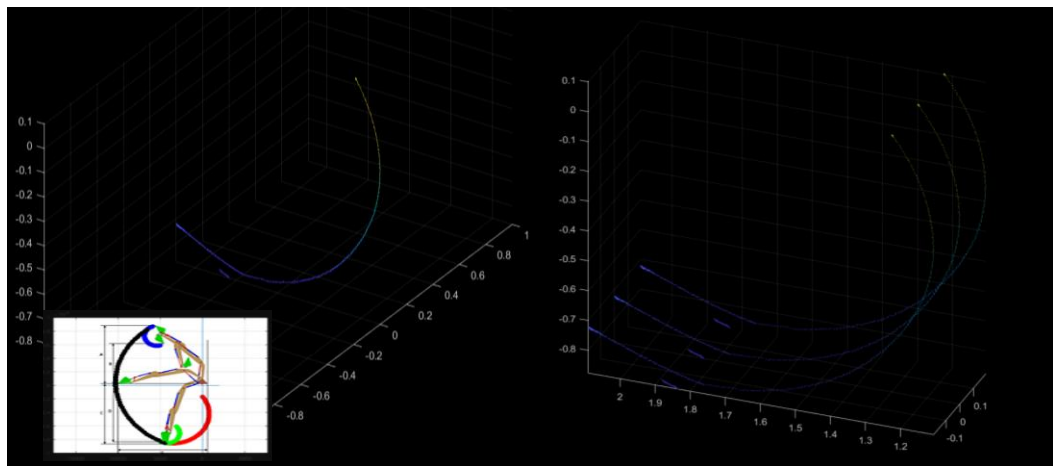


Figure 6.25: Bucket Trajectory

The next step was to fill out the vacant spaces between the 3D trajectory. This was done using the triangulation meshing, as shown in Fig. 6. 26

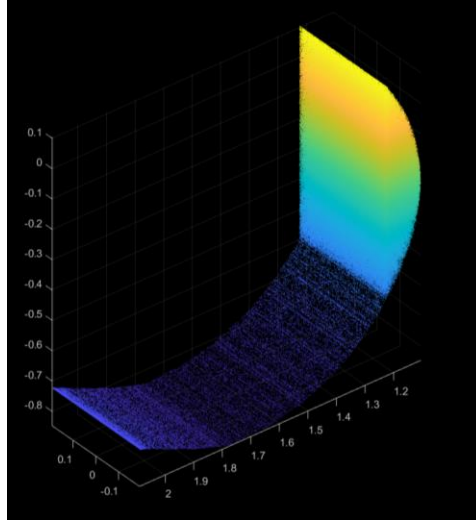


Figure 6.26: Bucket Trajectory Meshing

Meshing is the last step for the bucket trajectory; the next step was to merge the bucket trajectory with the ground point cloud.

6.5.2 Reconstructed map for occluded area

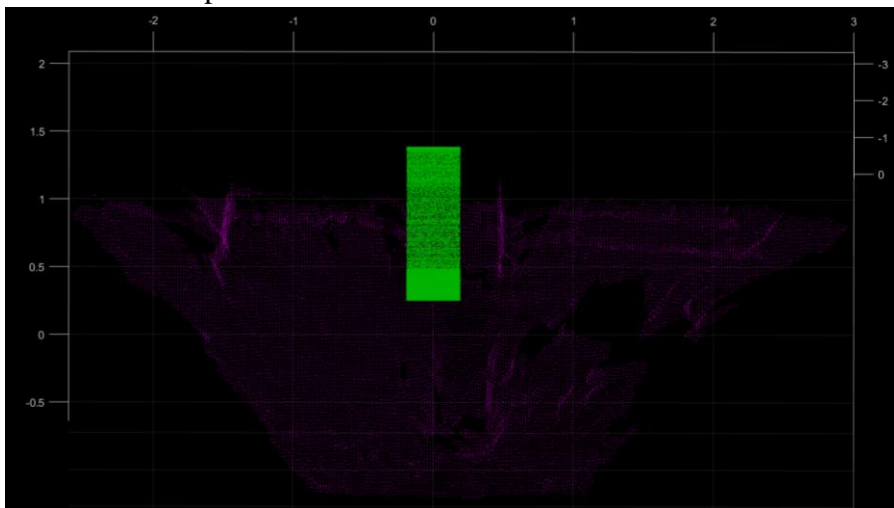


Figure 6.27: Merging of Occluded Area Point Cloud and Bucket Trajectory

Figure 6. 27 shows the merging of bucket trajectory with the ground point cloud. Note that the coordinate reference for both point clouds are different, so the transformation was required. The transformation was computed once before starting the experiment and applied to all the experiments.

After transforming the bucket trajectory, the final reconstructed map was obtained by merging the transformed bucket point cloud and ground point cloud. Note that the

bucket trajectory also contains points that do not belong to the ground. So we deleted these points and the final constructed map is given as follows.

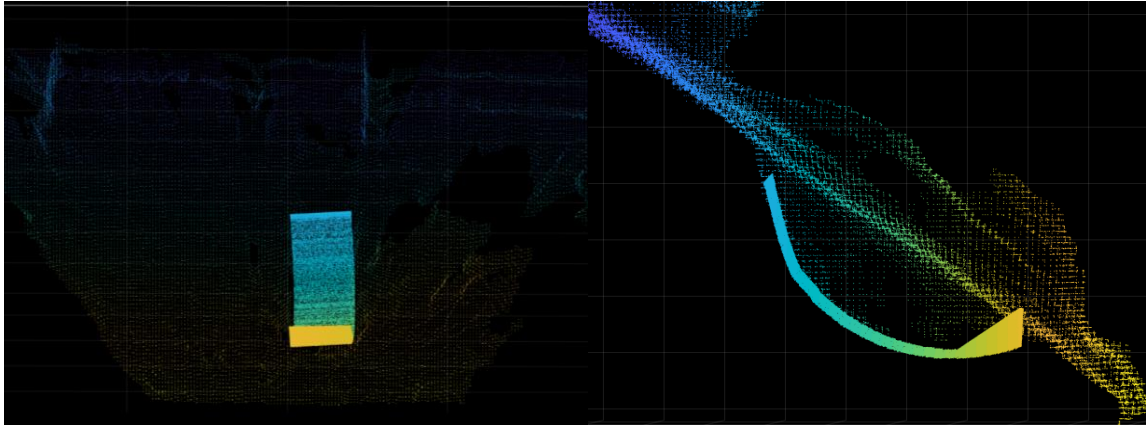


Figure 6.28: Reconstructed Map for Occluded Area

6.5.3 Verification of reconstructed map for Occluded Area.

To verify the accuracy of the reconstructed map including the occluded area, it was compared to the 3D map using the point cloud that was obtained from the stereo vision camera installed in the opposite direction of the occluded region.

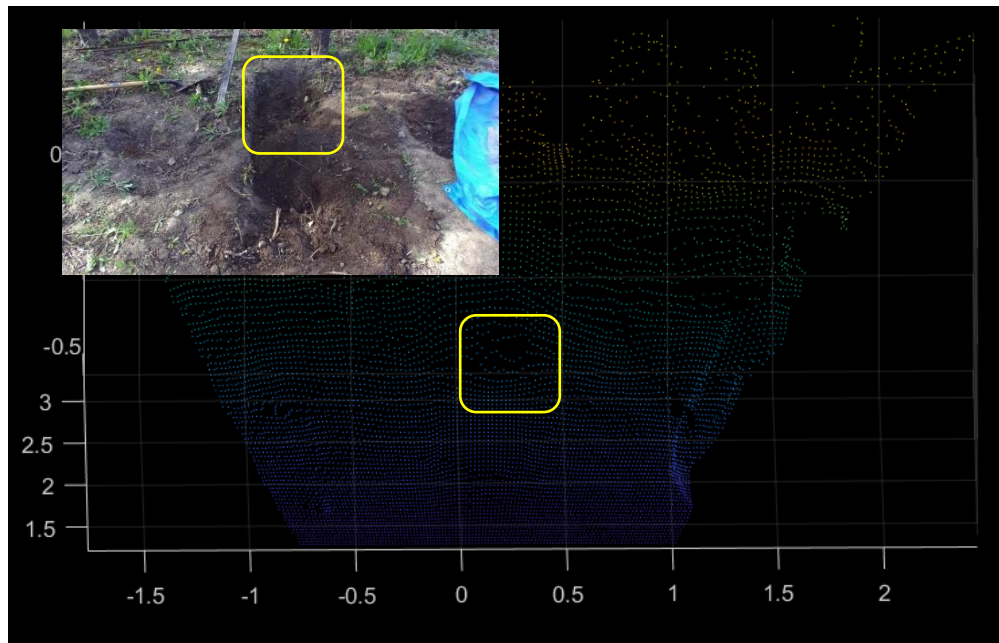


Figure 6.29: Occluded Area - Front Side

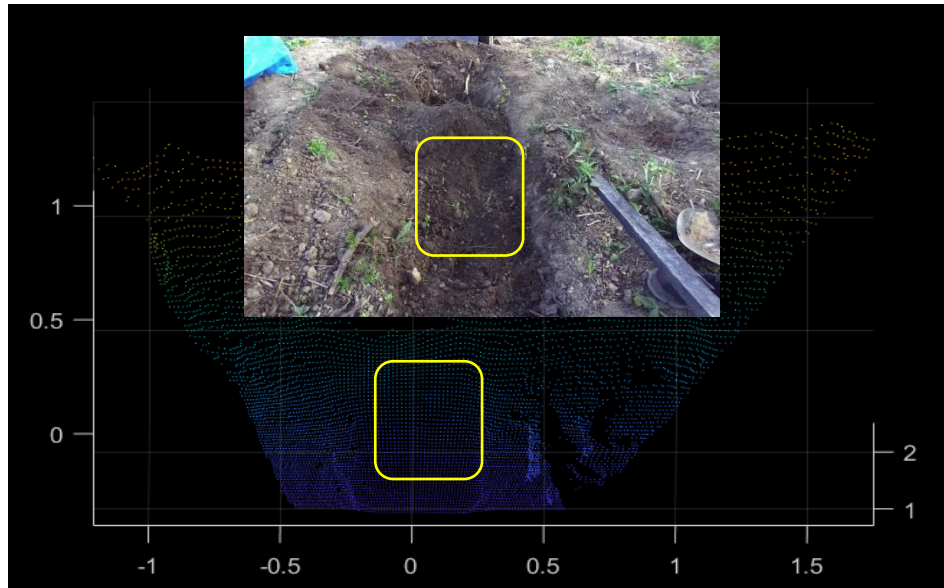


Figure 6.30: Occluded Area - Opposite Side

From the above two figures, we can observe that the occluded area in the front point cloud (Fig. 6.29) can be seen from the opposite side (Fig. 6.30) of the same point cloud. Note that these two point clouds were taken separately. Below are the figures of reconstructed maps and their corresponding point clouds from the opposite direction for verification purposes.

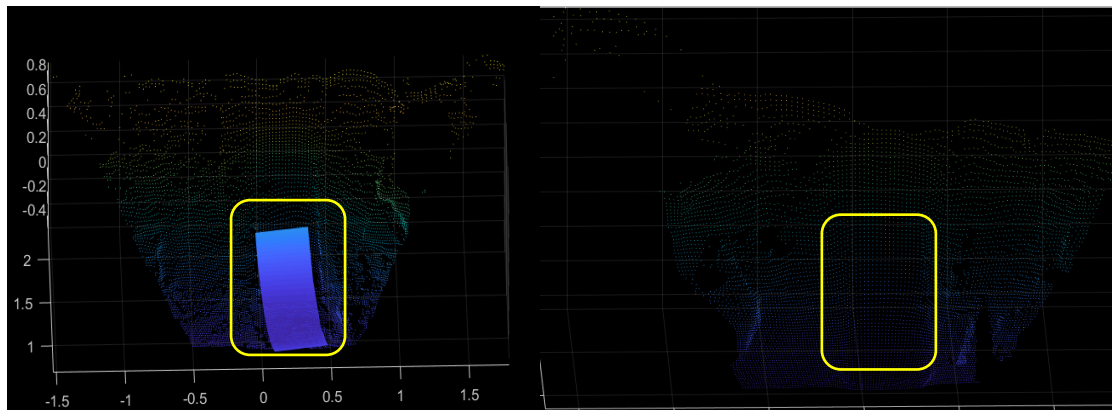


Figure 6.31: Occlusion Area Verification (Left: Front and Right: Opposite)

6.6 Material Properties – 5D Map

6.6.1 3D ground map and LiDAR's intensity

5D mapping is the construction of a map that consists of a 3D ground map, intensity info based on LiDAR's beam reflectivity, and force index.

For 5D map construction, both stereo camera and LiDAR were used. The three-dimensional geometrical position (x , y , and z coordinates) was measured by a stereo camera while intensity (reflectivity) data was collected by a LiDAR. Figure 6.32 shows a 3D map that shows the x , y , z coordinates of the targeted ground for excavation. The corresponding intensity value by a LiDAR can be seen in Fig. 6.33.

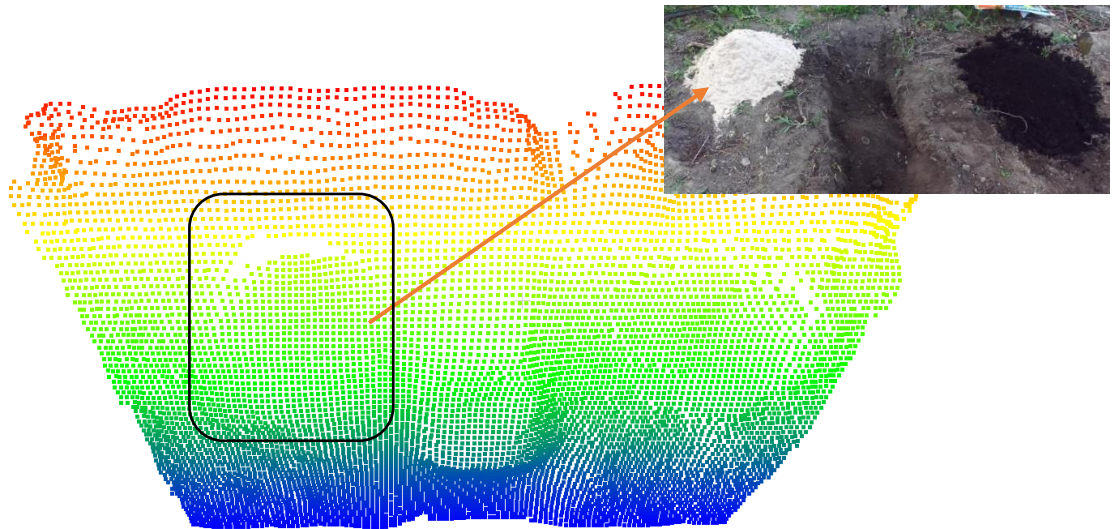


Figure 6.32: 3D Geometrical Info for Soil

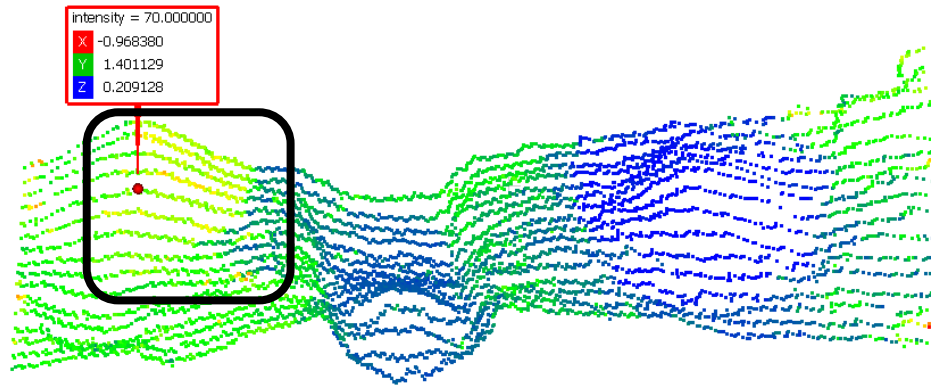


Figure 6.33: Soil Intensity Value for 5D Map

From the above figure, we can see that the two point clouds provide the coordinate info and intensity of the ground materials. To construct a 5D map, the second step is to merge the two point clouds obtained from the different types of sensors (stereo camera and Lidar). The merged point cloud was achieved by transforming one of the point clouds and merging with the other point cloud.

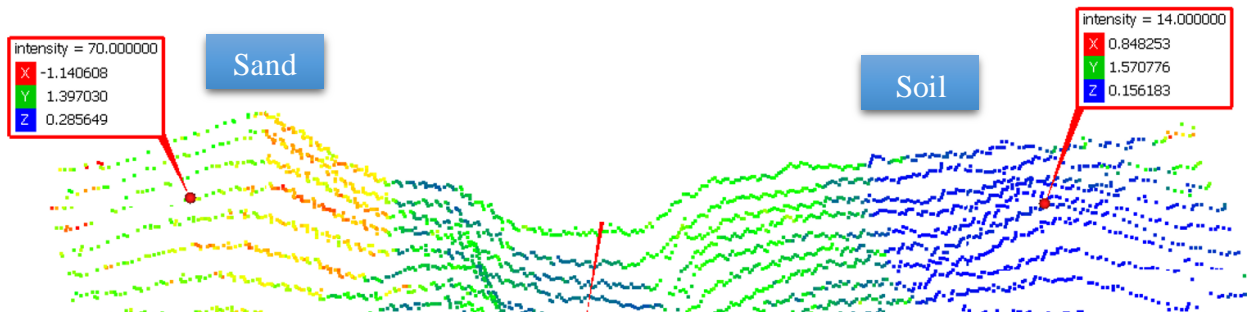


Figure 6.34: Position and Intensity Values for Sand and Soil

In figure 6. 35, we can observe that there is a significant difference in intensity between sand (left)-and soil (right). So, the intensity information could be used as an index to identify the type of materials but the intensity value is surface dependent. Specifically, if the colors of two materials are similar, their intensity values could be similar. However, the material info itself is not sufficient for sensing and control for autonomous excavation that is affected by the complex soil properties and dynamics such as ground resistive force.

So, we introduced the force as an additional index for the 5D mapping to represent the materials as follows.

6.6.2 Force Index

For 5D mapping, the head-side force and net force (see Eq. 3-2) of the bucket cylinder were considered as the force index. This is because the head-side force is generated by the bucket cylinder's extension during the excavation cycle (consisting of penetration, drag and rotate or curl) and the net force (=head side force-rod side force) of the bucket cylinder is used to be against the ground resistive forces. For experimental validation of the force index, the head-side and net forces were measured for the same target ground that has 6 segments. (Fig. 5.17). The first segment was the sand, the second was the mixture of sand and soil, third as soil, and the rest of the three were natural ground. Segment 1-3 were artificially made by putting materials on the ground, while segment 4-6 were the original ground surface.

To identify a digging point of the bucket on the ground surface during the excavation cycle, the bucket trajectory with respect to time was identified using the LVDT sensors and kinematic analysis.

Figure 6.35 and 36 show the bucket tip's trajectories with time of sand (Segment 1) and soil (Segment 3) as an example among 6 segments. The lowest point in each trajectory presents the digging (contact) point of the bucket during the excavation cycle. s

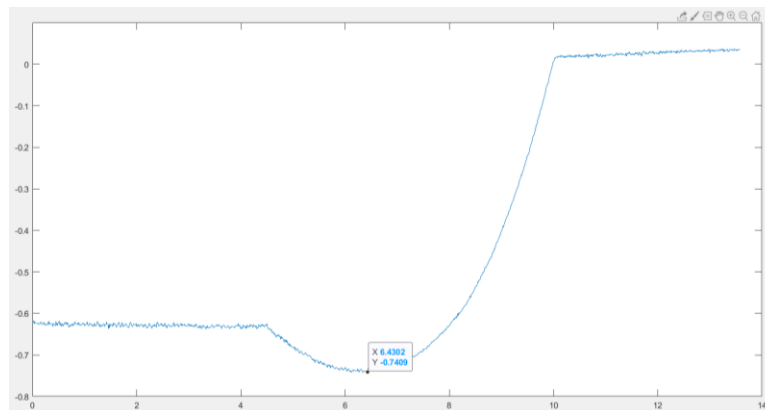


Figure 6.35: Sand Bucket Trajectory w.r.t to Time

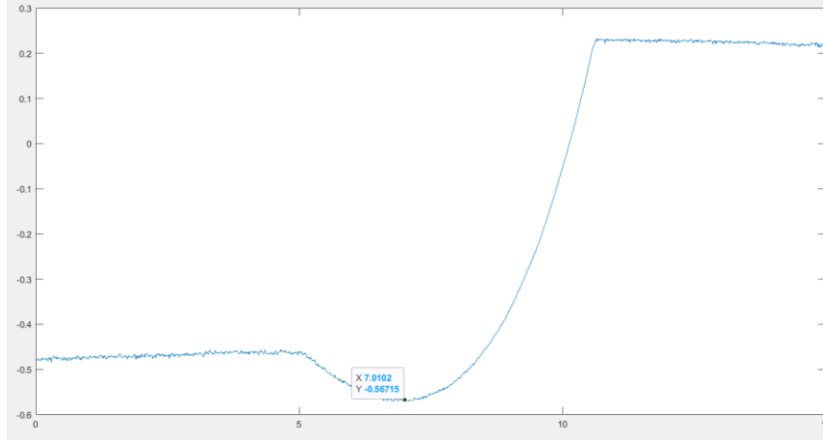


Figure 6.36: Soil Bucket Trajectory w.r.t to Time

After identifying the point of contact in time, we calculated the head, rod, and net forces at that time. The head force and rod force were calculated using the pressure data (measured by pressure sensors) and areas of the head and rod sides. The net force was calculated by subtracting the rod force from the head one. The head, rod, and net forces for the sand and soil ground are shown in Fig. 6. 37 – 6. 42).

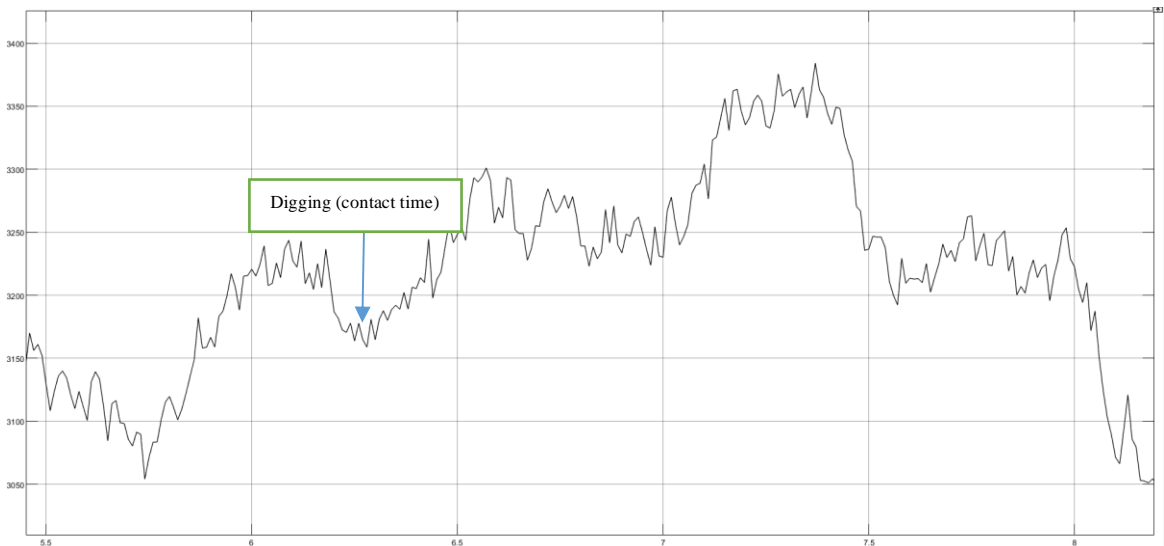


Figure 6.37: Head Force - Sand

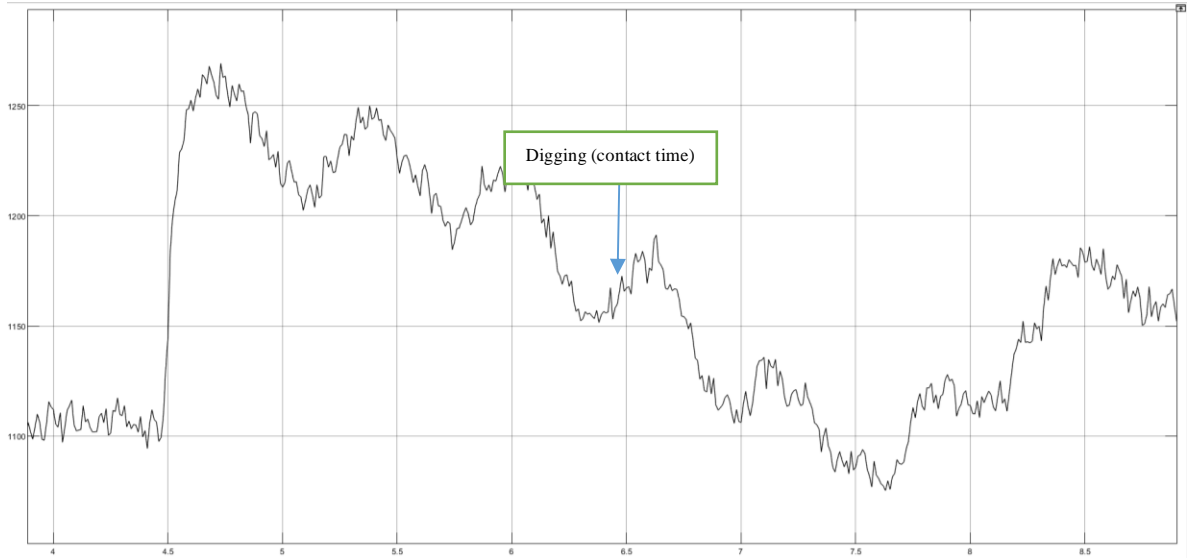


Figure 6.38: Rod Force - Sand

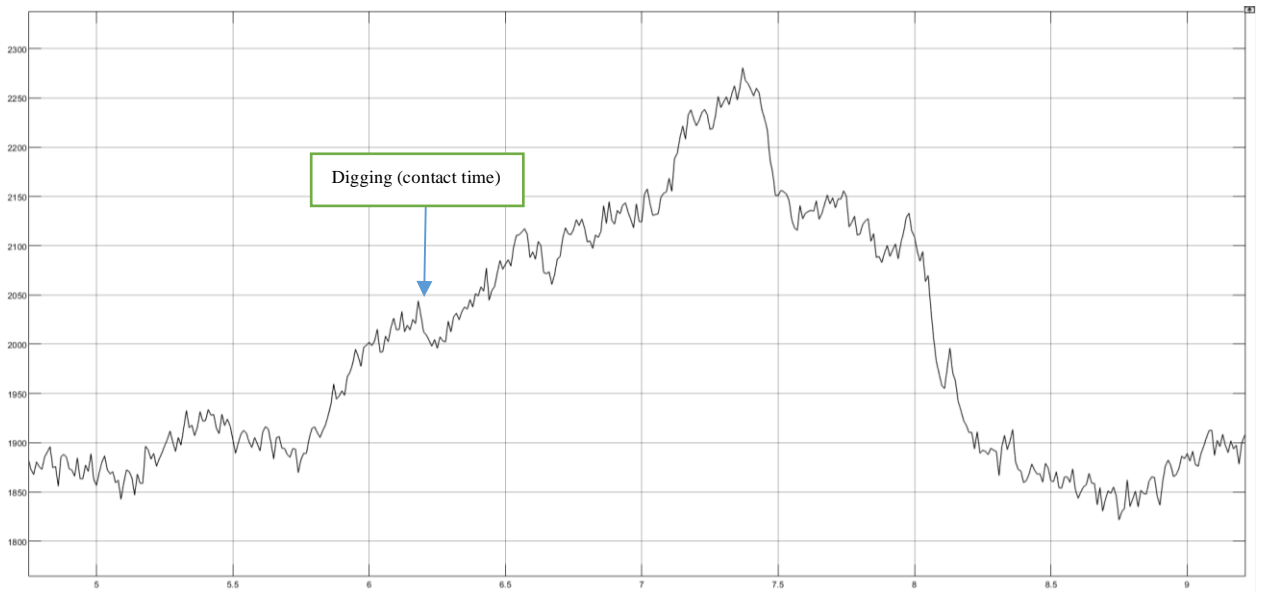


Figure 6.39: Net Force - Sand

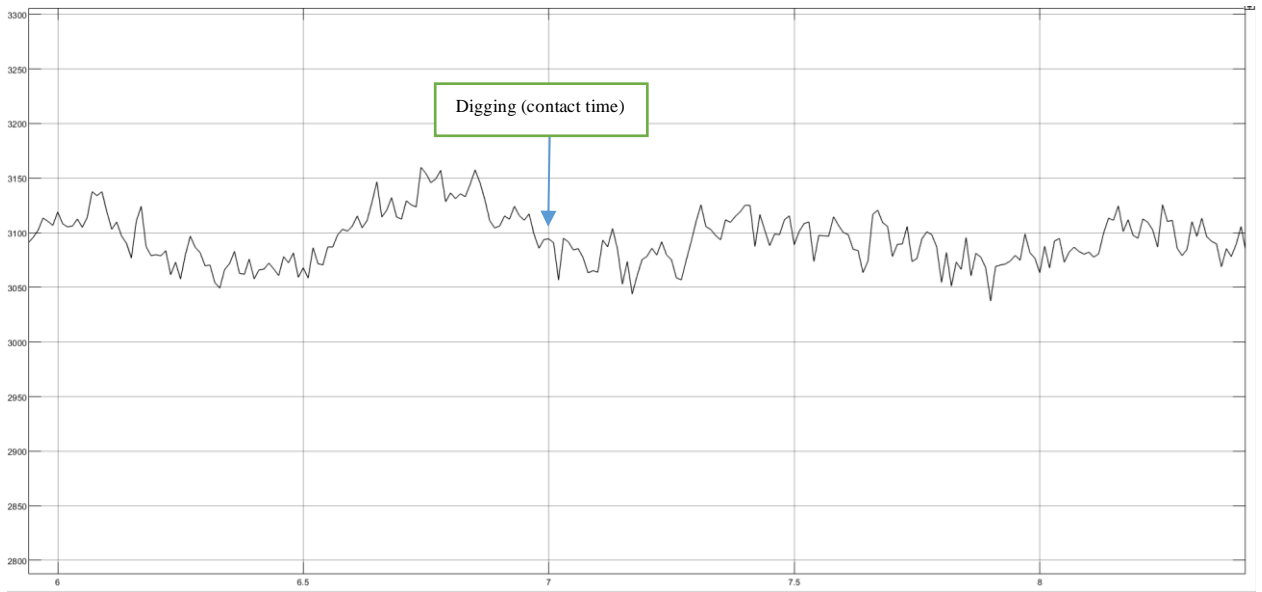


Figure 6.40: Head Force - Soil

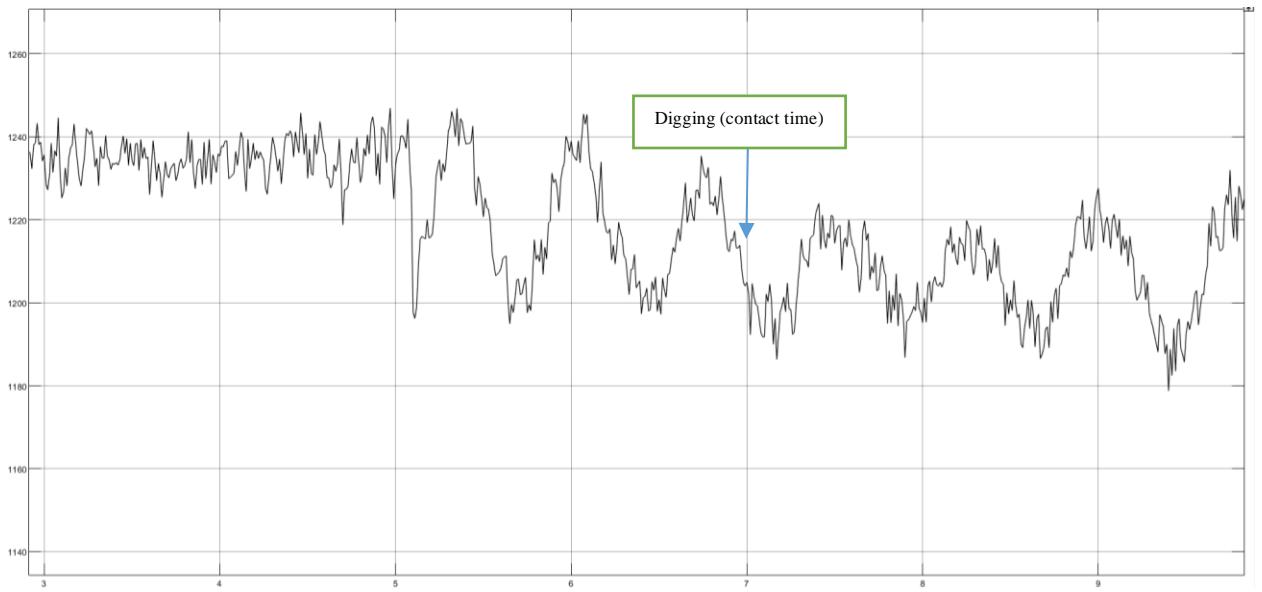


Figure 6.41: Rod Force - Soil

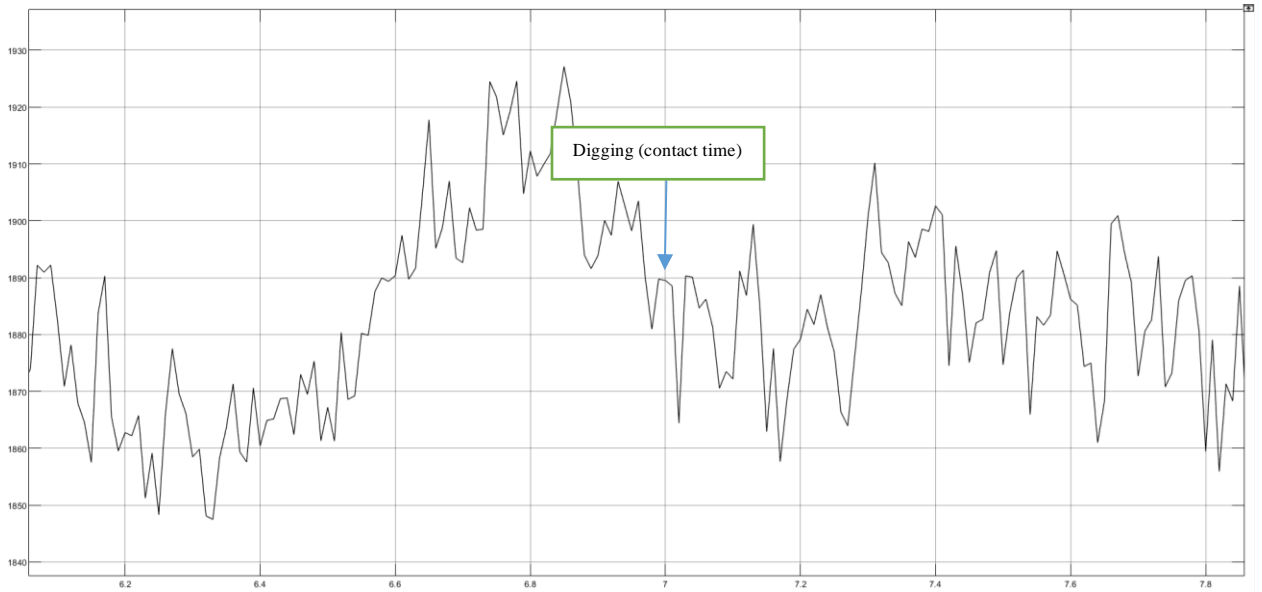


Figure 6.42: Net Force - Soil

Note that the above figures are shown to illustrate the pattern of three forces during the excavation cycle. Only the point of contact was taken for analysis.

6.6.3 Relationship between Intensities and Forces

Table 6. 2 shows the intensity and head and net forces for all the six segments.

Table 6.3: Intensity and Forces Relationship

Segment No. and Type	Intensity	Head Force (N)	Net Force (N)
1. Sand	70	3205	2050
2. Sand + Soil	22	3200	2000
3. Soil	14	3100	1900
4. Natural ground 1	36	3125	1900
5. Natural ground 2	28	3390	2250
6. Natural ground 3	22	3180	2200

Segments 1-3 were artificially distributed on the ground, and it contains three types of materials, sand, sand plus soil, and the soil. Note that the segments 1-3 were placed on the ground and not buried under the ground. Since the materials are not buried, so the ground resistive force is low in this case, and hence the resistive force is mostly material dependent. The intensity values depend on the color of the material surface, and hence, the sand has the highest intensity due to a brighter outer surface. In comparison, the soil has the lowest intensity due to a darker surface. The head and net forces for this case are material dependant. That is why it is linearly proportional to the intensity values.

Table 6.4: Natural Ground Classification Relationship

Segment Type	Intensity	Head Force	Net Force	Depth
4. Natural ground 1	36 (1)	3125 N (3)	1900 N (3)	-0.55 m (3)
5. Natural ground 2	28 (2)	3390 N (1)	2250 N (1)	-0.65 m (1)
6. Natural ground 3	22 (3)	3180 N (2)	2200 N (2)	-0.58 m (2)

Since the ground contact for digging was done on the natural hard ground, the net force index indicating the resistive force could be associated with the digging (contact) depth. So, we also checked the digging depth for segment 4, 5, and 6. From the table, we can note that the digging depth is ranked in the same order as the net (and head) force index. This means that higher digging depth may result in an increase of the resistive force during the ground contact and thus the net force index.

As seen in the above table, since there is no regular pattern between intensity and net force, the intensity information cannot indicate the severity of the resistive ground force. Therefore, the net force is a crucial component in our 5D mapping.

6.6.4 Soil type image classification results

The image classification was done using the GoogleNet pre-trained classification network. The images taken during the excavation task were utilized for training the network.



Figure 6.43: Image Classification – Segment 1



Figure 6.44: Image Classification - Segment 2



Figure 6.45: Image Classification - Segment 3

From the above figures, we can see that the trained neural network can successfully classify types of excavation materials. The occupancy is shown in the form of percentages. The average accuracy was noted to be 94%.

6.6.5 5D map Construction

The construction of a 5D map is the integration of attributes mentioned above (coordinate, intensity, and net force). The following figure illustrates the 5D map containing six segments of different types of materials and their corresponding material properties.

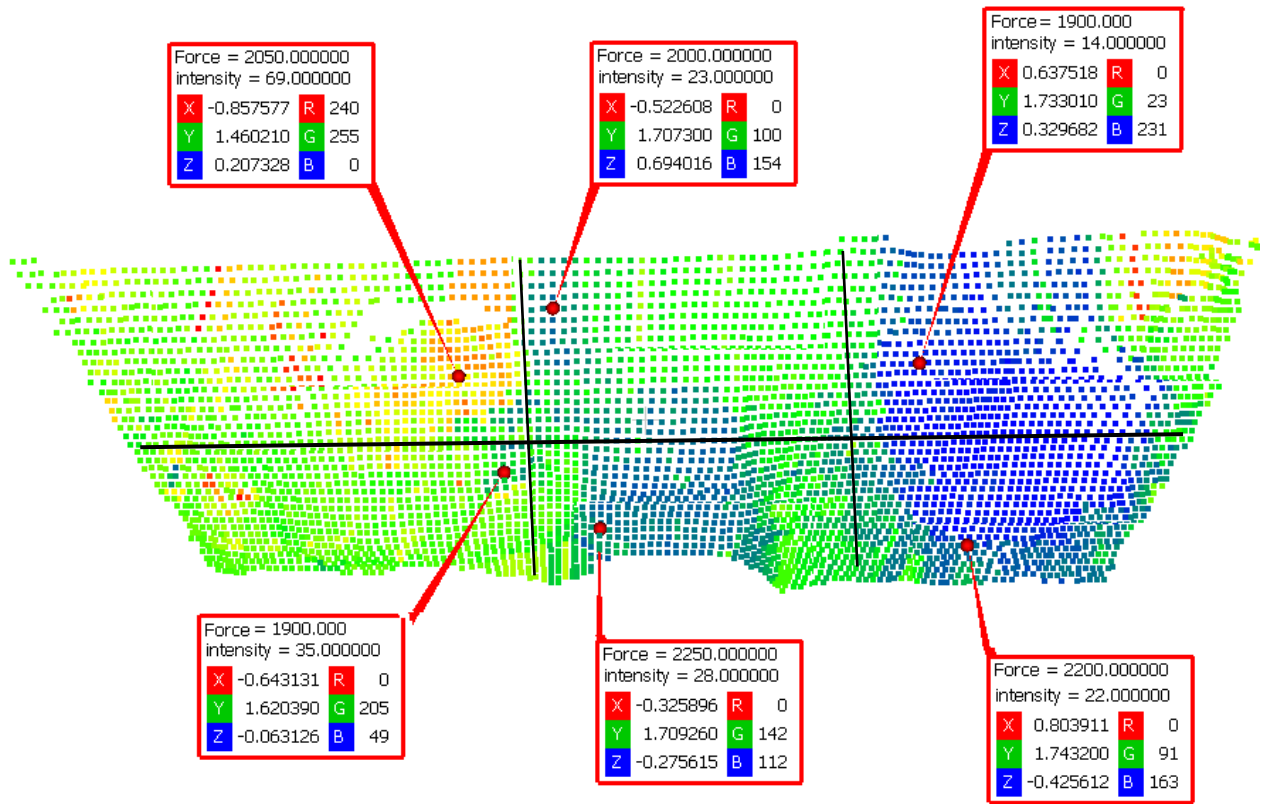


Figure 6.46: 5D Map Construction

Chapter 7. Conclusion and Future Work

7.1 Conclusion

This project aimed to design predicted safety algorithms for eliminating any chances of a potential collision, and estimation of excavation progress to estimate the completion of work in progress, deal with the occluded area issue and identify material properties.

Since the safety of autonomous excavators is crucial, there has been a need to develop more sophisticated safety control algorithms that are beyond the conventional safety techniques based on simple proximity detections and alarming. To meet this necessity, we developed the advanced safety algorithm for autonomous excavation that allows us to predict the states of the moving objects around the excavator and to calculate the time and distance to a collision.

The developed safety algorithm focuses on the predicted states of the objects around the excavator and evaluates the safety condition. The raw data from the LiDAR sensor was segmented into the ground and non-ground points using RANSAC. The non-ground points are then clustered using the K-means clustering technique. These clustered points are then converted to bounding boxes and referred to as the detected objects. To track the detected objects, EKF was used. JPDA provided the track management for associating the tracking detail such as tags, current state, predicted state, and covariance to each detected object. Using the kinematic analysis, the working area of the excavator was calculated. Finally, the safety indices were calculated using the predicted states of the objects and the working area of the excavator.

The experiments were carried out in the presence of single, multiple, static, and moving objects. VLP-16 LiDAR sensor was used to monitor the environment. The experiment results showed current and predicted states of the detected objects. Using the predicted states, and the working area of the excavator the time and distance to a collision

of each object to the excavator were calculated. The safety evaluation was indicated based on the safety indices as safe, warning, or emergency conditions.

For volume estimation, the primary focus was to estimate the progress of excavation. This was done using two different methods: ground excavation volume estimation and bucket volume estimation. The ground excavation volume estimation was carried out by subtracting the excavated ground from the pre-excavation ground. In contrast, bucket volume was estimated by comparing the bucket CAD model and a bucket containing soil after each dig. The experimental results present that the bucket volume estimation is less accurate than the ground excavation volume estimation. However, they follow the same pattern with some offset value. This is because the ground and bucket volume estimation was based on the same digging scenarios.

The occlusion area was itself a challenge during the ground mapping. This happened when the pile on the ground or the excavator's arm blocked the vision of the sensor and it was unable to perceive the correct data. There was a need to overcome the sensor occluded area for proper ground mapping. For such cases, we fused the exteroceptive and proprioceptive sensors. The proprioceptive sensors provided the data that helped in estimating the bucket trajectory while the exteroceptive sensors measured the ground map. To overcome the occluded area, the bucket trajectory was converted to 3D mesh using the triangulation method and then it was merged with the ground map to reconstruct a 3D map. The accuracy of this map was verified by taking data from the opposite side of the occluded area. The results showed that the bucket trajectory mesh could cover the occluded region but the transformation of trajectory reference to the global reference is one of the biggest factors as the wrong transformation could lead to incorrect map reconstruction.

To identify the properties of the materials, 5D mapping was introduced. This map consists of 3D geometrical info of position, intensity info based on LiDAR, and the force index of the bucket cylinder to identify the resistive ground force. The combination of these entities generates a 5D map that can be used for the excavated ground info. The 3D geometrical info is the x, y , and z position of the material. The intensity value is the LiDAR's beam reflectivity. The force index is the calculation of bucket cylinder head, and

net force. To support the classification of materials, we also applied the neural network (NN) using images taken during the excavation. For the experimental setup, we split the digging space into six segments for running tests. Each segment contains a different type of material. We built a 5D map and compared the properties of each material type. The results showed that the intensity value is directly proportional to the force for the materials that were artificially distributed, while it is inversely proportional to the natural ground. However, the depth of the natural ground is directly proportional to the ground resistive force.

The developed algorithms can be extensively used for urban excavation, agricultural machinery, and other construction equipment where safety and environmental monitoring are critical components to achieve autonomous operations.

7.2 Future Improvements

Further improvements in the area of autonomous excavation safety and progress monitoring/estimation could include:

- Introducing UAV drones to monitor the excavation site for safety and progress monitoring. This could eliminate the issue of sensors mounting and vibration factors for the mounted sensors.
- Based on our results, the bucket volume estimation is less accurate than the ground excavation volume estimation. So, there could be a need to develop a bucket volume estimation algorithm that provides more accurate results, because the bucket can be captured all the time during the excavation and therefore is a more reliable source of estimating the volume.
- Integration of the developed safety and excavation progress algorithms and its real-time operation for seamless autonomous excavation.

REFERENCES

- [1]. Reginald, N. (2020). *Development of an Integrated Tracking Control Algorithm and a Test Platform for Autonomous Excavation* (master's thesis). Ontario Tech University.
- [2]. P. K. N. Narasimha and M. A. Vinay, "Automation and Robotics in the Construction Industry - a Review," *i-manager's J. Futur. Eng. Technol.*, vol. 14, no. 3, p. 49, 2019.
- [3]. Q. Chen, B. García de Soto, and B. T. Adey, "Construction automation: Research areas, industry concerns and suggestions for advancement," *Autom. Constr.*, vol. 94, no. December 2017, pp. 22–38, 2018.
- [4]. F. Mrad, M. Asem Abdul-Malak, S. Sadek, and Z. Khudr, "Automated excavation in construction using robotics trajectory and envelop generation," *Eng. Constr. Archit. Manag.*, vol. 9, no. 4, pp. 325–335, 2002.
- [5]. Anwar, Hamza, Syed Muhammad Abbas, Abubakr Muhammad and Karsten Berns. "Volumetric Estimation of Contained Soil using 3D Sensors." (2014).
- [6]. "VeloView | ParaView", *Paraview.org*, 2020. [Online]. Available: <https://www.paraview.org/veloview/>. [Accessed: 19- Jun- 2020]
- [7]. "ZED 1.0 is here, adds Positional Tracking and 3D Reconstruction – Stereolabs", *Stereolabs*, 2020. [Online]. Available: <https://www.stereolabs.com/blog/positional-tracking-3d-reconstruction-and-more-with-zed-camera/>. [Accessed: 19- Jun- 2020]
- [8]. "CloudCompare - Open Source project", *Danielgm.net*, 2020. [Online]. Available: <https://www.danielgm.net/cc/>. [Accessed: 19- Jun- 2020]

- [9]. MATLAB - MathWorks", *Mathworks.com*, 2020. [Online]. Available: <https://www.mathworks.com/products/matlab.html>. [Accessed: 19- Jun- 2020]
- [10]. Ha, Quang & Santos, M. & Nguyen, Quang & Rye, David & Durrant-Whyte, H.. (2002). Robotic excavation in construction automation. *Robotics & Automation Magazine, IEEE*. 9. 20 - 28. 10.1109/100.993151.
- [11]. Yeom, Dong-Jun & Yoo, Hyun-Seok & Kim, Youngsuk. (2019). 3D surround local sensing system H/W for intelligent excavation robot (IES). *Journal of Asian Architecture and Building Engineering*. 1-18. 10.1080/13467581.2019.1679148.
- [12]. Zhang, M., Cao, T., & Zhao, X. (2017). Applying Sensor-Based Technology to Improve Construction Safety Management. *Sensors (Basel, Switzerland)*, 17(8), 1841. <https://doi.org/10.3390/s17081841>
- [13]. Lee, Kwang-Pyo & Lee, Hyun-Soo & Park, Moon-Seo & Kim, Hyunsoo & Baek, Yun-Ju. (2010). RFID-Based Real-Time Locating System for Construction Safety Management. *Korean Journal of Construction Engineering and Management*. 11. 10.6106/KJCEM.2010.11.2.106.
- [14]. Song, Jongchul & Haas, Carl & Caldas, Carlos. (2006). Tracking the Location of Materials on Construction Job Sites. *Journal of Construction Engineering and Management-asce - J CONSTR ENG MANAGE-ASCE*. 132. 10.1061/(ASCE)0733-9364(2006)132:9(911).
- [15]. Han, Sanguk & Lee, SangHyun. (2013). A vision-based motion capture and recognition framework for behavior-based safety management. *Automation in Construction*. 35. 131-141. 10.1016/j.autcon.2013.05.001.

- [16]. . Zhong, D.; Lv, H.; Han J.; Wei, Q. A Practical Application Combining Wireless Sensor Networks and Internet of Things: Safety Management System for Tower Crane Groups. *Sensors* 2014, 14, 13794–13814.
- [17]. Zhu, Zhenhua & Park, Man-Woo & Koch, Christian & Soltani, Mohammad & Hammad, Amin & Davari, Khashayar. (2016). Predicting movements of onsite workers and mobile equipment for enhancing construction site safety. *Automation in Construction*. 68. 95-101. 10.1016/j.autcon.2016.04.009.
- [18]. Arslan, Malik & Riaz, Zainab & Kiani, Adnan & Azhar, Salman. (2014). Real-time environmental monitoring, visualization and notification system for construction H&S management. *Journal of Information Technology in Construction (ITcon)*. 19. 72-91.
- [19]. Oh, K., Park, S., Seo, J., Kim, J.-G., Park, J., Lee, G., & Yi, K. (2019). Development of a predictive safety control algorithm using laser scanners for excavators on construction sites. *Proceedings of the Institution of Mechanical Engineers, Part D: Journal of Automobile Engineering*, 233(8), 2007–2029. <https://doi.org/10.1177/0954407018764046>
- [20]. Ahmad Hemami (October 1st 2008). Robotic Excavation, *Robotics and Automation in Construction*, Carlos Balaguer and Mohamed Abderrahim, IntechOpen, DOI: 10.5772/5620
- [21]. Stentz, J. Bares, S. Singh and P. Rowe, "A robotic excavator for autonomous truck loading," *Proceedings. 1998 IEEE/RSJ International Conference on Intelligent Robots and Systems. Innovations in Theory, Practice and*

Applications (Cat. No.98CH36190), Victoria, BC, Canada, 1998, pp. 1885-1893
vol.3, doi: 10.1109/IROS.1998.724871.

- [22]. Toledo, Mauricio & Isamitt, Valeria. (2017). A Proposal for Controlling Work Progress on Excavation Projects Using Digital Photographs. *Advanced Engineering Forum*. 21. 397-404. 10.4028/www.scientific.net/AEF.21.397.
- [23]. Bewley, Alex & Upcroft, Ben & Lever, Paul & Leonard, S.. (2009). Automatic in-bucket volume estimation for dragline operations.
- [24]. D. Jud, P. Leemann, S. Kerscher and M. Hutter, "Autonomous Free-Form Trenching Using a Walking Excavator," in *IEEE Robotics and Automation Letters*, vol. 4, no. 4, pp. 3208-3215, Oct. 2019, doi: 10.1109/LRA.2019.2925758.
- [25]. Niskanen, Ilpo & Immonen, Matti & Makkonen, Tomi & Keränen, Pekka & Tyni, Pekka & Hallman, Lauri & Hiltunen, Mikko & Kolli, Tanja & Louhisalmi, Yrjö & Kostamovaara, Juha & Heikkilä, Rauno. (2020). 4D modeling of soil surface during excavation using a solid-state 2D profilometer mounted on the arm of an excavator. *Automation in Construction*. 112. 10.1016/j.autcon.2020.103112.
- [26]. Puck Lidar Sensor, High-Value Surround Lidar | Velodyne Lidar, *Velodyne Lidar*, 2020. [Online]. Available: <https://velodynelidar.com/products/puck/>. [Accessed: 19- Jun- 2020]
- [27]. "ZED Stereo Camera | Stereolabs", *Stereolabs.com*, 2020. [Online]. Available: <https://www.stereolabs.com/zed/>. [Accessed: 19- Jun- 2020]
- [28]. "Use Case: Automated Driving Functions", *Dspace.com*, 2020. [Online]. Available:

https://www.dspace.com/en/pub/home/products/systems/functp/usecases_rcp/driv-erassist.cfm. [Accessed: 19- Jun- 2020]

- [29]. "Continental Automotive", *Continental-automotive.com*, 2020. [Online]. Available: <https://www.continental-automotive.com/en-gl/Passenger-Cars/Autonomous-Mobility/Enablers/Lidars/3D-Flash-Lidar>. [Accessed: 19- Jun- 2020]
- [30]. "Quanergy | M Series High Performance 360 Degree LiDAR Sensor", *Quanergy*, 2020. [Online]. Available: <https://quanergy.com/products/m8/>. [Accessed: 18- Jun- 2020]
- [31]. *Ouster.com*, 2020. [Online]. Available: <https://ouster.com/products/os1-lidar-sensor/>. [Accessed: 19- Jun- 2020]
- [32]. Solid-State LiDAR: Leddar M16 Multi-segment sensor module", *LeddarTech*, 2020. [Online]. Available: <https://leddartech.com/lidar/m16-multi-segment-sensor-module/>. [Accessed: 19- Jun- 2020]
- [33]. "Depth Camera D435i – Intel® RealSense™ Depth and Tracking Cameras", *Intel® RealSense™ Depth and Tracking Cameras*, 2020. [Online]. Available: <https://www.intelrealsense.com/depth-camera-d435i/>. [Accessed: 19- Jun- 2020]
- [34]. "Bumblebee® XB3 FireWire | FLIR Systems", *Flir.com*, 2020. [Online]. Available: <https://www.flir.com/support/products/bumblebee-xb3-firewire>. [Accessed: 19- Jun- 2020]

- [35]. Torr, Philip Zisserman, A. (2000). MLESAC: A New Robust Estimator with Application to Estimating Image Geometry. *Computer Vision and Image Understanding*. 78. 138-156. 10.1006/cviu.1999.0832
- [36]. Brown, R.G. and P.Y.C. Wang. *Introduction to Random Signal Analysis and Applied Kalman Filtering*. 3rd Edition. New York: John Wiley Sons, 1997.
- [37]. Kalman, R. E. “A New Approach to Linear Filtering and Prediction Problems.” *Transactions of the ASME–Journal of Basic Engineering*. Vol. 82, Series D, March 1960, pp. 35–45.
- [38]. Jung J, Paxson V, Berger A, et al. Fast portscan detection using sequential hypothesis testing. In: *Proceedings of the 2004 IEEE*
- [39]. "Joint probabilistic data association tracker - MATLAB", *Mathworks.com*, 2020. [Online]. Available: <https://www.mathworks.com/help/fusion/ref/trackerjpda-system-object.html>. [Accessed: 19- Jun- 2020]
- [40]. Besl, Paul J., N. D. McKay. “A Method for Registration of 3-D Shapes.” *IEEE Transactions on Pattern Analysis and Machine Intelligence*. Los Alamitos, CA: IEEE Computer Society. Vol. 14, Issue 2, 1992, pp. 239–256.
- [41]. Magnusson, M. “The Three-Dimensional Normal-Distributions Transform — an Efficient Representation for Registration, Surface Analysis, and Loop Detection.” Ph.D. Thesis. Örebro University, Örebro, Sweden, 2013.
- [42]. Transform 3-D point cloud - MATLAB pcttransform", *Mathworks.com*, 2020. [Online]. Available:

<https://www.mathworks.com/help/vision/ref/pctransform.html>. [Accessed: 21-Jun- 2020].

[43]. Mathworks.com. 2020. *Matrix Representation Of Geometric Transformations- MATLAB & Simulink*. [online] Available at: <<https://www.mathworks.com/help/images/matrix-representation-of-geometric-transformations.html>> [Accessed 21 June 2020].

[44]. Siemens Digital Industries Software. 2020. *NX*. [online] Available at: <<https://www.plm.automation.siemens.com/global/en/products/nx/>> [Accessed 21 June 2020].

[45]. Mathworks.com. 2020. *Triangulation Representations- MATLAB & Simulink*. [online] Available at: <<https://www.mathworks.com/help/matlab/math/triangulation-representations.html>> [Accessed 21 June 2020].

[46]. P. F. Timon Homberger, Lorenz Wellhausen and M. Hutter, “Support surface estimation for legged robots,” in IEEE International Conference on Robotics and Automation (ICRA), 2019.

[47]. Mineo, Carmelo & Pierce, Stephen & Nicholson, Ian & Cooper, Ian. (2017). Introducing a novel Mesh Following Technique for approximation-free robotic tool path trajectories. *Journal of Computational Design and Engineering*. 4. 10.1016/j.jcde.2017.01.002.

[48]. LiDAR Intensity: What is it and What are it’s applications? - Geodetics. (2020). Retrieved 22 June 2020, from <https://geodetics.com/lidar-intensity-applications/>

- [49]. Deep Learning Toolbox. (2020). Retrieved 22 June 2020, from <https://www.mathworks.com/products/deep-learning.html>
- [50]. BVLC/caffe. (2020). Retrieved 22 June 2020, from https://github.com/BVLC/caffe/tree/master/models/bvlc_googlenet
- [51]. Szegedy, Christian, Wei Liu, Yangqing Jia, Pierre Sermanet, Scott Reed, Dragomir Anguelov, Dumitru Erhan, Vincent Vanhoucke, and Andrew Rabinovich. "Going deeper with convolutions." In *Proceedings of the IEEE conference on computer vision and pattern recognition*, pp. 1-9. 2015.
- [52]. Kala, Rahul. (2016). Basics of Autonomous Vehicles. 10.1016/B978-0-12-803729-4.00002-7.
- [53]. Hariyama, Masanori & Yokoyama, Naoto & Kameyama, Michitaka. (2008). Design of a Trinocular-Stereo-Vision VLSI Processor Based on Optimal Scheduling. *IEICE Transactions on Electronics*. 91-C. 479-486. 10.1093/ietele/e91-c.4.479.
- [54]. "Review: GoogLeNet (Inception v1)— Winner of ILSVRC 2014 (Image Classification)", Medium, 2020. [Online]. Available: <https://medium.com/coinmonks/paper-review-of-googlenet-inception-v1-winner-of-ilsvlc-2014-image-classification-c2b3565a64e7>. [Accessed: 15- Jul- 2020]

APPENDICES

Appendix A. Point cloud Transformation

Appendix A.1: 3D Geometric Transformation Matrices

3D Affine Transformation	Transformation Matrix		
Translation	$\begin{bmatrix} 1 & 0 & 0 & 0 \\ 0 & 1 & 0 & 0 \\ 0 & 0 & 1 & 0 \\ t_x & t_y & t_z & 1 \end{bmatrix}$		
Scale	$\begin{bmatrix} s_x & 0 & 0 & 0 \\ 0 & s_y & 0 & 0 \\ 0 & 0 & s_z & 0 \\ 0 & 0 & 0 & 1 \end{bmatrix}$		
Shear	x,y shear: $x' = x + az$ $y' = y + bz$ $z' = z$ $\begin{bmatrix} 1 & 0 & 0 & 0 \\ 0 & 1 & 0 & 0 \\ a & b & 1 & 0 \\ 0 & 0 & 0 & 1 \end{bmatrix}$	x,z shear: $x' = x + ay$ $y' = y$ $z' = z + cy$ $\begin{bmatrix} 1 & 0 & 0 & 0 \\ a & 1 & c & 0 \\ 0 & 0 & 1 & 0 \\ 0 & 0 & 0 & 1 \end{bmatrix}$	y,z shear: $x' = x$ $y' = y + bx$ $z' = z + cx$ $\begin{bmatrix} 1 & b & c & 0 \\ 0 & 1 & 0 & 0 \\ 0 & 0 & 1 & 0 \\ 0 & 0 & 0 & 1 \end{bmatrix}$
Rotation	About x-axis $\begin{bmatrix} 1 & 0 & 0 & 0 \\ 0 & \cos(a) & \sin(a) & 0 \\ 0 & -\sin(a) & \cos(a) & 0 \\ 0 & 0 & 0 & 1 \end{bmatrix}$	About y-axis $\begin{bmatrix} \cos(a) & 0 & -\sin(a) & 0 \\ 0 & 1 & 0 & 0 \\ \sin(a) & 0 & \cos(a) & 0 \\ 0 & 0 & 0 & 1 \end{bmatrix}$	About z-axis $\begin{bmatrix} \cos(a) & \sin(a) & 0 & 0 \\ -\sin(a) & \cos(a) & 0 & 0 \\ 0 & 0 & 1 & 0 \\ 0 & 0 & 0 & 1 \end{bmatrix}$

